Czech Technical University in Prague
Faculty of Nuclear Sciences and Physical Engineering

Department of Physics

S-wave charmonia studies using the ATLAS detector

Bachelor Thesis

Lukáš Novotný
Supervisor: Ing. Michal Marčišovský, PhD.

Prague, 2016

České vysoké učení technické v Praze
Fakulta jaderná a fyzikálně inženýrská

Katedra Fyziky

Studium s-wave charmonií pomocí detektoru ATLAS

Bakalářská práce

Lukáš Novotný
Vedoucí práce: Ing. Michal Marčišovský, PhD.
Praha, 2016

Zadání práce

Declaration

I hereby declare that this thesis is the result of my own work and all the sources I used are in the list of references. I have no objection to usage of this work in compliance with the act §60 Law No. 121/2000 Coll. (Copyright Act), and with the rights connected with the copyright act including the changes in the act.

Prohlášení

Prohlašuji, že jsem svou bakalářkou práci vypracoval samostatně a použil jsem pouze podklady uvedené v přiloženém seznamu. Nemám závažný důvod proti použití tohoto díla ve smyslu §60 zákona č.121/2000 Sb., o právu autorském, o právech souvisejících s právem autorským a o změně některých zákonů (autorský zákon).

v Praze dne ....

Lukáš Novotný

Acknowledgement

I would like to express my gratitude to my supervisor Michal Marčišovský for his invaluable advice, patience, willingness and professional guidance during the realization of this work. I am very grateful to Mária Čarná for language corrections and Václav Vrba for overall support of my work. Furthermore, I would like to thank Radek Novotný for helpful advice and discussions. Last but not least, I would like to thank my family, girlfriend and friends for their encouragement and support.

Lukáš Novotný

Title: **S-wave charmonia studies using the ATLAS detector**

Author: Lukáš Novotný

Specialization: Experimental nuclear and particle physics

Sort of project: Bachelor thesis

Supervisor: Ing. Michal Marčišovský, PhD.

Abstract: This thesis is dedicated to the J/ψ and $\psi(2S)$ mass and lifetime fit with respect to the transverse moment and rapidity, the J/ψ and $\psi(2S)$ cross section and the ratio of their cross section in proton-proton collisions measured by the ATLAS detector at the Large Hadron Collider (LHC) at center of mass energy $\sqrt{s} = 13$ TeV.
Firstly, the thesis is devoted to the Standard Model, then the ATLAS detector at the LHC is introduced and ATLAS Trigger System and Offline Software is mentioned. The thesis ends with the data analysis model and results.

Key words: J/ψ, $\psi(2S)$, muon channel, charmonium, ATLAS, LHC, cross section

Název práce: **Studium s-wave charmonií pomocí detektoru ATLAS**

Autor: Lukáš Novotný

Obor: Experimentální jaderná a částicová fyzika

Druh práce: Bakalářská práce

Vedoucí práce: Ing. Michal Marčišovský, PhD.

Abstrakt: Tato práce se věnuje hmotnostnímu a časovému fitu částic $J\psi$ a $\psi(2S)$, dále se zabývá měřením účinných průřezů částic obou částic a poměrem jejich účinných průřezů v proton-protonových srážkách měřených detektorem ATLAS v LHC při těžišťové energii $\sqrt{s} = 13$ TeV. Zpočátku se práce věnuje Standardnímu modelu elementárních částic, poté je představen detektor ATLAS následovaný textem o systému triggerování a offline softwaru na ATLASu. Na závěr je zmíněn použitý analyzační model a jsou ukázány výsledky analýzy.

Klíčová slova: J/ψ, $\psi(2S)$, mionový kanál, charmonium, ATLAS, LHC, účinný průřez

Contents

List of Figures

List of Tables

Introduction

Charmonium is a bound state of a charm quark and antiquark. The most widely known charmonia J/ψ and $\psi(2S)$ can decay via an electromagnetic interaction to a $\mu^+\mu^-$ pair. The charmonium system has become the 'hydrogen atom' of meson spectroscopy, because it was believed that charmonium could help us to understand hadronic dynamics as the hydrogen atom did in understanding the atomic physics.

It can be also used for B-hadron detection or for the measurement of the quark gluon plasma (QGP) temperature. Last but not least, it is widely used in detector performance studies for the measurement of the detector reconstruction efficiency and the detector resolution.

The history, description and role of charmonia in the Standard Model, which is described in the first chapter, is presented in the second chapter. This thesis uses data of the proton-proton collisions recorded by the ATLAS detector at the LHC. ATLAS as a multi-purpose detector is introduced in the third chapter. In the fourth chapter, the ATLAS trigger system and offline software are introduced.

The main achievement of this thesis is presented in the last chapter, where the J/ψ and $\psi(2S)$ production fractions and cross-sections are shown.

Chapter 1

Introduction to the particle physics

Contemporary instrumentation and theories allow us to describe the behaviour of the particles. These objects are described by the theory called Standard Model. According to this model, all matter is made of particles without inner structure, called elementary particles, and interacts through force carriers.

family		symbol	name	mass	spin	charge	discovered
fermions	quarks	u	up	$2.3^{+0.7}_{-0.5}$ MeV	1/2	2/3	1968
		d	down	$4.8^{+0.5}_{-0.3}$ MeV	1/2	$-1/3$	1968
		s	strange	95 ± 5 MeV	1/2	$-1/3$	1968
		c	charm	1.275 ± 0.025 GeV	1/2	2/3	1974
		b	bottom	4.18 ± 0.03 GeV	1/2	$-1/3$	1977
		t	top	$173.21 \pm 0.51 \pm 0.71$ GeV	1/2	2/3	1995
	leptons	e	electron	510.998928 ± 0.000011 keV	1/2	-1	1897
		μ	muon	$105.6583715 \pm 0.0000035$ MeV	1/2	-1	1936
		τ	tau	1776.82 ± 0.16 MeV	1/2	-1	1975
		ν_e	e-neutrino	< 2 eV	1/2	0	1956
		ν_μ	μ-neutrino	< 0.19 MeV	1/2	0	1962
		ν_τ	τ-neutrino	< 18.2 MeV	1/2	0	2000
bosons	vector	γ	photon	$< 10^{-18}$ eV	1	0	1905[1]
		g	gluon	0	1	0	1978
		$W^{\pm}$	W boson	80.385 ± 0.015 GeV	1	± 1	1983
		Z^0	Z boson	91.1876 ± 0.0021 GeV	1	0	1983
	skalar	H	Higgs boson	125.7 ± 0.4 GeV	0	0	2012

Table 1.1: Particles and force carriers in the Standard model [1].

[1] In 1670, Isaac Newton came with the corpuscular hypothesis, where he claimed the light behave as particle. However, forty years before, René Descartes had published his wave theory of the light. Scientists

1.1 The Standard model

This theory, developed in the 1970s, successfully explains almost all collider experimental results. It contains bosons with integer fundamental spin and 12 fermions with half-integer fundamental spin. Fermions obey Fermi-Dirac statistics and bosons obey Bose-Einstein statistics. For more details, see Table 1.1.

1.1.1 The quantum description of a particle

Using the Fourier transformation, the energy in the quantum world can be substituted with the operator $E \to i\hbar\frac{\partial}{\partial t}$ and the momentum p with the operator $p \to -i\hbar\nabla$. Thus, the equation of the energy conservation $E = \frac{p^2}{2m} + V$, where V is the potential, is transformed into the time-dependent Schrödinger equation

$$i\hbar\frac{\partial}{\partial t}\psi = -\frac{\hbar^2}{2m}\nabla^2\psi + \hat{V}\psi. \tag{1.1}$$

Substituting the right side of the equation (1.1) with the hamiltonian $\hat{H}$, this equation transforms into

$$i\hbar\frac{\partial}{\partial t}\psi = \hat{H}\psi. \tag{1.2}$$

The hamiltonian $\hat{H}$ is the operator corresponding to the total energy of the system. It has discrete spectrum of eigenvalues. In general, the physical quantity can be described by the linear operators in the quantum mechanics. Not only the hamiltonian has a discrete spectrum, for example the squared angular momentum $\hat{L}^2$ with eigenvalues $\sqrt{l(l+1)}\hbar$ $(l \in \mathbb{N}_0)$[2], the third component of angular momentum $\hat{L}_z$ has eigenvalues $m\hbar$ $(m = -l, \ldots, 0 \ldots, l)$. Also other operators such as the parity $\hat{P}$, the charge conjugation operator $\hat{C}$ and the time reversal operator $\hat{T}$ have discrete spectra.

The parity

The parity operator $\hat{P}$ inverses the three spatial coordinate axes $(x, y, z \to -x, -y, -z)$

$$\hat{\mathrm{P}}\psi\left(\mathbf{r}\right) = \psi\left(-\mathbf{r}\right). \tag{1.3}$$

Moreover, it also inverses the direction of momentum, but it does not change time and angular momentum. In two dimension, the inversion of axes is equivalent to the 180° rotation.
Applying twice the parity operator, the original state is obtained, which implies that the eigenvalues of the parity are $P = \pm 1$.

had argued for centuries, until Albert Einstein came with wave-corpuscular dualism, the idea that the light (the photon) is wave and particle concurrently.

The charge conjugation

The charge conjugation operator $\hat{C}$ reverses the sign of the charge and magnetic moment of the particle, other coordinates are conserved. This implies that $\hat{C}$ replaces the particle with its own antiparticle,

$$\hat{\mathrm{C}}\psi\left(\mathbf{r}\right) = \overline{\psi}\left(\mathbf{r}\right). \tag{1.4}$$

Similarly to the parity, the eigenvalues of the charge conjugation operator are $C = \pm 1$.

The time reverse

The time reversal operator $\hat{T}$ changes the time direction,

$$\hat{\mathrm{T}}\psi\left(\mathbf{r}, t\right) = \psi\left(\mathbf{r}, -t\right). \tag{1.5}$$

The CPT invariance

The CPT theorem states that all interactions are invariant under the simultaneous application of the parity, charge conjugation and time operator. Using the charge conjugation $\hat{C}$ operator independently, it would be violated in the weak interactions. CP is also violated (thus the time T is violated). This violation was firstly observed in the neutral kaon decay [4]. The CPT invariance in the observations of the high energy physics experiments seems to be conserved [5], [6], [7].

1.1.2 Fundamental interactions

	gravitational	electromagnetic	weak	strong
boson	graviton[2]	photon	$W^{\pm}$, Z^0	gluons
spin-parity	2^+	1^-	1^-, 1^+	1^-
mass [GeV]	0[3]	0	$m_W = 80.2$, $m_Z = 91.2$	0
source	mass	electric charge	weak charge	colour charge
range [m]	∞	∞	10^{-18}	$\leq 10^{-15}$
coupling constant	$\frac{G_N M^2}{4\pi\hbar c} = 5 \cdot 10^{-40}$	$\alpha = \frac{e^2}{4\pi\hbar c} = \frac{1}{137}$	$\frac{G\left(Mc^2\right)^2}{(\hbar c)^3} = 1 \cdot 10^{-5}$	$\alpha_S \leq 1$

Table 1.2: Fundamental interactions [2].

There are four fundamental interactions - strong, electromagnetic, weak and gravitational, but only the first three are incorporated into the Standard Model and are realized

[2]The graviton is a hypothetical particle. However, the gravitational waves (the influence of the graviton or graviton itself) were observed in 2016[10].

[3]The mass of graviton is expected to be zero in four dimensions (three space and one time), but it can have mass in more dimensions.

by gauge bosons mentioned in Table 1.1. In our every day life, the gravitational and electromagnetic force are usually observed, strong and weak interaction become important at the distance scales of 10^{-15} m and smaller.

Electromagnetic interactions

Electromagnetic interactions between charged particles are mediated by photon exchange. Particles with the same sign of charge repel each other and particles with the opposite charge attract each other. The value of the coupling constant, or the fine structure constant, is at low energy levels equal to

$$\alpha = \frac{1}{4\pi\varepsilon_0}\frac{e^2}{\hbar c} \simeq \frac{1}{137}, \tag{1.6}$$

where e is the elementary charge. At the energy scales of Z^0 boson mass, the coupling constant is $\alpha \simeq \frac{1}{128}$. The lightest charged particle is an electron with lifetime $\tau_e > 4 \cdot 10^{26}$ years. Because electron can decay only by violating the charge conservation and it has not been observed yet, it is assumed, that in every reaction or decay, the total charge is conserved. The electromagnetic interaction is described within the quantum electrodynamics framework (QED). In this theory, the definition (1.6) is not constant, but it depends on the energy scale at wich the measurement is made. The relation (1.6) then becomes the running coupling (1.20) described in the section 1.3.1.

Gravitational interaction

The effects of the gravitational interaction demonstrate themselves predominantly in the macroscopic world, gravitating objects curve the spacetime around themselves which can manifest itself by exerting a force on a nearby objects. It binds objects to the surface of the Earth, holds together star clusters and galaxies. Its coupling strength is defined via the Newtonian constant

$$G = 6.673 \cdot 10^{-11}\ \mathrm{m^3 kg^{-1} s^{-2}}, \tag{1.7}$$

which is a constant used in the Einstein field equations of the general theory of relativity,

$$R_{\mu\nu} - \frac{1}{2} R g_{\mu\nu} = \frac{8\pi G}{c^4} T_{\mu\nu}, \tag{1.8}$$

$R_{\mu\nu}$ is the Ricci curvature tensor, R is the scalar curvature or the Ricci scalar, $g_{\mu\nu}$ is the metric tensor and $T_{\mu\nu}$ is the stress-energy tensor generalizing the stress tensor of Newtonian physics [8].

In the Newtonian approach, the force between two point particles with mass M and distance r is given by $\frac{G_N M^2}{r^2}$. By using the electromagnetic force between charged particles, e^2/r^2, we can substitute GM^2 in the definition (1.6) for e^2/ε_0 and obtain a constant

$$\frac{GM^2}{4\pi\hbar c} = 5.34 \cdot 10^{-40}. \tag{1.9}$$

In comparison with the fine structure constant (1.6), the gravitational interaction is negligibly small in high energy physics and microscopic physics and it is not included in the Standard Model. On the other hand, gravitational interaction is crucial in cosmology, because it is a long-distance interaction and non-existence of negative gravitational charge. The gravitational force is only attractive and it is hypothetically mediated through graviton in the quantum field theories [9], the massless (in four dimensions) particle with spin 2. As mentioned in the footnote of the Table 1.2, the gravitational waves were recently discovered, but the graviton was not observed directly.

Strong interaction

Quarks and gluons interact via the strong interaction, but leptons do not. For example, this force binds quarks in protons and neutrons. The analogy of electric charge in this interaction is called colour. There are three colours (red, green, blue) and three anticolours (antired, antigreen, anti blue). Colour is a new degree of freedom, so every quark has one of three colours and antiquarks one of three anticolours. The strong interaction is mediated through gluons, which has also colour. Nine types of gluons exist, but only eight of them can carry the colour information and the remaining one is colourless. Eight states can be mixed into each other under SU(3) transformations and one can not be mixed with others, this decomposition can be written as

$$3 \otimes \overline{3} = 8 \oplus 1. \tag{1.10}$$

The strong interaction is described within the quantum chromodynamics framework (QCD), which will be mentioned later in this chapter [2].

Weak interaction

The weak interaction is mediated through exchange of $W^{\pm}$ or Z^0 bosons (Z^0 is considered to mediate the electroweak interaction, because it can mix with the photon [2]). This interaction can be encountered in macroscopic world, it is for example responsible for thermonuclear fusion in Sun or for beta decay, where one neutron in the nucleus is transformed into proton with radiating the W^- boson, which decays into electron and electron antineutrino. As it is visible on this reaction, the weak interaction change flavour. It also has the smallest range of interaction, see Table 1.2.

1.1.3 Leptons

Nowadays, six leptons are known to exist. There are three leptons with charge equal to -1: electron e, muon μ and tau τ. To each charged lepton there is its neutral counterpart, called neutrino and labelled ν, one for each charged lepton. Electron, muon and tau form

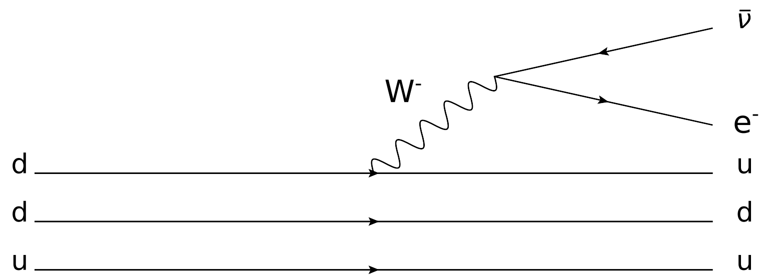

Figure 1.1: The neutron (ddu) decaying into the proton (udu), electron and electron antineutrino via the weak interaction.

doublets[4] together with neutrinos

$$\begin{pmatrix} e \\ \nu_e \end{pmatrix}, \begin{pmatrix} \mu \\ \nu_\mu \end{pmatrix}, \begin{pmatrix} \tau \\ \nu_\tau \end{pmatrix}. \tag{1.11}$$

These doublets are also referred to as generations, the electron and electron-neutrino form the first generation. The behaviour of leptons in the reaction can be described by lepton flavour numbers L_e, L_μ, L_τ, equal to $+1$ for each lepton and -1 for each antilepton. All lepton flavour numbers have to be conserved in the process through arbitrary fundamental interaction.
The muon and tau are unlike electron unstable, the mean lifetimes are $t_\mu = 2.197 \cdot 10^{-6}$ s for μ [1] and $t_\tau = 2.9 \cdot 10^{-13}$ s for τ [1].
All leptons have spin 1/2 and interact weakly, but only charged leptons interact electromagnetically. Thus, neutrinos can pass through the matter more easily than other leptons. They were originally postulated in 1930 by Wolfgang Pauli[11] in order to conserve the energy and momentum in the β-decay. It is assumed in the Standard Model neutrinos are massless, however neutrino flavour mixing and flavour oscillations are observed, so neutrinos are not massless particles[5]

Scientists discovered that , as . This implies the .

1.1.4 Quarks

Similarly to leptons, quarks have spin 1/2 and form three doublets

$$\begin{pmatrix} u \\ d \end{pmatrix}, \begin{pmatrix} s \\ c \end{pmatrix}, \begin{pmatrix} t \\ b \end{pmatrix}. \tag{1.12}$$

Quarks u and d form the first, s and c the second and t and b the third generation. The upper part of doublets has electric charge 2/3 (u, c and t) and the bottom part has charge of $-1/3$ (d, s and b). Quarks interact through all known fundamental forces, and are the

[4] The doublet notation results from the SU(2) group.

[5] The mass of neutrino are estimated in the Table 1.1. According to precise cosmological measurement of Planck probe, the sum of neutrino masses is $\sum m_\nu < 0.23$ eV. [17]

only ones which do through strong force, because they carry one of three colours, red (r), green (g) and (b).
The existence of quarks was independently predicted in 1964 by G. Zweig [12] and M. Gell-Mann [13]. Only up, down and strange quarks were known at the time, others were discovered later, charm quark in 1974 [14], bottom quark in 1977 [15] and top quark in 1995 [16].
Quarks can exist only in a bound state with another quarks or antiquarks, separated quark has not been observed, except the top quark, which decays before it has a chance for hadronization. Quark composites are called hadrons, the most common are mesons and baryons, but also tetraquarks and pentaquarks have been recently observed. Nevertheless, the bound state of top quark was not observed due to its small lifetime.
There are quantum numbers which describe quarks and their formations. The baryon number $\mathfrak{B}$ is defined as the number of baryons minus number of antibaryons,

$$\mathfrak{B} = N(\text{baryons}) - N(\text{antibaryons}).$$

It is easy to see, that $\mathfrak{B} = 1$ for baryons, which means, that the baryon number of quark is 1/3. Others quark flavour numbers are strangeness S (number of strange antiquarks minus number of strange quarks) charm C (number of charm quarks minus number of charm antiquarks), beauty B (number of bottom antiquarks minus number of bottom quarks) and top T (number of charm quarks minus number of charm antiquarks), all numbers are summarized in Table 1.3. With known all quark quantum numbers, the hypercharge, which

flavour	I_3	S	C	B	T	$\mathfrak{B}$	Y
up	1/2	0	0	0	0	1/3	1/3
down	-1/2	0	0	0	0	1/3	1/3
strange	0	-1	0	0	0	1/3	-2/3
charm	0	0	+1	0	0	1/3	4/3
bottom	0	0	0	-1	0	1/3	-2/3
top	0	0	0	0	+1	1/3	4/3

Table 1.3: Quantum numbers of the quarks, I_3 is the third component of isospin, S is the strangeness, C is the charm, B is the beauty, T is the top, $\mathfrak{B}$ is the baryon number and Y is the hypercharge. [3]

combines and unifies the isospin and flavour, can be defined with the help of formula:

$$Y = \mathfrak{B} + S + C + B + T. \tag{1.13}$$

The relationship between charge $Q/|e|$ and hypercharge Y is given by Gell-Mann–Nishijima equation

$$\frac{Q}{|e|} = I_3 + \frac{1}{2}Y. \tag{1.14}$$

Mesons

Mesons have baryon number $\mathfrak{B} = 0$ and are bosons, because with given spin of quarks $\frac{1}{2}$, their total spin is either 0 or 1. They are bound states of quark q and antiquark $\overline{q}$, where flavour of q and $\overline{q}$ can be different. The range for the angular momentum J is given by the relation $|l - s| \leq J \leq |l + s|$, where s is the spin and l is the orbital angular momentum. Then, the parity P is defined to $P = (-1)^{l+1}$ and charge conjugation C is defined to $C = (-1)^{l+s}$ [32].
With this notation, mesons are divided into J^{PC} multiplets. The $l = 0$ states are pseudoscalars (0^{-+}) and the vectors (1^{--}). For $l = 1$, the states are scalars (0^{++}), axial vectors (1^{++} and 1^{+-}) and tensors (2^{++}) [1]. Mesons with higher quantum numbers can exist.
With only u and d quark, four isospin combinations (in analogy to the spin combination) can be made: $\pi^+ = (u\overline{d})$, $\pi^0 = \frac{1}{\sqrt{2}}(d\overline{d} - u\overline{u})$, $\pi^- = d\overline{u}$ form triplet and $\eta = \frac{1}{\sqrt{2}}(d\overline{d} + u\overline{u})$ forms singlet. Adding the s quarks into the set of available quarks gives 9 meson states, one octet and one singlet. Already defined π^+, π^0, π^- are together with $K^+ = (u\overline{s})$, $K^0 = (d\overline{s})$, $K^- = (\overline{u}s)$, $\overline{K}^0 = (\overline{d}s)$ and $\eta = \eta_8 = \frac{1}{\sqrt{6}}(d\overline{d} + u\overline{u} - 2s\overline{s})$ in the octet and $\eta' = \eta_0 = \frac{1}{\sqrt{3}}(d\overline{d}+u\overline{u}+s\overline{s})$ form singlet. Using this nonet, other two singlets $\omega = \frac{1}{\sqrt{2}}(u\overline{u}+d\overline{d})$ and $\phi = s\overline{s}$ are observed in nature, which are linear superposition of η_0 and η_8, can be composed. The mesons can be organised in the weight diagram, already mentioned mesons are in the central planes in the Figure 1.2.
By including the fourth quark c, 16 combination are possible, divided into 15-plet and a singlet. Meson with quark and antiquark of the same heavy flavour is called quarkonium. Specially, it is called charmonium for charm quark and antiquark and bottomium for bottom quark and antiquark. The most well known states of charmonium ($c\overline{c}$) are referred to as J/ψ and $\psi(2S)$.

Baryons

Baryons are bound state of three quarks. They are fermions (the total spin is a multiple of half integer) and their baryon number is $\mathfrak{B} = 1$ ($\mathfrak{B} = -1$ for antibaryons). Our world is primarily made of baryons with u and d quarks. The most common baryons are proton (uud) and neutron (udd), which form the nucleus of each atom.
In analogy with mesons, quarks up, down and strange quark can form baryon octet (baryons with spin and parity $J^P = 1/2^+$) and the baryon decuplet (baryons with spin and parity $J^P = 3/2^+$). Adding the charm quark, the icosuplet are made, one with afore mentioned baryon octet and one with decuplet. Names and composition of these baryons is shown in Figure 1.3.
Similarly, bottom quark can form baryons, but top quark can not due to its short lifetime.

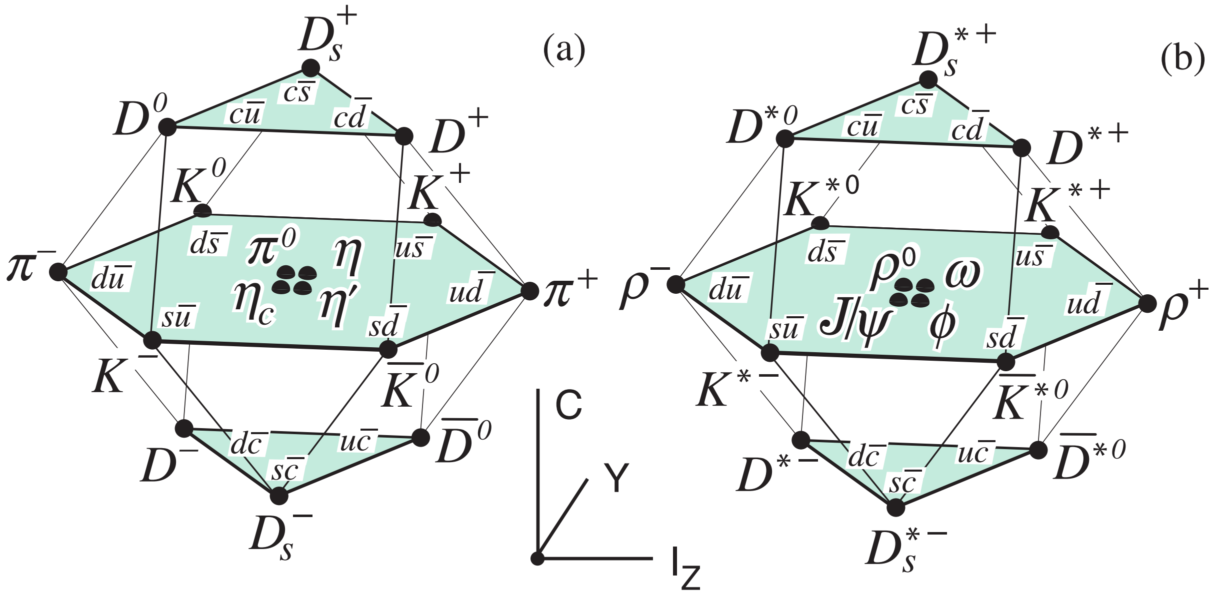

Figure 1.2: Weight diagram showing the 16-plet for the pseudoscalar (a) and vector mesons (b), formed by u, d, s and c quarks. I_z is the third component of isospin, C is the charm and Y is the hypercharge defined by the equation (1.13) [1].

Tetraquarks and pentaquarks

New structures of quarks and antiquarks have been recently observed, which cannot be classified either as meson or baryons. In 2007, the observation of the $Z(4430)$ state, a $c\bar{c}d\bar{u}$ tetraquark candidate, was announced by the Belle experiment in Japan. The existence of $Z(4430)$ was confirmed in 2014 at the LHCb experiment[18].
After this observation, it is not surprising, that also pentaquark state was observed, namely the $J/\psi p$ resonance in $\Lambda_b^0 \to J/\psi K^- p$ decays.[19] The quark content of this pentaquark is expected to be $c\bar{c}uud$.

1.1.5 Antiparticles

Antiparticles were predicted in 1929 by Paul Dirac[20]. Antiparticles are objects with the same mass as the corresponding particles (fermions and bosons), but they have opposite sign of electric and colour charge. According to Dirac, the vacuum consists of sea (often called Dirac sea), where negative energy levels are possible[6]. By transferring the energy $E > 2m_0c^2$ to the negative energy electron, it can be lifted into the positive energy state, from which electron and its antiparticle positron can be created. The transferred energy to e^+e^- creation can be considered as the energy of γ-ray in the presence of the nucleus. The opposite process is also possible, an e^+e^- bound state, called positronium, can annihilate to

[6] Negative energies may occur in quantum mechanics and are included in the relativistic relation $E = \pm\sqrt{p^2c^2 + m^2c^4}$.

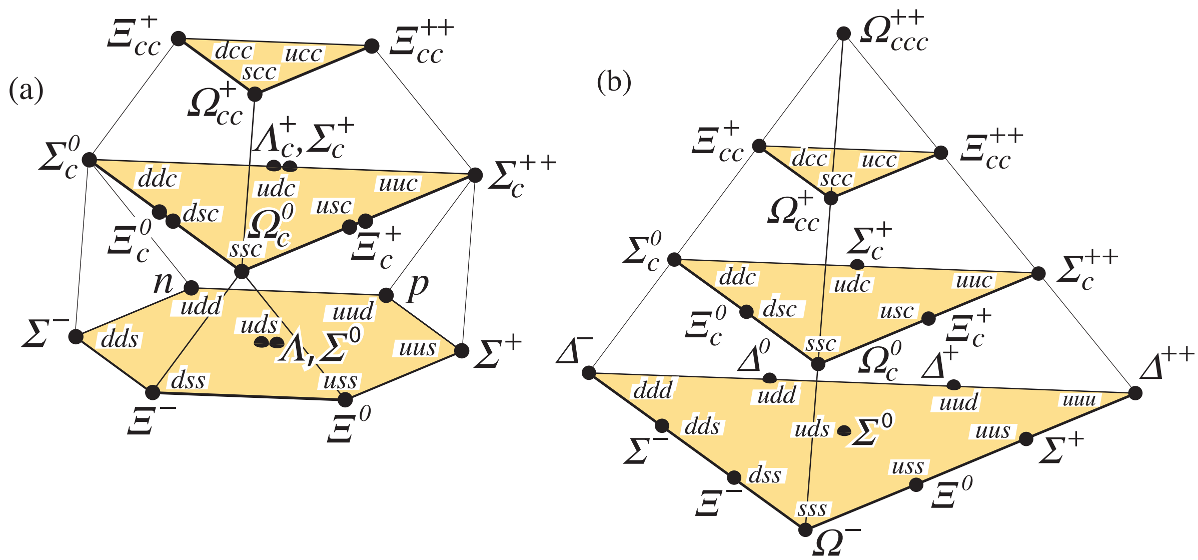

Figure 1.3: Weight diagram showing baryons formed by u, d, s and c quarks, (a) is the icosuplet with octet and (b) is icosuplet with decuplet. Note that there are two Ξ_c^+ and two Ξ_c^0 resonances on the left [1].

two or three γ-rays, but not only to a single γ-ray, due to the total momentum conservation. The first antiparticle was discovered in 1932 in a cloud chamber exposed to cosmic rays. Later, other antiparticles were discovered, but not all particles have its antipartner, for example, the boson Z^0 or γ is particle and its own antiparticle simultaneously.

1.2 GIM mechanism and CKM matrix

In 1963, Nicola Cabibbo[22] found, that the mass eigenstate and the interaction eigenstate of down and strange quark differ in the weak interaction. Denoting d, s the mass eigenstate and d', s' the interaction eigenstate of down and strange quark, the relation between them is described by the Cabibbo angle $\theta_C \simeq 12.9°$

$$d' = d\cos\theta_C + s\sin\theta_C. \tag{1.15}$$

From this equation, the quark interaction eigenstates known in that time can be written in the doublet $\binom{u}{d'}$. Knowing only three quarks at the time, logical choice was to use two quarks with the charge $-1/3$.
Seven years later, S. Glashow, I. Iliopoulos and L. Maiani propose the existence of the fourth quark c and the second doublet $\binom{c}{s'}$. The s' is orthogonal to d', therefore the relation between s' and s, d is given similarly to the equation (1.15) by

$$s' = -d\sin\theta_C + s\cos\theta_C. \tag{1.16}$$

From (1.15) and (1.16), the relation between two mentioned bases is the rotation

$$\begin{pmatrix} d' \\ s' \end{pmatrix} = \begin{pmatrix} \cos\theta_C & \sin\theta_C \\ -\sin\theta_C & \cos\theta_C \end{pmatrix} \begin{pmatrix} d \\ s \end{pmatrix}. \tag{1.17}$$

The GIM mechanism was generalised to three families by M. Kobayashi and K. Maskawa[24] in 1973. The general quark mixing transformation with the unitary Cabibbo, Kobayashi, Maskawa (CKM) matrix is

$$\begin{pmatrix} d' \\ s' \\ b' \end{pmatrix} = \begin{pmatrix} V_{ud} & V_{us} & V_{ub} \\ V_{cd} & V_{cs} & V_{cb} \\ V_{td} & V_{ts} & V_{tb} \end{pmatrix} \begin{pmatrix} d \\ s \\ b \end{pmatrix}. \tag{1.18}$$

The matrix is the rotation in the three dimensional space and can be split into the multiplication of three matrices of two dimensional rotation around the first, second and third axis. The diagonal elements are approximately equal $|V_{ud}| \approx |V_{cs}| \approx |V_{tb}| \approx 1$, other elements are much smaller than one, but nonzero. Matrix elements modify the decay amplitude in the weak interaction and in the case that a complex phase appears in the CKM matrix, the CP violation is allowed in the Standard Model.

1.3 QCD

As stated in the section 1.1.2, the quantum chromodynamics (QCD) is a theory describing the strong interaction between quarks and gluons. The QCD potential can be approximated by the Cornell potential [25]

$$V(r) = -\frac{4}{3}\frac{\alpha_S}{r} + kr, \tag{1.19}$$

where α_S is the strong interaction coupling and k is the free parameter. The first term is dominant at small r and it is similar to Coulomb potential, the factor $\frac{4}{3}$ is derived from the 8 colour gluons averaged over three colours and divided by 2 for a historical reason. The linear term in equation is associated with the colour confinement at large r.

1.3.1 Running coupling

The strength of the interaction is given by the coupling constant. However, this constant is dependent on transferred momentum Q and also on the energy scale μ at which the measurement was made. Thus at the first approximation, the running coupling is

$$\alpha\left(Q^2\right) = \frac{\alpha\left(\mu^2\right)}{1 - \beta_0 \alpha\left(\mu^2\right) \ln\left(\frac{Q^2}{\mu^2}\right)}, \tag{1.20}$$

where the $\alpha\left(Q^2\right)$ is equal to $1/137$ for electromagnetic interaction, respectively approximately equal to 1 for the strong interaction, and β_0 is the quantity dependent on the number of freedom n_f (for fermions) and n_b (for bosons),

$$\beta_0 = \frac{1}{12\pi}\left(4n_f - 11n_b\right). \tag{1.21}$$

For QED, there are three families of fermions, $n_f = 3$, and no colour of the photon, $n_b = 0$, so $\beta_0 = 1/\pi$. For QCD, there are three colour of fermions and gluons ($n_f = 3$ and $n_b = 3$), so $\beta_0 = -7/4\pi$.
According to the equation (1.20), the strong coupling increases at larger distance, so it is impossible to free the quark from hadrons. When enough energy to pull the quark out of the hadron is delivered, the colour confinement is observed and another quark-antiquark pair is formed. At smaller distances, the coupling decreases due to the antiscreening of strong interaction and quarks can be considered in hadrons as free particles. This phenomenon is called asymptotic freedom.

1.4 The OZI rule

The OZI rule was proposed by Susumu Okubo, George Zweig and Jugoro Iizuka in the 1960s[26]. It states, that any strongly occurring process will be OZI-forbidden (or OZI-suppressed), if its Feynman diagram can be divided into two independent diagrams by cutting only gluon lines. This explains why some decay modes dominate over other. For example, the charmonium decay (Figure 1.4) into light hadrons is OZI-forbidden (it has low branching ratio) in contrast with the OZI-allowed charmonium decay into the D^+D^- pair[7].

1.5 Collisions and decays

In order to study afore mentioned particles and phenomena, it is necessary to build particle accelerators and detectors. There are two types of detected processes, collisions and decays. The transition amplitude is given by the matrix element

$$M_{fi} = \langle f|\, H_{int}\, |i\rangle \tag{1.22}$$

of the interaction Hamiltonian H_{int} between final $|f\rangle$ and initial $|i\rangle$ states. The reaction rate (rate per unit time) W is expressed throught the matrix element (1.22) in Fermi's Second Golden Rule

$$W = \frac{2\pi}{\hbar}\left|M_{fi}\right|^2 \rho_f, \tag{1.23}$$

[7] The charmonium state has to have enough energy to decay to this pair. Charmonia under this threshold (the rest mass of charmonium state is smaller than the D^+D^- rest mass) decay through electromagnetic interaction.

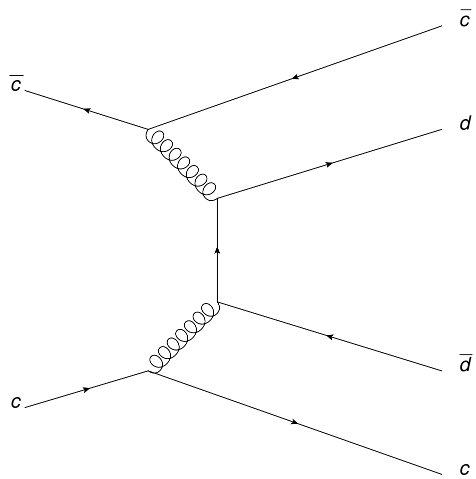

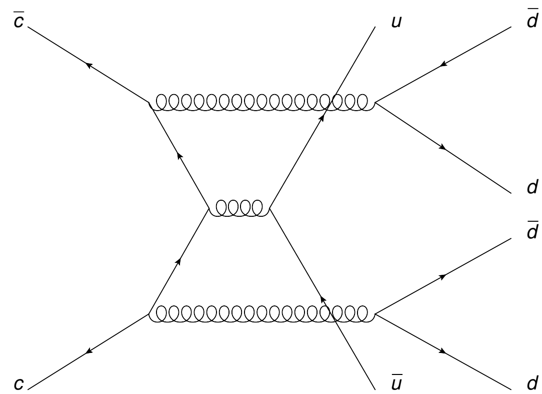

Figure 1.4: OZI rule. OZI-allowed decay of charmonium into a D^+D^- pair on left, OZI-suppressed decay of a charmonium state into light hadrons. [27]

where ρ_f is the energy density $\mathrm{d}N/\mathrm{d}E$ of final states.
Using this relation, the energy width of the state is given

$$\Gamma = \frac{\hbar}{\tau} = \hbar W = 2\pi \left|M_{fi}\right|^2 \int \rho_f \mathrm{d}\Omega, \tag{1.24}$$

where τ is the mean lifetime of the system and is related to the reaction rate W.

1.5.1 Luminosity

Two bunches with N_1 and N_2 particles (usually protons, antiprotons, nuclei) are collided in accelerator with frequency f. Assuming the Gaussian profiles of each bunches in all dimensions, the luminosity is defined to be

$$\mathscr{L} = \frac{N_1 N_2 f N_b}{4\pi\sigma_x\sigma_y}, \tag{1.25}$$

where σ_x and σ_y are standard deviations of the gauss distribution in vertical and horizontal direction and N_b is number of bunches. The dimension of the luminosity is $\mathrm{cm}^{-2}\mathrm{s}^{-1}$ and typical values of luminosity are usually around $(10^{30}\text{-}10^{38})\,\mathrm{cm}^{-2}\mathrm{s}^{-1}$.

1.5.2 Resonances in collider experiments

Large amount of particle is created in the collision. Particles with finite lifetime are called resonances and usually decay into another particles. The cross-section, defined by the reaction rate W and luminosity L

$$\sigma = \frac{W}{L}, \tag{1.26}$$

is given for resonances by Breit-Wigner formula

$$\sigma\left(E\right)=\frac{4\pi\lambda\!\!\!^{-}\left(2J+1\right)}{\left(2s_{a}+1\right)\left(2s_{a}+1\right)}\frac{\Gamma^{2}/4}{\left[\left(E-E_{R}\right)^{2}+\Gamma^{2}/4\right]},\tag{1.27}$$

where s_a and s_b are spins of the incident and target particles, J is the spin of the resonance, E_R is the resonance energy and Γ is the total width of resonance, which is the sum of the partial widths for each channel

$$\Gamma=\sum_{i}\Gamma_{i}.\tag{1.28}$$

Each channel i is characterised by the branching ratio

$$R_{i}=\frac{\Gamma_{i}}{\Gamma}.\tag{1.29}$$

Chapter 2

Quarkonia

The quarkonium is a bound flavourless state of quark and antiquark of the same flavour. In the case the quark is charm, the state is called charmonium, in case of the bottom quark it is called bottomium. The states made of light quarks are not considered as quarkonium due to their small mass and also because the light unflavoured mesons make quantum mechanical mixture of the light quark states.
The quarkonia are due to the large mass of constituent quarks almost nonrelativistic, $\beta \approx 0.2$ for charmonium, so their spectra are similar to the positronium state or the hydrogen atom. However, unlike the positronium state, which is bound only by the electromagnetic interaction (Coulomb force), the quarks are attracted in the quarkonium state by the strong force. This similarity is helpful, because the Cornell potential ((1.19) in section 1.3 of the chapter 1) is similar to the Coulomb potential $\sim 1/r$ at small distances, so the strong interaction can described with help of charmonia. The binding of charmonia and bottomonia is usually described by the non-perturbative QCD due to the fact that typical binding energies are at the edge of QCD pertubativity ($\alpha_s \ll 1$).
Apart from this purpose, quarkonia are useful in measuring the quark gluon plasma (QGP) temperature (for example J/ψ is melting at different temperature than $\psi(2S)$). Charmonia are used for B hadron identification (it is "standard candle" to identify decays of B mesons using displaced J/ψ decay vertices) and last but not least it is widely used in detector performance studies for the measurement of the detector reconstruction efficiency and the detector resolution.

2.1 The J/ψ and $\psi(2S)$ discovery

As written in the section 1.1.4 of the previous chapter, Zweig and Gell-Mann independently proposed theory, which predicted existence of quarks d, u and s. The existence of the fourth quark, named charm, was predicted in 1964 by Sheldon Glashow and James Bjorken. Six years later, Sheldon Glashow, John Iliopoulos, and Luciano Maiani showed the importance of charm quark in the Zweig's quark model, the charm quark allows a theory (GIM mechanism) that has flavour-conserving Z^0-mediated weak interactions but no flavour-changing ones. Finally on 11^{th} November 1974, Burton Richter at SLAC[1][29] and Samuel Ting at BNL[2][28] announced independently the discovery of particle J/ψ, which consists of two quarks, c and $\bar{c}$, therefore the existence of charm quark was confirmed. The discovery of the excited charmonia state $\psi(2S)$ was also announced[30].

2.1.1 Samuel Ting at BNL

Samuel C. C. Ting studied with his collaborators from the MIT[3] the behaviour of timelike photons in the $p+p \to e^+ + e^- + X$ reactions and also searched for a new particle decaying into e^+e^- and $\mu^+\mu^-$ pairs. They used the the proton beam from the BNL synchrotron, which was directed at the beryllium target. Resulting muons, electrons and positrons from the collision were detected by the two-arm spectrometer. The bending was provided vertically by two magnets to measure the angle and momentum of created particles independently. Two Cherenkov detectors filled with the hydrogen were installed to extract muons, electrons and positrons from hadrons. The main detection was provided by eleven planes of proportional chambers. The spectrometer was able to map the e^+e^- mass region of $1-5$ GeV.
During their measurement, they have observed a peak between 3 and 3.25 GeV. For this reason, the track reconstruction was made again and the narrow peak was at $m_{e^+e^-} = 3.1$ GeV with the mass resolution 20 MeV. Some tests to exclude the spectrometer fault were made and the discovery of the particle J was announced on 11^{th} November 1974 [14].

2.1.2 Burton Richter at SLAC

Burton Richter with his research team built the collider called SPEAR. There, the physics goal was to measure the total cross-section of the annihilation of electrons and positrons to hadrons as a function of the central mass energy $\sqrt{s}$ in 200 MeV steps. The enhancement of the cross-section was observed at the central mass energy $\sqrt{s} = 3.2$ GeV. The measurement of the cross-section at $\sqrt{s} = 3.1$ GeV was inconsistent. Richter realized, that this would be caused by the narrow resonance, so they decided to repeat the measurement around this energy with finer energy steps. They have observed a peak in the region $\sqrt{s} =$ 3.10-3.12 GeV, where the cross-section rose from 25 nb to maximum value of (2300 ± 200) nb[31]. In this measurement, the upper limit of the full width of the peak was estimated to be $\Gamma_{max} = 1.3$ MeV (using the Breit-Wigner formula and measured total cross-section 800 nb, the estimated width is $\Gamma_{e^+e^-} = 87$ keV [2]). This narrowness is caused by OZI rule (chapter 1, section). The particle ψ does not have enough energy to decay via the OZI-allowed channel, therefore it decays via the OZI-suppressed channel. For this reason, the mean lifetime is higher than was expected and therefore according to the equation (1.24) (section 1.5 of the previous chapter), the width is small.
Moreover, the Richter's group determined the angular momentum of the discovered particle

[1]Stanford Linear Accelerator Centre
[2]Brookhaven National Laboratory
[3]Massachusetts Institute of Technology

named ψ. The e^+e^- annihilation to hadrons is presumed to go through the virtual photon, which has the angular momentum, the parity P and charge parity C (defined in the section 1.1.1 in chapter 1) equal to $J^{PC} = 1^{--}$. Because the ψ particle and photon amplitude can interfere, it was assumed in respect with the experimental results that the quantum numbers of the ψ are $J^{PC} = 1^{--}$.

2.2 The spectrum of charmonium state

In addition to J/ψ and $\psi(2S)$, other charmonia state were discovered, but only charmonia with $J^{PC} = 1^{--}$ can be accessed in the e^+e^- or $\mu^+\mu^-$ channel.

The charmonium state notation. The charmonia levels in the spectrum are described with the invariant mass, the total angular momentum and with the eigenvalues of the parity and charge conjugation. The vector of the total angular momentum is sum of the angular momentum vector $\mathbf{L}$ and the spin vector $\mathbf{S}$,

$$\mathbf{J} = \mathbf{L} \oplus \mathbf{S}, \tag{2.1}$$

where the $\mathbf{S} = \mathbf{s_c} + \mathbf{s_{\bar{c}}}$ is the vector sum of charm and anticharm spins.
Therefore with respect to the charm and anticharm quark spins $s_c = s_{\bar{c}} = \frac{1}{2}$, the total spin S takes values 0 or 1 and charmonia can form singlet and triplet. The angular momentum takes positive integer values or zero, $L = 0, 1, 2, 3, \dots$. Usually, the notation from the atomic physics is used, where the state with increasing angular momentum L are named $L = S, P, D, F, \dots$.
The radial quantum excitation number n_r is another value describing the quantum state [32]. Thus, each charmonia state is also described in the spectroscopic form [32]

$$(n_r + 1)^{(2S+1)} L_J, \tag{2.2}$$

for example J/ψ is represented as 1^1S_1 state and $\psi(2S)$ as 2^1S_1 state. The lowest charmonium state is 1^1S_0 (η_c).
With knowledge of the angular momentum L, the eigenvalue of the parity operator can be derived, $P = (-1)^{L+1}$. Moreover, using the spin S, the eigenvalue of the charge conjugation is $C = (-1)^{L+S}$. Then the J^{PC} notation can be defined. It is put to use in section 2.1.2 and in Figure 2.1.

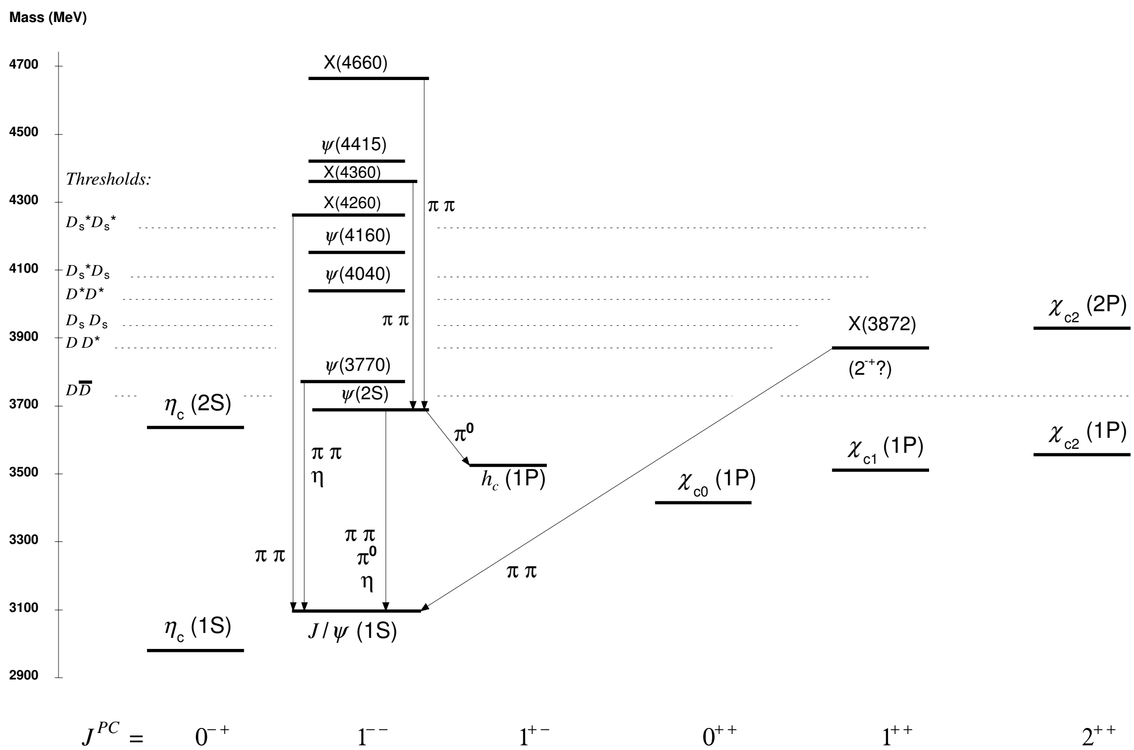

Figure 2.1: The charmonium states with the thresholds for various pairs divided using the J^{PC} notation [1].

Chapter 3

The ATLAS detector at the LHC

To study and verify the predictions of the Standard Model and discover the physics beyond its boundaries, particle accelerators and corresponding detectors are as exploration tools used. In this apparatuses, charged particles are accelerated to nearly the speed of light by the electromagnetic fields, then collided and secondary particles are studied. The most well known colliders are the Large Hadron Collider (LHC) at CERN[1], Relativistic Heavy Ion Collider (RHIC) at Brookhaven National Laboratory and Tevatron at Fermilab. All these colliders are circular accelerators. The Stanford Linear accelerator Center (SLAC) is the other type of accelerator, the linear accelerator, which is suitable for accelerating and colliding light electrons which would otherwise suffer from synchrotron accelerating losses in a circular accelerator.

3.1 The Large Hadron Collider

The Large Hadron Collider is the most powerful particle collider ever built. It is located in an underground 27 kilometres in circumference at the France–Switzerland border near Geneva, Switzerland.

3.1.1 History of LHC

The first proposal of the Large Hadron Collider was presented in 1984 on the CERN and ECFA[2] workshop in Lausanne, Switzerland. In this proposal, the excavated tunnel for Large Electron-Positron Collider (LEP) at CERN would be later used for the LHC. The excavation of this tunnel was completed in 1988 and the LEP collider started operation in August 1989 with the total beam energy of 45 GeV for accelerated electrons and positrons. These particles were preaccelerated and injected in to the main LEP ring by the Super

[1]European Organization for Nuclear Research (in French: Conseil Européen en pour la Recherche Nucleaire), www.cern.ch.

[2]European Committee for Future Accelerators, ecfa.web.cern.ch.

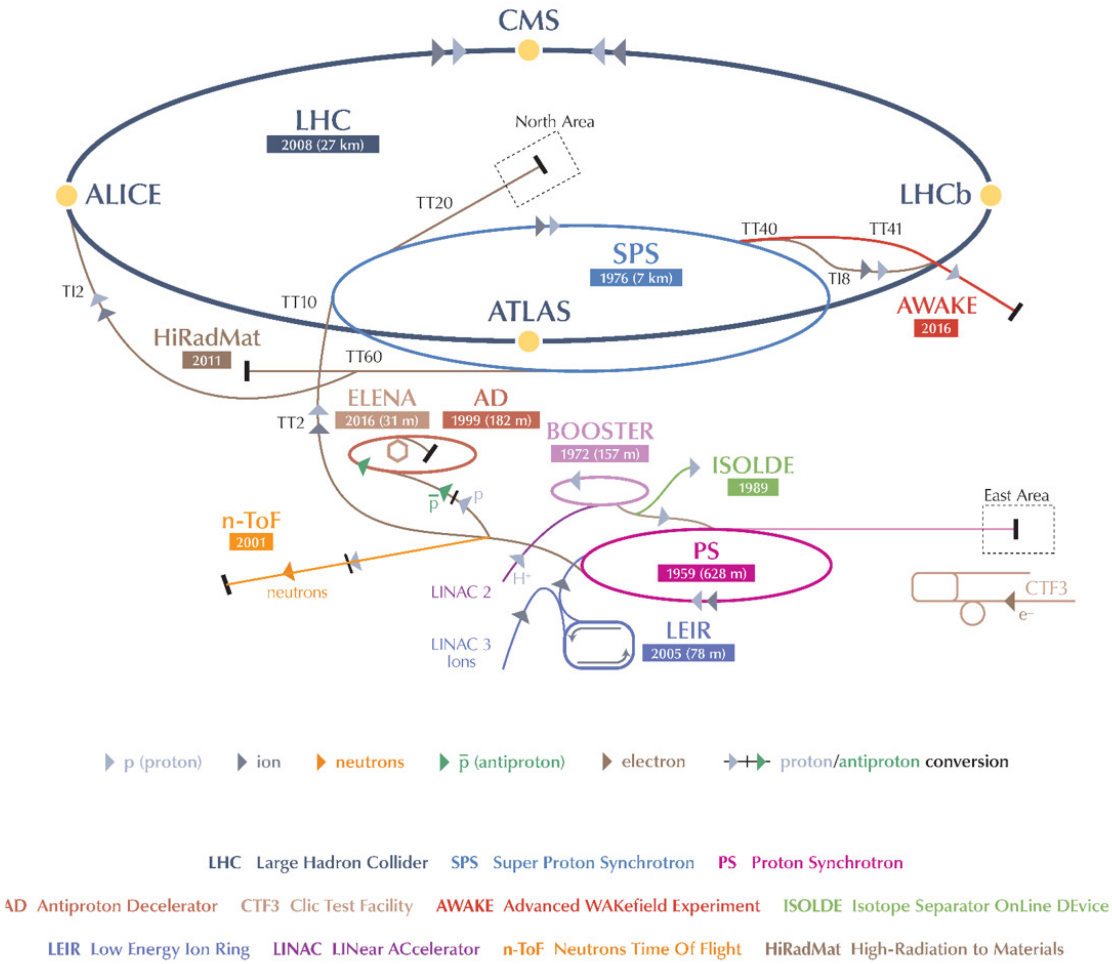

Figure 3.1: The CERN accelerator complex. The proton chain starts in the LINAC 2, the ^{208}Pb chain starts in LINAC 3. The nuclei then travel through the BOOSTER (LEIR for ^{208}Pb), PS, SPS and are collided in the LHC main ring. The accelerating sequence is described in the section 3.1.2 [33].

Proton Synchrotron (SpS), the older accelerator and collider used previously as independent accelerator of protons (later protons and antiprotons, Sp$\bar{\text{p}}$S) between 1981 and 1984. During the LEP era, it was included into the LEP (later LHC) accelerator chain. The LEP center of mass energy reached its maximum of 209 GeV in 2000 and at the end of the year, the LEP Collider was shut down due to the construction of the LHC.
The CERN council approved the construction of the Large Hadron Collider in 1994 and the design report of the LHC was published in 1995. The ATLAS, CMS and ALICE experiments were approved in 1997, the LHCb experiment a year later. After years of construction, the LHC operation was started on September 10$^{\text{th}}$ 2008, but nine days later, a fault forcing a shutdown occured in the electrical bus connection and the helium from the cooling system was released. The LHC was restarted in November 2009. A month later,

LHC was operated with the collisions energy of 2.36 TeV, which set the new world record. After a short technical stop, the LHC was started again with the physics programme and the first collisions at 7 TeV centre-of-mass energy until 2011. Then in 2012, the collision energy was increased to 8 TeV. In this period (2010-2012), denoted as LHC Run 1, among the most important discoveries were the Higgs boson[35], the bottomium state $\chi_b(3P)$ [36] and also observation of a rare decay of B_s meson into two muons andits compatibility with Standard Model predictions. The Run 1 ended in winter 2012, followed by the shutdown LS1.
After shutdown for hardware upgrade, Run 2 started in June 2015 at a record collision energy 13 TeV. This period will last for three years and the second shutdown will follow. The preliminary LHC schedule to year 2035 is shown in Figure 3.2.

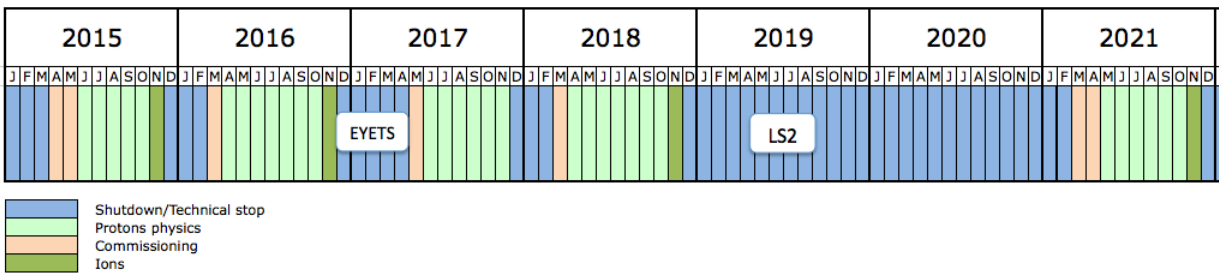

Figure 3.2: The outline LHC schedule out to 2021 with the LS2 shutdown and Extended year end technical stop (EYETS)[37].

3.1.2 The LHC accelerator

The main accelerator ring lies in a tunnel 27 kilometres in circumference. It contains two adjacent parallel beam pipes. 1232 dipole magnets located around these pipes are used to bend the beam and 392 quadrupole magnets focus the beam. Another type of magnet is used to focus the beam closer together in order to increase the chance of collision. The operating temperature of magnets is 1.9 K, so the cooling system is filled with the superfluid $^{4}_{2}$He.
Hydrogen is used as source of protons. These protons are sent into the linear accelerator Linac2, where they are accelerated to energy of 50 MeV. Thereafter, the beam continues to the Proton Synchrotron Booster (PSB), that pushes the beam energy to 1.4 GeV. Going through the Proton Synchrotron (PS), which accelerates protons to 25 GeV, they reach the Super Proton Synchrotron, where they are accelerated to 450 GeV. Finally, the protons are injected into the two LHC beam pipes. Finally, they are accelerated to the beam energy (6.5 TeV per beam during Run 2), one beam circulates clockwise and the the other beam circulates anticlockwise. It takes 4 minutes and 20 seconds to fill the LHC ring. After the final acceleration, proton bunches are collided with the frequency 40 MHz (which corresponds to a period of 25 ns). The whole accelerator chain is shown in the Figure 3.1. Not all protons in bunches are collided at the end of LHC fill. The protons in bunches have

large kinetic energy and therefore high destructive power, so they are sent to the beam dump, where they are safely disposed of. The beam dump has blocks several meters long made of copper, aluminium, carbon and beryllium.
In the LHC, besides protons also ^{208}Pb nuclei can by accelerated and collided. They start their journey at the linear accelerator Linac3 and after accumulation in the LEIR storage ring, they are injected into the PS. Then, the acceleration process is the same as for protons [34].

3.1.3 Detectors at the LHC

The beams in both pipes are collided at four locations around the accelerator ring. At these places, four large (have own interaction point)and three small ones (share the collision point with one of the large detector) are build.

ATLAS **A** **T**oroidal **L**HC **A**pparatu**S** is a multi-purpose detector. It is built to serve the purpose of allowing study the particle physics beyond the Standard Model. ATLAS was built to discover the basic block of matter, to investigate properties of the previously undiscovered Higgs boson or the asymmetry between the behavior of matter and antimatter, known as CP violation [38].

CMS The **C**ompact **M**uon **S**olenoid was built with similar purpose as ATLAS. The main goals of this experiment are same as the goals of ATLAS, but CMS and ATLAS use different technical solutions and design of its detector magnet system [38].

ALICE **A** **L**arge **I**on **C**ollider **E**xperiment is a detector built primary to detect particles originating in the heavy ion collisions. At these collisions, the temperature much higher than inside the Sun is reached and also the signs of the quark gluon plasma state[3] (QGP) is possibly observed [38].

LHCb **L**arge **H**adron **C**ollider **b**eauty is designed to study the difference between matter and antimatter by studying the properties of mesons and baryons witch contains the b quark. LHCb is also capable to perform measurements of electroweak physics in the forward region [38].

LHCf **L**arge **H**adron **C**ollider **f**orward is an experiment intended for studying astroparticle (cosmic ray) physics. It is built at the same collision point as ATLAS. It uses particles thrown in the forward direction by collisions as a source to simulate cosmic rays [38].

[3]The state few milliseconds after the Big Bang, where quarks and gluons are free.

TOTEM The full name of this experiment is **TOT**al cross section, **E**lastic scattering and diffraction dissociation **M**easurement at the LHC. It shares the collision point with the CMS. The detector aims at the measurement of total cross section and elastic scattering in forward region [38].

MoEDAL

The **Mo**nopole and **E**xotics **D**etector **a**t the **L**HC is located near the LHCb experiment. The main goal of this detector is the search of the magnetic monopole, a hypothetical particle with a magnetic charge. MOEDAL also looks for highly ionizing Stable Massive Particles (SMPs), predicted by theories beyond the Standard Model[38].

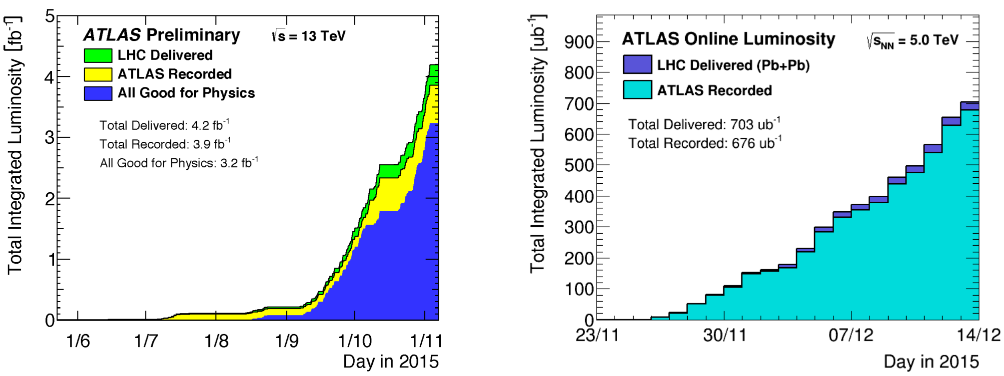

Figure 3.3: The total integrated luminosity at the LHC and ATLAS during 2015 in proton-proton collision (left) and in ^{208}Pb-^{208}Pb collision (right).

3.2 A Toroidal LHC ApparatuS

The ATLAS is a multi-purpose detector on the Large Hadron Collider. It is placed 100 m below ground near the village Meyrin in Switzerland. With the weight 7000 tonnes, length 46 m, 25 m height and 25 m width, ATLAS is in the fact the largest particle collider detector ever constructed. It is designed to detect particles from the proton-proton collision at the luminosity 10^{34} cm^{-2}s^{-1} and the energy 14 TeV and the ^{208}Pb-^{208}Pb collision at the luminosity 10^{27} cm^{-2}s^{-1} and the energy 5.5 TeV per nucleon pair. The total integrated luminosity of the LHC and ATLAS during 2015 running is shown in the Figure 3.3. ATLAS consists of several subdetectors with the different pseudorapidity[4] coverage, the largest one $|\eta| < 4.9$ is in the forward hadronic calorimetry. The ATLAS detector is forward-backward symmetric with respect to the interaction point. It consists of the 4 detector systems and solenoidal and toroidal magnet systems. The innermost subdetector is the Inner Detector (ID), which is responsible for the measurement of trajectories of charged particles. The ID

[4]The pseudorapidity detector coordinate is defined as $\eta = -\ln\tan(\Theta/2)$, where Θ is the polar angle from the beam axis.

is surrounded by the Electromagnetic and Hadronic Calorimeters, the devices measuring the energy of a particle passing through the detector, the Electromagnetic Calorimeter detect especially light particles interacting via the electromagnetic force, like electrons, positrons, muons and photons. On the contrary, the Hadronic Calorimeter detects hadrons and mesons. The outermost layer is the Muon Spectrometer, which is designed to measure the muon momentum with excellent resolution (80 μm per chamber of Monitored Drift Tubes [39]). The view of the ATLAS detector with its subdetectors is shown in the Figure 3.4.

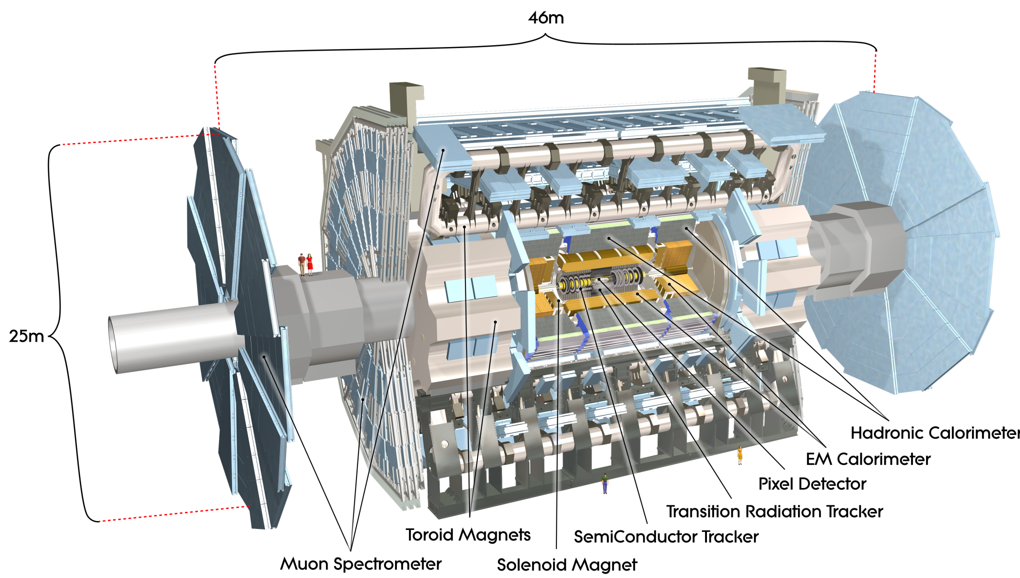

Figure 3.4: The ATLAS detector with its subdetectors [39].

3.2.1 Magnet system

The ATLAS magnet system is 22 m wide and 26 m long [39] and consists of four large superconducting magnets, one solenoid, one barrel toroid and two end-cap toroids (see Figure 3.5).

The Central Solenoid Magnet lies between the ID and Electromagnetic Calorimeter. It is capable to produce a 2 T axial field. This magnet has to be thin in order to not shield particles travelling from Inner Detector to Calorimeter, so the inner and outer diameters are 2.46 m and 2.56 m. Its axial length is 5.8 m. Because this magnet works at temperatures close to absolute zero, the heat shield made of 2 mm thick aluminium panel is added.

The Barrel Toroid consists of eight coils. The overall length of this toroid system is 25.3 m, the inner and outer diameters are 9.4 m and 20.1 m. Each coil is separated and surrounded by cryostats. It produces 0.5 T toroidal magnetic field for the muon spectrometer in the

central region.
Similarly to the Barrel Toroid, both End-cap Toroids consist of eight coils, but they are rotated by 22.5° with respect to the Barrel Toroid. Each end-cap toroid produces 1 T magnetic field for the muon spectrometer in the end-cap region.

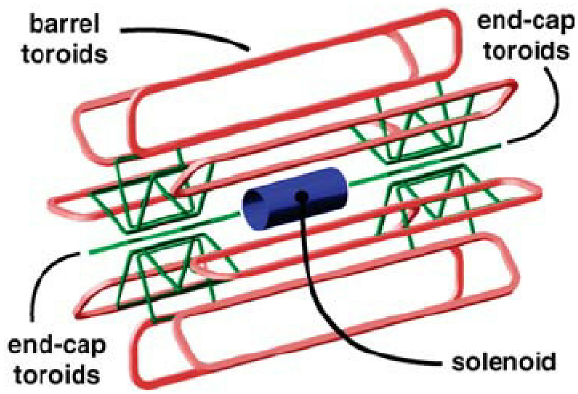

Figure 3.5: The ATLAS magnet system [40].

3.2.2 Inner Detector

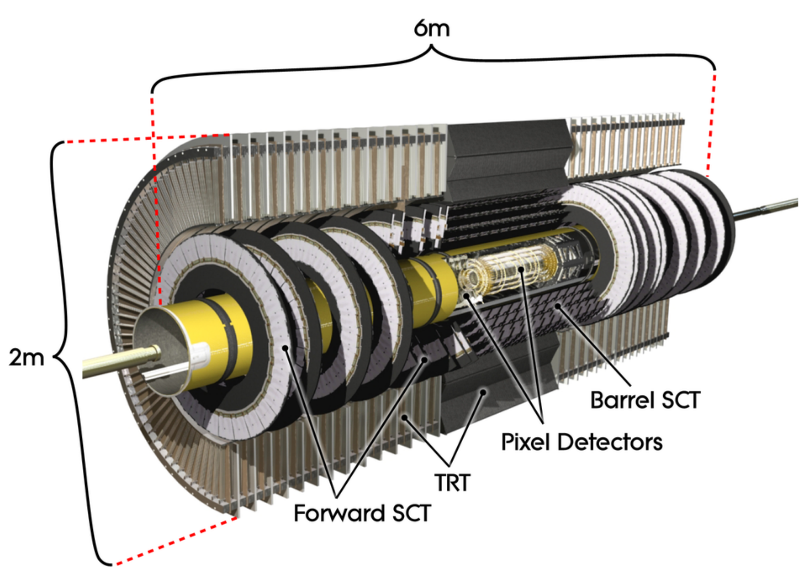

Figure 3.6: The ATLAS Inner Detector with its parts [39].

The Inner Detector covers the pseudorapidity $|\eta| < 2.5$ and full azimuthal angle Φ. It is built few centimetres form the beam axis and its radius is 1.2 m and length is 6.2 m. It provides excellent momentum resolution and vertex reconstruction for charged particles. The

Inner Detector consists of Pixel Detectors, SemiConductor Tracker (SCT) and Transition Radiation Tracker (TRT). In the barrel section, Pixel Detector and SCT form cylinders around the beam axis, in the end-cap regions they are located on disks perpendicular to the beam axis. The barrel TRT straws are parallel to the beam direction. The ID immersed in a 2 T magnetic field produced by the central superconducting solenoid. The cut-away view of the ATLAS Inner Detector is shown in the Figure 3.6.

Pixel Detector

The innermost part of the Inner Detector is the Pixel Detector. It is a system of four layers, the Insertable B-Layer (IBL) was installed during the first long shutdown (2013-2014)[41]. The pixel detector consists of four barrels and of three disks at a distance 59.5 m on each side. This distribution provides three measurement points of each particle travelling from the collision with the maximal pseudorapidity $|\eta| < 2.5$. The Pixel Detector is composed of modules, each module contains 47232 pixels. About 90% of pixels has the area of $50 \times 400\ \mu\text{m}^2$, the size of the remaining pixels is $50 \times 600\ \mu\text{m}^2$ (ganged pixels) and $50 \times 250\ \mu\text{m}^2$ (IBL). The intrinsic accuracy of each pixel layer is 10 μm in $R - \Phi$[5] and 115 μm in z. To reduce the leakage current, the sensors are operated between $-5°$C and $-10°$C.

SemiConductor Tracker

The SemiConductor Tracker (SCT) is the middle component of the Inner Detector and encloses the Pixel Detector. It is composed of four layers and provides four hits per track in ideal case. The SCT is especially used for the measurement of momentum. Each layer consists of the barrel modules, that are mounted on cylinders at radii of 29.9 cm, 37.1 cm, 44.3 cm, and 51.4 cm. The SCT consists of 4088 silicon strip sensors forming four cylindrical barrel and two end-caps of nine disks each. The strips in the barrel SCT are parallel to the field produced by the solenoid.

Transition Radiation Tracker

The Transition Radiation Tracker (TRT) is a combination of a straw tracker and a transition radiation detector and it is the outermost part of the Inner Detector with the inner radius of 55.4 cm and outer radius of 108.2 cm. The basic TRT elements are polyamide drift (straw) tubes. Each straw is 4 mm in diameter, the maximum length 144 cm in the barrel and 37 cm in the end-cap region and they are are filled with xenon and carbon dioxide gas. The barrel contains about 50000 straws and the end-caps contain 320000 radial straws. The spatial resolution of each straw is 170 μm. These allow the detector to distinguish two types of hits, the tracking hits (pass the lower threshold) and transition radiation hits(pass the higher threshold). The particle with the transverse momentum $p_{\text{T}} > 0.5$ GeV

[5]The distance ΔR in the pseudorapidity-azimuthal angle space is $\Delta R = \sqrt{\Delta\eta^2 + \Delta\Phi^2}$.

and pseudorapidity $|\eta| < 2$ travelling through the TRT should cross typically more than 30 straws.

3.2.3 Calorimeters

Both electromagnetic and hadronic calorimeter are outside the solenoidal magnet. They are designed to measure the energy of incoming particle by absorbing it with creation of the electromagnetic or hadronic shower. The ATLAS calorimeter system consists of a number of detector. The electromagnetic calorimeters, which are closest to the beam axis are situated in the cryostats, are divided into three parts, a barrel and two end-caps. There is the electromagnetic barrel calorimeter in the barrel cryostat, end-caps contain an ElectroMagnetic End-cap Calorimeter (EMEC), Hadronic End-cap Calorimeter (HEC) behind the EMEC and Forward calorimeter (FCal) closest to the beam axis. The outer calorimeters are scintillator tile barrel and two extended tile barrels. The cut-away view of the ATLAS calorimeter system is shown in Figure 3.7.

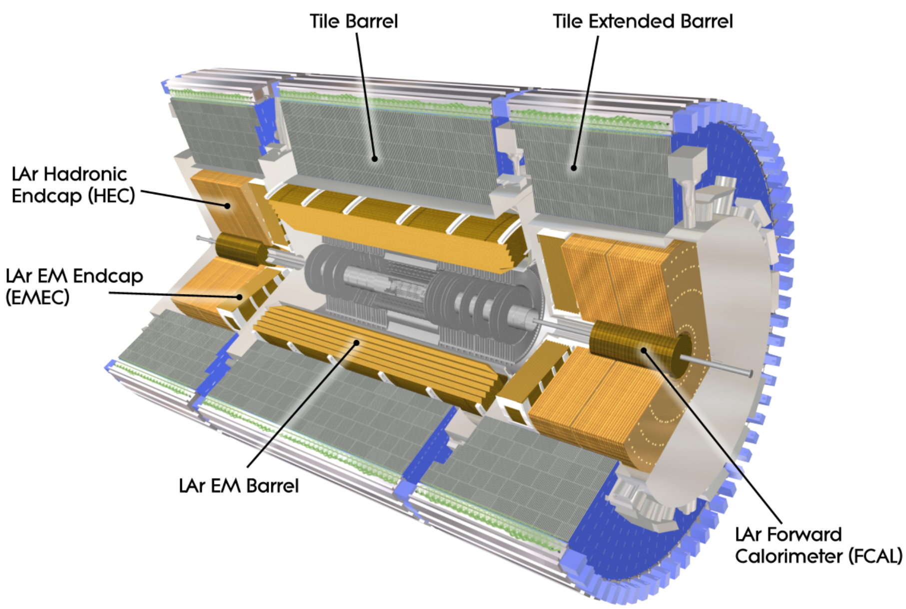

Figure 3.7: The ATLAS calorimeter system [39].

Electromagnetic Calorimeters

The electromagnetic (EM) calorimeters detect photons and charged particles interacting through the electromagnetic interaction. They deposit their whole energy producing an electromagnetic shower. Lead and stainless steel are used as the energy absorbing material and the liquid argon (LAr) filling EM calorimeters is used as the sampling material due to its stability of response over time. The geometry of calorimeter allows the calorimeters to have several active layers, three in the precision-measurement region $0 < |\eta| < 2.5$, two in the region $2.5 < |\eta| < 3.2$ and one in the overlap region between the barrel and the EMEC. This results to the overall EM calorimeters coverage of the pseudorapidity $\eta < |3.2|$.

Hadronic Calorimeters

In contrast with the electromagnetic calorimeter, the hadronic calorimeter detects the particles interacting through the strong interaction, primary the hadrons, which annihilate with the production of the shower. The scintillator tiles are used as sampling medium and for the absorber medium is used steel. The ATLAS hadronic calorimeter system consists of tile calorimeter and and two hadronic end-cap calorimeters (HEC). The tile calorimeter with inner radius 2.28 m and outer radius 4.25 m itself consists of one central barrel and two extended barrels. The barrel part covers the region $\eta < |1.0|$ and extended barrels cover region $0.8 < |\eta| < 1.7$. The tile calorimeter with its extended parts is divided in to three layers.
The LAr (liquid argon) hadron end-cap calorimeter (HEC) uses the copper plates with the LAr gaps as the active medium. Located behind the end-cap electromagnetic calorimeter, with the same LAr cryostats, it is composed of two wheels at each end-cap. Each wheel is segmented into two layers, totally four layers per end-cap region. The HEC overlaps with the pseudorapidity coverage $1.5 < |\eta| < 3.2$ in to the extended tile calorimeter region.
The LAr Forward Calorimeter (FCal) is the outer part in the end-cap cryostat and it consists of three parts, one part made of copper to provide electromagnetic measurements and two parts made of tungsten measure the energy of hadronic interactions. The FCal overall covers the pseudorapidity $3.1 < |\eta| < 4.9$.

3.2.4 Muon Spectrometer

Muons unlike other charged particles are not stopped by the Inner Detector and Calorimeters. To measure their momentum and trajectory, the outermost part of the ATLAS detector system, the Muon Spectrometer, is used. The measurement is based on the examination of the muon track deflection, induced by the ATLAS magnet system. Muons with the psedorapidity in the range $|\eta| < 1.4$ are deflected by the Barrel Toroid, muons with pseudorapidity $1.6 < |\eta| < 2.7$ are bent by end-cap magnet. In the region $1.4 < |\eta| < 1.6$, the deflection is provided by both Barrel Toroid Magnet and End-cap Toroid Magnet. Thus, the overall pseudorapidity coverage by the muon system is $|\eta| < 2.7$. The coverage is provided by Monitored Drift Tubes (MDT's) over the most η and by Cathode Strip Chambers (CSC's) at large pseudorapidity. The ATLAS muon system has also another purpose, the trigger system (for instance, it provide p_{T} threshold or bunch-crossing identification for the muon spectrometer). This system cover the range $|\eta| < 2.4$ and is formed by Resistive Plate Chambers (RPC's) in the barrel section and Thin Gap Chambers (TGC's) in the end-cap regions.
In the barrel region, the muon chambers are arranged three cylindrical layers around the beam axis. Chambers in the end-cap and transition region are also installed in three layers,

orthogonal to the beam axis. The main parameters of muon spectrometer are in the Table 3.1 and the view of the ATLAS muon system is in the Figure 3.8.

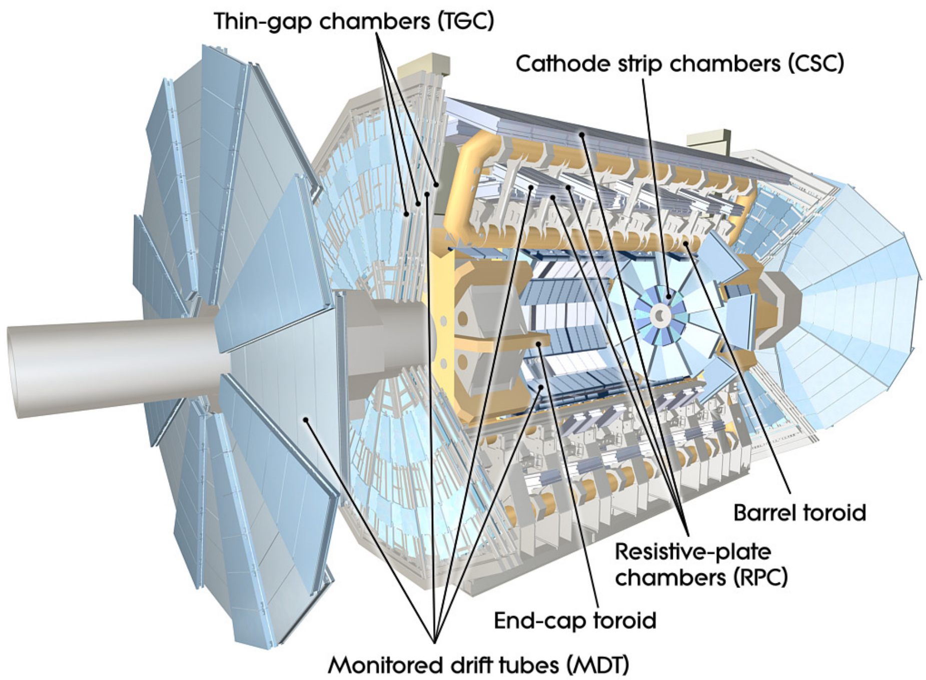

Figure 3.8: The ATLAS muon spectrometer [39].

		Chamber resolution in			Hits/track		Number of	
	Function	z/R	Φ	time	barrel	end-cap	chambers	channels
MDT	tracking	35 μm (z)	-	-	20	20	1150	354000
CSC	tracking	40 μm (R)	5 mm	7 ns	-	4	32	31000
RPC	trigger	10 mm (z)	10 mm	1.5 ns	6	-	606	373000
TGC	trigger	2-6 mm (R)	3-7 mm	4 ns	-	9	3588	318000

Table 3.1: Main parameters of the Monitored Drift Tube (MDT), Cathode Strip Chamber (CSC), Resistive Plate Chamber (RPC) and Thin Gap Chamber (TGC).[39]

Monitored Drift Tubes

Monitored Drift Tubes (MDTs) provide precise measurement of muon momentum in almost all Muon Spectrometer. The basic MDT element is a drift tube with a diameter 29.97 mm and length in a range 0.9 to 6.2 m made of aluminium. The tube is filled with Argon (93%) and Carbon dioxide (7%) at the pressure 3 bar. There is the tungsten-rhenium wire inside the tube, used for the collecting electrons created by the ionization of the gas by incoming particle. Each MDT chamber is formed by two multilayers, which itself consists of three or four layers of the drift tubes. The chambers are equipped with the temperature monitors (for correction of the tube thermal deformation) and aluminium frame supporting the multilayers is fit up with the monitoring system to control the sagging and torsion of the chamber.[42]

Cathode Strip Chambers

Because the MDT has limit of counting rate 150 Hz/cm^2 for safe operation, in the region $|\eta| > 2$, where this limit can be exceeded due to the thermalised neutrons coming from the Calorimeter, the Cathode Strip Chambers (CSCs) are used. CSCs are multi-wire proportional chambers with strip read and form two discs with eight large and eight small chambers each. Each chamber has four CSC plane, so this part provides four independent measurement along each track with the resolution 60 μm in η and 5 μm in the Φ plane. Each chamber consists of four wire planes, so the CSC system provide similar configuration like MDT system, but with higher quality of granularity.

Resistive Plate Chambers

The Resistive Plate Chambers (RPCs) serve as the muon trigger in the barrel region and also provide second coordinate measurements. It consists of three layers around the beam axis, two inner layers surround the middle MDTs and the outer layer is located between the MDT chamber for the large sectors and MDT for small sectors. Two inner RPCs provide the transverse momentum trigger in the range $6-9$ GeV (low-p_{T} trigger) and configuration of inner and outer RPCs provide the p_{T} trigger in the range $9-35$ GeV (high-p_{T} trigger). RPC has two parallel electrode-plates at the distance 2 mm, made of phenolic-melaminic plastic laminate. The filling gas is the mixture of $C_2H_2F_4$ (94.7%), Iso-C_4H_{10} (5%) and SF_6 (0.3%). The electric field in the gas is 4.9 kV/mm, allowing the formation of the avalanches created by the incoming particle. The signal is read out by the metallic strips, which are installed on the outer side of the resistive plates.

Thin Gap Chambers

The Thin Gap Chambers (TGCs) is located in the en-cap region and provide the muon trigger capability and the measurement of the azimuthal coordinate. In the end-cap region, the middle layer of the MDTs is complemented by seven layers of TGCs and the inner layer of the MDTs is complemented by two layers of TGCs, the end-cap (EI) and forward (FI) TGCs. The Thin Gap Chambers do not touch the MDT like the RPCs, but they have own support system or use support system of other parts of the ATLAS apparatus, the EI TGC is for example mounted on the support structure of the barrel toroid coils.
TGC's are multi-wire proportional chambers with the wire-to-cathode distance of 1.4 mm smaller than the wire-to-wire distance of 1.8 mm. The position measurement is made by the strips (azimuthal angle) and wires (pseudorapidity) with pseudorapidity coverage

$1.05 < |\eta| < 2.7$. This together with high electric field around the TGC wires leads to very good time resolution for the majority of the muon tracks. The pseudorapidity region for triggering is $1.05 < |\eta| < 2.4$ and important is that the TGCs used for the position measurement are not used for triggering.

3.2.5 Forward detectors

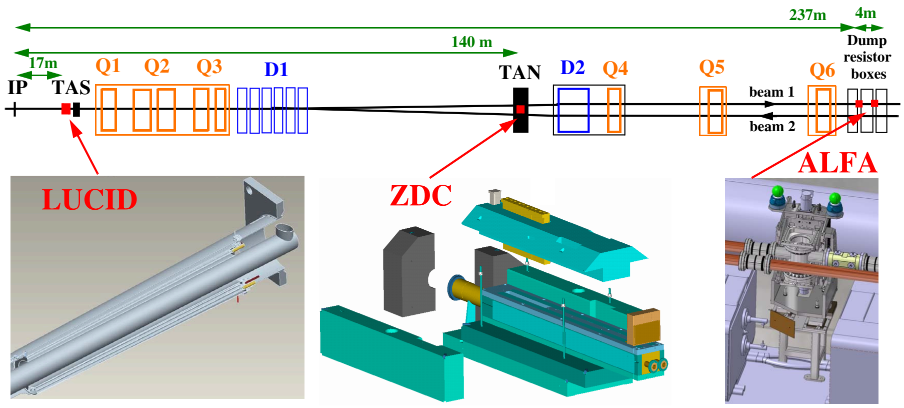

Figure 3.9: The placement of the ATLAS forward detectors [39].

There are three small sets of detector, which provide the good coverage in the very forward region. The placement of the forward detectors is in the Figure 3.9.
The LUCID (LUminosity measurement using Cerenkov Integrating Detector) is located on the beam axis 17 m from the interaction point. It is designed to measure inelastic $p - p$ scattering and to measure online the relative-luminosity.
The ALFA (Absolute Luminosity For ATLAS) is located at 240 m from the interaction point (the most remote detector belonging to the ATLAS domain). It consists of scintillating-fibre trackers and it help determine the absolute luminosity via elastic scattering at small angles. To measure at these angles (3 μrad [39]), the detectors are placed in the Roman pots, which can move as close as 1 mm to the beam axis.
The ZDC (Zero-Degree Calorimeter) is embed in the TAN (Target Absorber Neutral) at 140 m from the interaction point and just beyond this detector, the beam pipe is divided into two separate pipes. It main purpose is the determination of the heavy-ion collision centrality and also it measures neutral particles at pseudorapidities $|\eta| \geq 8.2$.

Chapter 4

The ATLAS Trigger System and Offline Software

4.1 The Trigger and Data Acquisition System

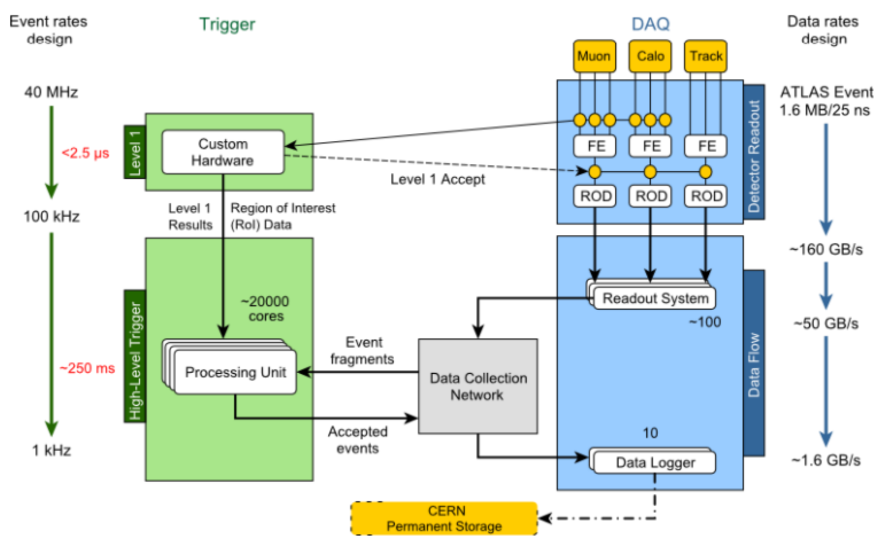

Figure 4.1: The architecture ATLAS Trigger and Data Acquisition System (TDAQ) in Run 2 [44].

Operating at the luminosity of 10^{34} cm^{-2}s^{-1}, the proton-proton bunch crossing rate is 40 MHz [39]. In every crossing bunch dozens of proton interact, the total interaction rate is approximately 1 GHz. Due to the technical limitations, event rate of about 1 kHz (in Run 2) can be recorded, therefore it is important to select events with maximum efficiency in the selected physics channels. This reduction is performed by the Trigger System, which has two distinct levels, L1 and High-Level Trigger (merged L2 and Event Filter)[43]. The ATLAS Trigger and Data Acquisition System in Run 2 is shown in Figure 4.1.

In the first stage of the ATLAS Trigger System, the L1 Trigger reduces the the rate from 40 MHz to 100 kHz. Its decision is formed by the Central Trigger Processor (CTP), which uses information from Muon Spectrometer subdetectors and from all calorimeter subsystems. The L1 Calorimeter Trigger (L1Calo) search events with high transverse energy E_T such as electron, photons, jets and τ-leptons decaying into hadron and also events with large total transverse energy and large missing transverse energy $E_{\mathrm{T}}^{\mathrm{miss}}$. The L1 Muon Trigger receives the signals from the muon trigger chambers RPC and TGC (described in the section 3.2.4 in the chapter 3). It selects events with high-p_{T} muons based on six p_{T} thresholds, where muons are not counted more than in one threshold region.
The L1 Trigger latency is required to be less than 2.5 μs. The decision together with other signals is sent to the detector front-end system by the Timing, Trigger and Control system (TTC). In case the L1 Trigger accepts the event, the information is sent as Region-of-Interest (RoI) to the High-Level Trigger.
High-Level Trigger (HLT) works with additional detector information such as the Inner Detector hits, full information from Calorimeter and from muon detectors. The L2 Trigger inside the HLT reconstruct the track in RoI using fast reconstruction algorithms. When the event passes the L2 Trigger, the Event Filter will classify the selected event and reconstruct the event with complete detector information. The events are stored for offline reconstruction as 'RAW' data and the rate of recording of these events is 1 kHz. The information flow in the beginning with the rate of $\sim$ 10 PB/s is reduced to $\sim$ 1 GB/s. RAW data are converted in the Athena framework into the xAOD data format, which can be used for further analysis.

4.2 Muon reconstruction

The muons are important for the variety of physical processes, including the B-physics and the study of charmonia, because charmonia can decay via the electromagnetic interaction into two oppositely charged muons. While events with these muons are triggered and saved to disk, they are reconstructed using information from the Inner Detector and Muon Spectrometer. Muon track candidate are connected with hits in segments of the detector (especially in the Muon Spectrometer). If the fit used for the hit association satisfies the selection criteria, the track is assigned to muon. There are four types of muons according the muon reconstruction: Combined, Segment-tagged, Calorimeter-tagged and Extrapolated muons.[45]

Combined muons: The reconstruction uses the fitted hits obtained independently by the Inner Detector and Muon Spectrometer. To improve the fit quality, some tracks can be added or removed. This refit can be made for example by the *STACO* or *MuId* algorithm[46]. These muons are use for the J/ψ reconstruction in order to ensure the good quality of the signal.

Segment-tagged muons: When the muon track cross just one layer of the Muon Spectrometer due to the small p_{T}, these muons are used. The tracks in the Inner Detector are assigned to muons and the extrapolated to the hit in the Muon Spectrometer. The common algorithm for these muons is *MuTag.*[47]

Calorimeter-tagged muons: They are lowest purity muons are tracks in the Inner Detector associated with muons and the energy deposited in the Calorimeter but not connected with hits in the Muon Spectrometer. It is located primarily in the region, where is not the Muon Spectrometer coverage because of the support system of the Inner Detector and the Calorimeter. [46]

Extrapolated muons: These muons, also called stand-alone muons, are associated only with the track in the Muon Spectrometer, which are extrapolated to the interaction point. To be classified as this type, the muon has to hit at least two layers of the Spectrometer. The track can be reconstructed for example by the *Muonboy* algorithm. [47]

4.3 Data Format

During the Run 1 phase of the ATLAS experiment, data designated for further physics analysis were saved after reconstruction in AOD(Analysis Object Data) format. These data are not directly readable with ROOT, so they have to be transformed using the Athena software into the DPD format (n-tuple data format), which is readable by ROOT and is more suitable for the following physics analysis. However, this approach has associated large disadvantage, because every physic group handles their own ”derivations” dAOD, which generally contain same information and waste disk space. Moreover, waiting for DPD production takes months in some cases and it is difficult to compare analyses using different DPDs.
In Run 2, data from reconstruction are saved in a new data format xAOD[49]. As shown in Figure 4.2, xAOD format substitutes AOD and DPD format, it is object oriented, so this format is readable both by Athena software and by ROOT. The xAOD is uniform across all reconstructed object types (jets, muons, etc.).
The xAOD consists of information about the event (EventInfo) and information about reconstructed objects within each event (jets, muons, tracks, etc.). These reconstructed objects inherit from a common class Particle. xAOD::EventInfo is only one object of this type for given event and contains current run number, event number, what was the pile-up for given event. Information about objects of particle type (electron, muon, tau, jet, photon, . . .) is saved as class xAOD::IParticle. Here are saved variables such as particle mass, energy, rapidity, transverse momentum and other information about given particle candidate.
Information in xAOD is split into the objects and the Auxiliary Store, where object data are stored as vectors of values. The splitting allows reading of variable across objects without having to going through the full event, for example it enables fast reading in

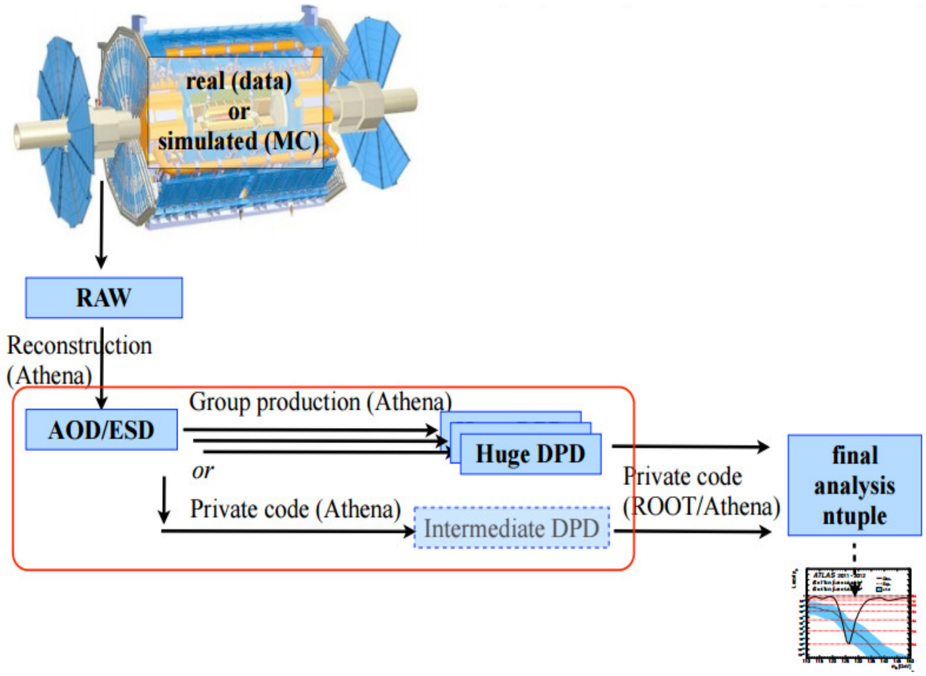

Figure 4.2: The Run 1 analysis model, RAW is a persistent representation of the event data in byte-stream format, AOD is Analysis Object Data, ESD is Event Summary Data and DPD is n-tuple data format. The red rectangle is substituted by xAOD format in the Run 2.[48]

ROOT with TBrowser. Usually, programmers work with object and never need to interact with Auxiliary Store.

4.4 ATLAS Offline Software

4.4.1 The Athena framework

A majority of the ATLAS software is implemented within the Athena, an object-oriented framework designed to provide a common infrastructure and environment for simulation, reconstruction and analysis applications high-energy physics experiment. It is based on C++ and Python and it is an implementation of the underlying Gaudi [52], architecture developed by the LHCb but commonly used by both ATLAS and LHCb.
The Athena is designed to provide an environment for simulation, filtering, reconstruction and analysis applications. It contains a skeleton of an application, into which the developers can plug-in their codes. Also in the Athena, the data in RAW format is transformed into xAOD (formerly AOD) and it serves as a central software repository of all algorithms.

4.4.2 ROOT framework

ROOT [53] is an object-oriented framework and it was originally designed at CERN by René Brun and Fons Rademakers. It has a C/C++ interpreter (CINT) and C/C++ compiler (ACLIC) and can be used as an interactive environment (running code in the command line) or execute scripts. Its large advantage is the ability to handle large files. It is able to make multi-dimensional histograms, curve fitting and storage of analysis results as ROOT files. ROOT provides the Virtual Monte Carlo interface to simulation engines such as Geant 4 and can be also used to develop an event display, an application providing the detector geometry or the particle path visualisation.
ROOT consists of about 3000 classes which contain the low-level building blocks of ROOT. The example of the class is *TFile*, *TObject* or *TClass*. The container classes provide the data structure classes like lists, maps, vectors and others and the trees and N-tuples can be made with the *TTree* and Ntuple classes.[51] The ROOT version 6.04.00 is primarily used to plot histograms in my analysis.

Roofit

Roofit [54] is a library of C++ classes providing the data fitting and modelling in the ROOT framework. In was originally developed for the BaBar collaboration at Stanford Linear Accelerator Center.
Roofit works with the normalised PDFs (Probability Density Functions) describing the probability density of the observables distribution with respect on the parameters of the density function. For example, the Gaussian density function with its parameter is

$$G(x,\mu,\sigma) = \frac{1}{A}\exp\left(-\frac{1}{2}\left(\frac{x-\mu}{\sigma}\right)^2\right), \qquad A = \int_{x_b}^{x_t}\exp\left(-\frac{1}{2}\left(\frac{x-\mu}{\sigma}\right)^2\right)\mathrm{d}x, \tag{4.1}$$

where x is the variable and μ, σ are parameters. If the limits of the integral are maximal and minimal, the integral is due to the normalisation equal to one.
Roofit can be used to perform unbinned and binned maximum likelyhood fits and produce plots. It also allows the multidimensional fitting, description of correlations between observables and the universal implementation of toy Monte Carlo sampling techniques.
The Roofit is used for fitting and computing fit parameters in my analysis.

Chapter 5

Data analysis

This analysis uses the data taken on LHC in Run 2 during the period E in proton-proton collisions at center of mass energy of 13 TeV. Only $J/\psi \rightarrow \mu^+\mu^-$ and $\psi(2S) \rightarrow \mu^+\mu^-$ decay modes are considered. The J/ψ and $\psi(2S)$ must meet the following criteria. First of all, muons must be oppositely charged. Second, the dimuon transverse momentum p_{T} fulfils conditions $p_{\mathrm{T}} > 8$ GeV and $p_{\mathrm{T}} < 110$ GeV. The first limit is due to the muon trigger and the second is due to the statistics. The pseudorapidity limit is $|\eta| < 2.5$. The total integrated luminosity $L = 437.54\ \mathrm{pb}^{-1}$ for data in period E was calculated using the iLumiCalc tool, where the StandardGRL_All_Good good run list was used[1]. The bin migration correction due to the limited detector resolution was not included.
The data consist of two J/ψ (and $\psi(2S)$) signal components, the prompt and non-prompt signal, and also of their background. The prompt signal are J/ψ ($\psi(2S)$) produced in the proton-proton collision or by the deexcitation of the higher charmonium states. The non-prompt signal are J/ψ ($\psi(2S)$) produced in the secondary reaction, mostly the B-hadron decays. In order to identify the non-prompt J/ψ, the pseudo-proper lifetime as a discrimination variable is used. It is defined as

$$\tau = \frac{L_{xy} m_{PDG}^{J/\psi}}{p_{\mathrm{T}}^{J/\psi}}, \tag{5.1}$$

where L_{xy} is the distance of the J/ψ vertex from the primary vertex measured in the transverse plane, $m_{PDG}^{J/\psi}$ is the charmonium mass from [1] and $p_{\mathrm{T}}^{J/\psi}$ is the transverse momentum of the particle. This formula is also valid for $\psi(2S)$. Thus, the prompt charmonium has a value of the pseudo-proper lifetime equal to 0, meanwhile the non-prompt charmonium pseudo-proper lifetime is nonzero.

[1] Good run lists (GRL) are lists of all runs and luminosity blocks good for physics analysis defined by the Data Quality (DQ) information.

5.1 The reconstruction and trigger efficiency

Prior to the main analysis, the number of J/ψ and $\psi(2S)$ in each event must be scaled by the weight w, defined as

$$w^{-1} = \mathcal{E}_{reco} \cdot \mathcal{E}_{trig}, \tag{5.2}$$

where $\mathcal{E}_{reco}$ is the muon offline reconstruction efficiency and $\mathcal{E}_{trig}$ is the trigger efficiency. For the J/ψ and $\psi(2S)$ reconstruction efficiency $\mathcal{E}_{reco}$, the single muon reconstruction efficiencies $\mathcal{E}^{\pm}_{\mu}\left(p^{+}_{\mathrm{T}}, q \times \eta^{\pm}\right)$ as a function of p_{T} and $q \times \eta(\mu)$ (q is a charge of the muon) are used. Then, the J/ψ and $\psi(2S)$ reconstruction efficiency is calculated as

$$\mathcal{E}_{reco} = \mathcal{E}^{+}_{\mu}\left(p^{+}_{\mathrm{T}}, q \times \eta^{+}\right) \cdot \mathcal{E}^{-}_{\mu}\left(p^{-}_{\mathrm{T}}, q \times \eta^{-}\right). \tag{5.3}$$

The single muon reconstruction map can be seen in Figure 5.1, where is the significant efficiency decrease in the region where $\eta \approx 0$. This is due to the cabling of muon detectors. Analogically to the reconstruction, the trigger efficiency is calculated as a multiple of the single muon trigger efficiencies $\mathcal{E}^{\pm}_{RoI}\left(p^{+}_{\mathrm{T}}, q \times \eta^{\pm}\right)$ and the correction factor $c_{\mu\mu}\left(\Delta R, |y^{\mu\mu}|\right)$, thus

$$\mathcal{E}_{trig} = \mathcal{E}^{+}_{RoI}\left(p^{+}_{\mathrm{T}}, q \times \eta^{+}\right) \cdot \mathcal{E}^{-}_{RoI}\left(p^{-}_{\mathrm{T}}, q \times \eta^{-}\right) \cdot c_{\mu\mu}\left(\Delta R, |y^{\mu\mu}|\right). \tag{5.4}$$

The factor $c_{\mu\mu}$ provides a correction on opposite muon charge and vertexing requirement. The single muon trigger efficiency map is shown in Figure 5.1. Both maps were provided by the ATLAS B-physics group.

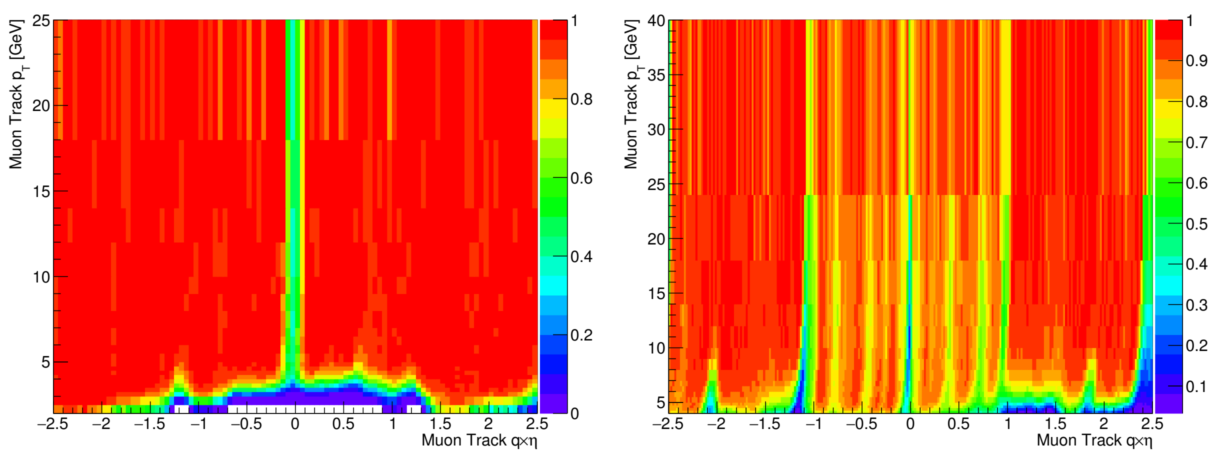

Figure 5.1: The single muon reconstruction efficiency map (left) and trigger efficiency map (right) of HLT_2mu4_bJpsimumu for 13 TeV data as a function of the p_{T} and multiple of muon charge and pseudorapidity.

5.2 The mass-lifetime fit model

The weighted data were separated into p_{T} and $|y|$ bins and then fitted in each bin with a two-dimensional mass-lifetime fit, which consists of prompt and non-prompt signal and three background function.

The prompt J/ψ and $\psi(2S)$ mass component was modelled with a Gaussian, as well as the non-prompt mass component. The means of both Gaussians were fixed to the PDG values of J/ψ and $\psi(2S)$ masses to reduce the additional degree of freedom of the probability function. For the pseudo-proper lifetime prompt component, a Dirac function convolved with a resolution function was used, meanwhile one-sided exponential convolved with identical resolution function was used for the lifetime non-prompt component.

As mentioned earlier, the background is composed of three components, one prompt and two non-prompt. The mass prompt background was modeled with a linear function and the time prompt background is described by a Dirac function convolved with the resolution function. The non-prompt background consists of two components. In the first component, mass is represented by an exponential function and time is modeled by a single-sided exponential convolved with the resolution function. In the second component, mass is again described by an exponential function and time is represented by a double-sided exponential convolved with the resolution function.

Summing up all five components described above and also in the Table , the final probability distribution function is

$$PDF\left(m,\tau\right)=\sum_{i=1}^{5} f_i\cdot P_i\left(m,\tau\right)\otimes R\left(\tau\right), \tag{5.5}$$

where f_i is the normalisation factor, $P_i\left(m,\tau\right)$ is a two-dimensional probability function and $R\left(\tau\right)$ is a lifetime resolution model function.

The J/ψ mass and time distributions and fits with respect to the p_{T} and $|y|$ bins are shown in Figures A.1-A.16 in Appendix A. Similarly, the $\psi(2S)$ mass and time distributions and fits are shown in Figures B.1-B.16. The results are presented only with a statistical uncertainty, the systematic uncertainties are not calculated yet because the main analysis is still in progress.

Source	Type	Invariant mass	Pseudo-proper lifetime
Signal	prompt	$G(m)$	$\delta(\tau)$
	non-prompt	$G(m)$	$Exp_3(\tau)$
Background	prompt	$P^{(1)}(m)$	$\delta(\tau)$
	non-prompt	$Exp_1(m)$	$Exp_4(\tau)$
	non-prompt	$Exp_2(m)$	$Exp_5(\lvert\tau\rvert)$

Table 5.1: Components of the mass-lifetime fit model. G represents Gaussian, δ is a Dirac delta function, $P^{(1)}$ is linear function and Exp represents exponential function.

5.3 The non-prompt J/ψ and $\psi(2S)$ fraction

Using the information obtained from the mass lifetime fits, the non-prompt fraction f_b^{ψ} can be plotted. It is defined as the ratio of the number of non-prompt charmonia to the total amount produced:

$$f_b^{\psi} = \frac{pp \to b + X \to \psi + X'}{pp \xrightarrow{\text{inclusive}} \psi + X'} = \frac{N_{\psi}^{NP}}{N_{\psi}^{NP} + N_{\psi}^{P}}, \tag{5.6}$$

where N_{ψ}^{NP} denotes the number of non-prompt charmonia and N_{ψ}^{P} denotes the prompt part of the signal.

The J/ψ and $\psi(2S)$ non-prompt fractions for four rapidity ranges are plotted in Figure 5.2 and 5.3. The non-prompt fraction increases with the J/ψ ($\psi(2S)$) transverse momentum p_{T} except of the $\psi(2S)$ rapidity bin $0.75 < |y| < 2.0$, where the mass-lifetime fit does not converge well. The rapidity influence on the non-prompt fraction is insignificant. For the $\psi(2S)$, the rapidity bins $2.0 < |y| < 2.5$ were omitted due to the small statistical sample, as well as the bins $40 < p_{\mathrm{T}} < 60$ and $60 < p_{\mathrm{T}} < 110$ with the rapidity $1.5 < |y| < 2.0$.

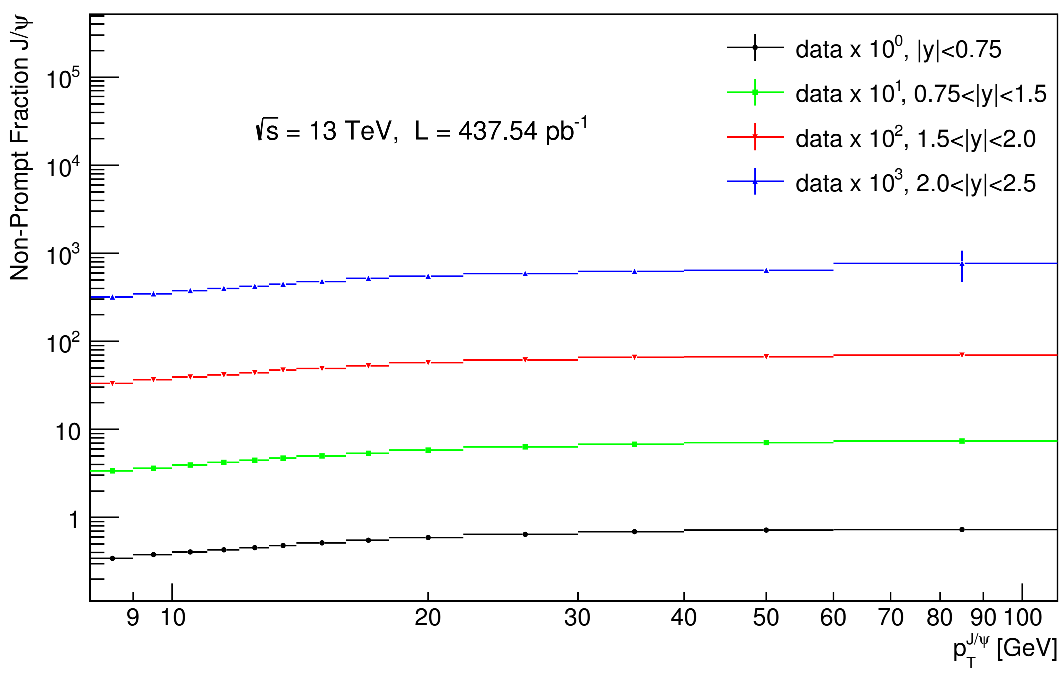

Figure 5.2: The J/ψ non-prompt fraction for $\sqrt{s} = 13$ TeV as function of p_{T} for different rapidity bins.

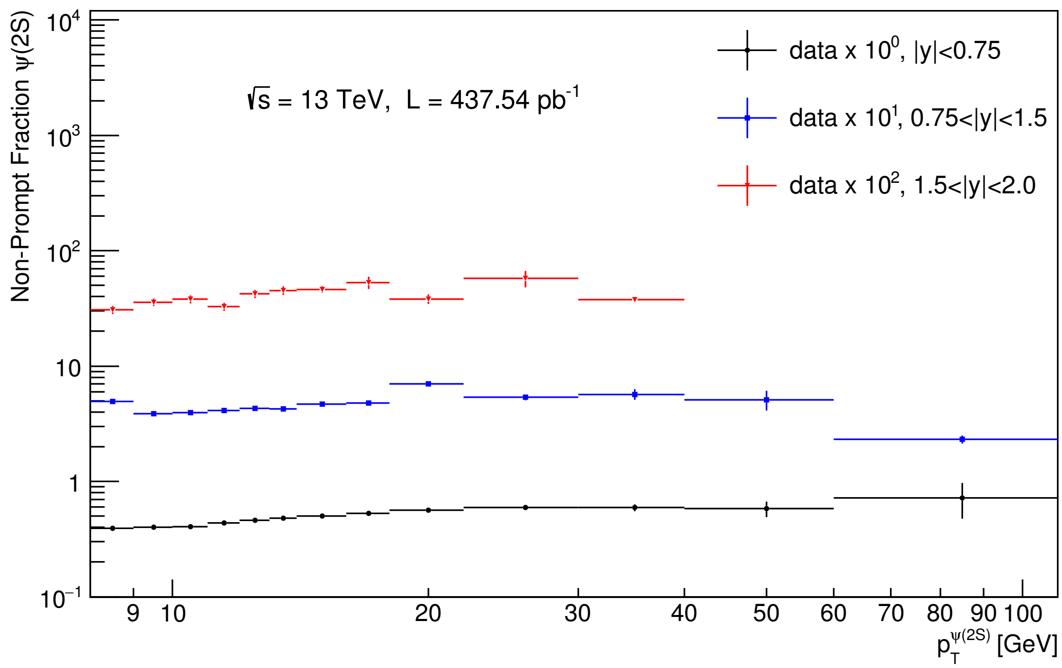

Figure 5.3: The $\psi(2S)$ non-prompt fraction for $\sqrt{s} = 13$ TeV as function of p_{T} for different rapidity bins.

5.4 Inclusive $J/\psi \to \mu^+\mu^-$ and $\psi(2S) \to \mu^+\mu^-$ differential production cross-section

The differential dimuon cross-section in each bin for the sum of prompt and non-prompt J/ψ (and $\psi(2S)$) is defined as

$$\frac{\mathrm{d}^2\sigma}{\mathrm{d}p_{\mathrm{T}}\mathrm{d}y}\mathcal{B}r\left(\psi \to \mu^+\mu^-\right) = \frac{N}{\Delta p_{\mathrm{T}}\Delta y L}, \tag{5.7}$$

where Δp_{T} and Δy are the transverse momentum and rapidity width, L is the integrated luminosity of the data sample and N is the number of prompt and non-prompt J/ψ or $\psi(2S)$ mesons for each p_{T} and y bin, corrected for trigger and reconstruction efficiencies.Assuming the ATLAS detector is symmetrical, the width Δy includes particles with both positive and negative rapidity. Figures 5.4 and 5.5 show the J/ψ and $\psi(2S)$ differential cross-sections. The cross-section seems to be flat for low p_{T} (8-10 GeV) and decreases in dependence to p_{T}, the rapidity does not affect the data.

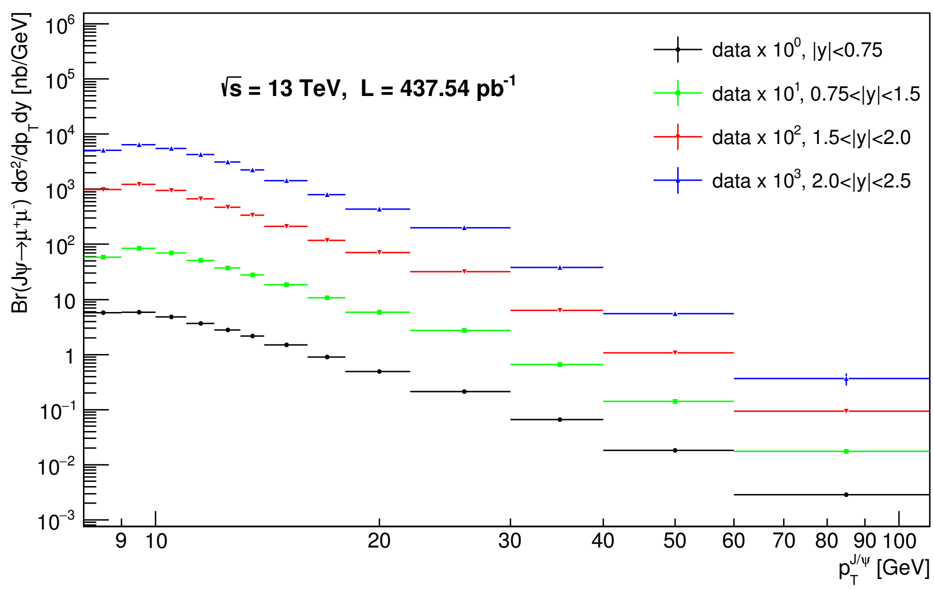

Figure 5.4: The J/ψ differential production cross-section for $\sqrt{s} = 13$ TeV data as a function of J/ψ p_{T} in several bins of rapidity y.

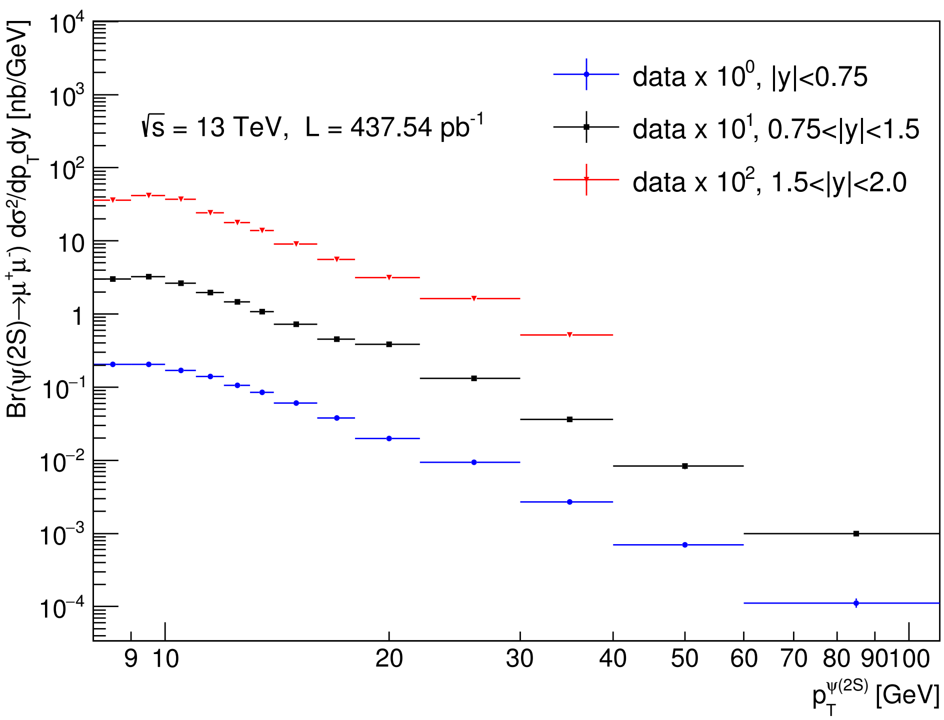

Figure 5.5: The $\psi(2S)$ differential production cross-section for $\sqrt{s} = 13$ TeV data as a function of $\psi(2S)$ p_{T} in several bins of rapidity y.

5.5 $\psi(2S)$ to J/ψ differential production cross-section ratio

The ratio of $\psi(2S)$ to J/ψ inclusive production cross-section is defined as

$$R = \frac{N_{\psi(2S)}}{N_{J/\psi}}, \tag{5.8}$$

where $N_{\psi(2S)}$ is the number of inclusive $\psi(2S)$ in the dimuon decay and $N_{J/\psi}$ is the number of inclusive J/ψ in the dimuon decay. The efficiency corrections are eliminated in this formula, therefore the results are precise.
The result in Figure 5.6 seems to be constant with no dependence on the p_{T} and y except for the bins with rapidity $1.5 < |y| < 2.0$, where the ratio increases with the transverse momentum, but this can be caused by the small statistical sample.

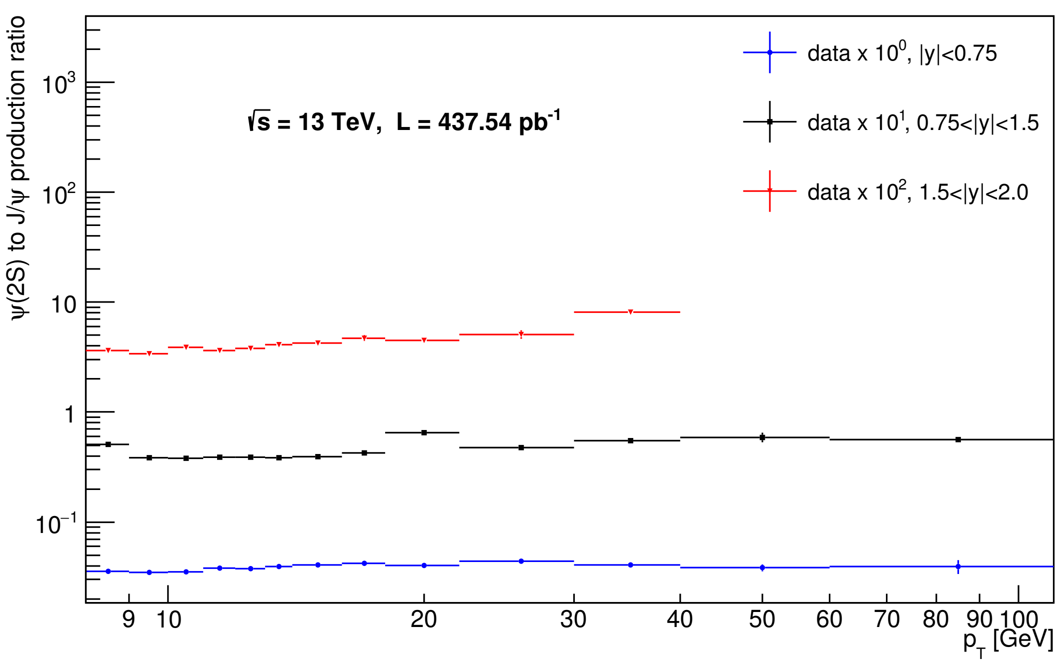

Figure 5.6: The $\psi(2S)$ to J/ψ production ratio for 13 TeV as function of p_{T} in several rapidity y bins.

Conclusion

This thesis was devoted to the study of the J/ψ and $\psi(2S)$ mesons. The main motivation was to measure the inclusive production cross-section, the ratio of their cross-sections and the non-prompt production fraction of both mesons. For this purpose, the data from the proton-proton collisions with the center-of-mass energy of $\sqrt{s} = 13$ TeV were used. These data were recorded by the ATLAS experiment at the LHC in the period E with the integrated luminosity $L = 437.54$ pb^{-1}.

The summit of this thesis is the data flow and the description of my own analysis. The non-prompt J/ψ production fraction in the $\mu^+\mu^-$ channel was measured in the transverse momentum range $8 < p_\mathrm{T} < 110$ GeV and the rapidity range $|y| < 2.5$. This fraction rises for the increasing transverse momentum and has no dependence on the rapidity. Due to the small statistical sample, the non-prompt $\psi(2S)$ production fraction in the $\mu^+\mu^-$ channel was measured only in the rapidity range $|y| < 2.0$ and the fraction has the same trend as the non-prompt J/ψ fraction. The J/ψ and $\psi(2S)$ inclusive production cross-sections decrease with the transverse momenta and are independent on the rapidity, except for one $\psi(2S)$ bin.

To improve this results, more data, especially the $\psi(2S)$ events, should be analysed. Also, the acceptance correction has to be made, together with the calculation of the systematic error.

Appendix A

J/ψ invariant mass and pseudo-proper lifetime distributions with fits

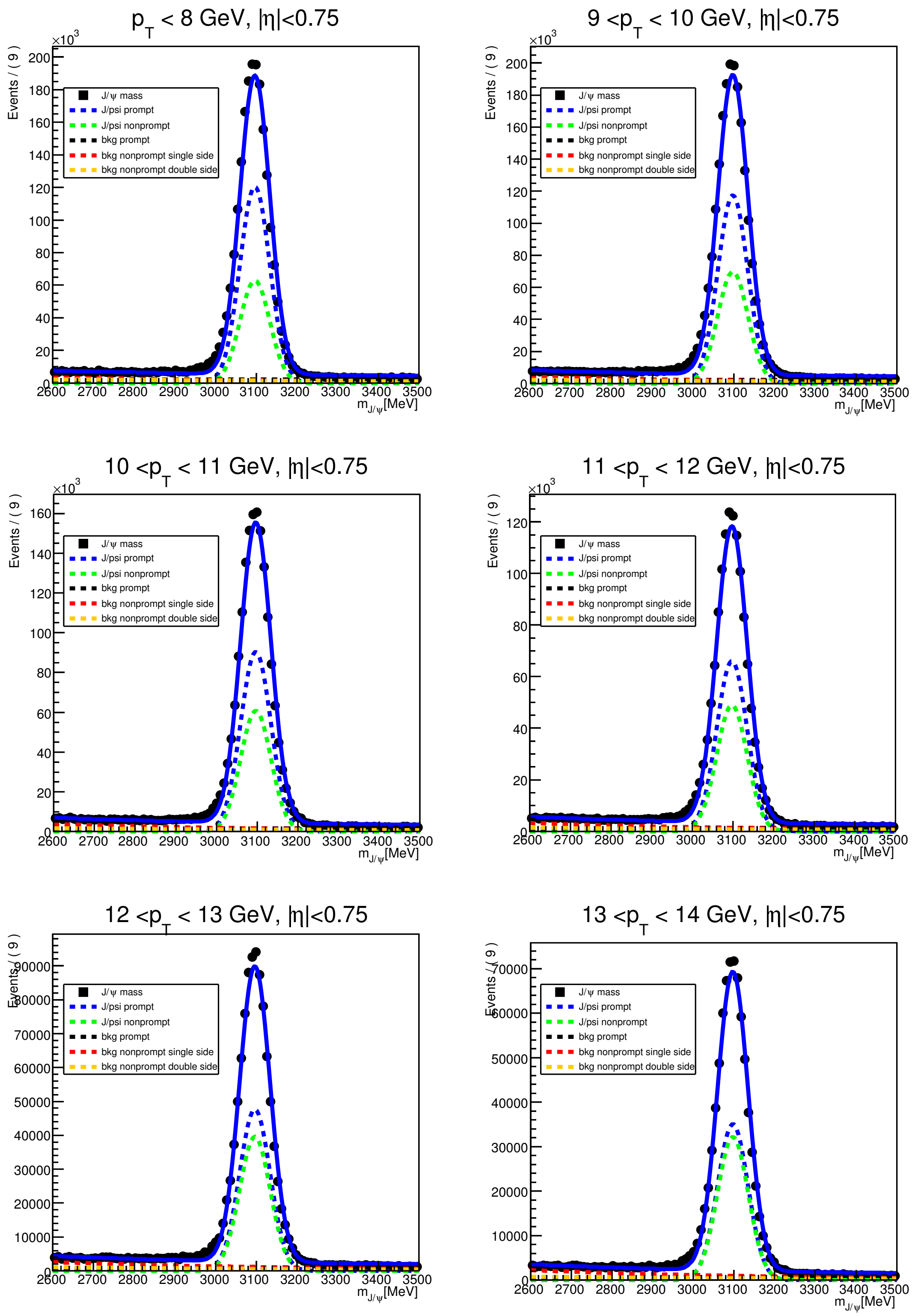

Figure A.1: Invariant mass distribution of weighted J/ψ in rapidity $|y| < 0.75$ for different transverse momenta p_{T}.

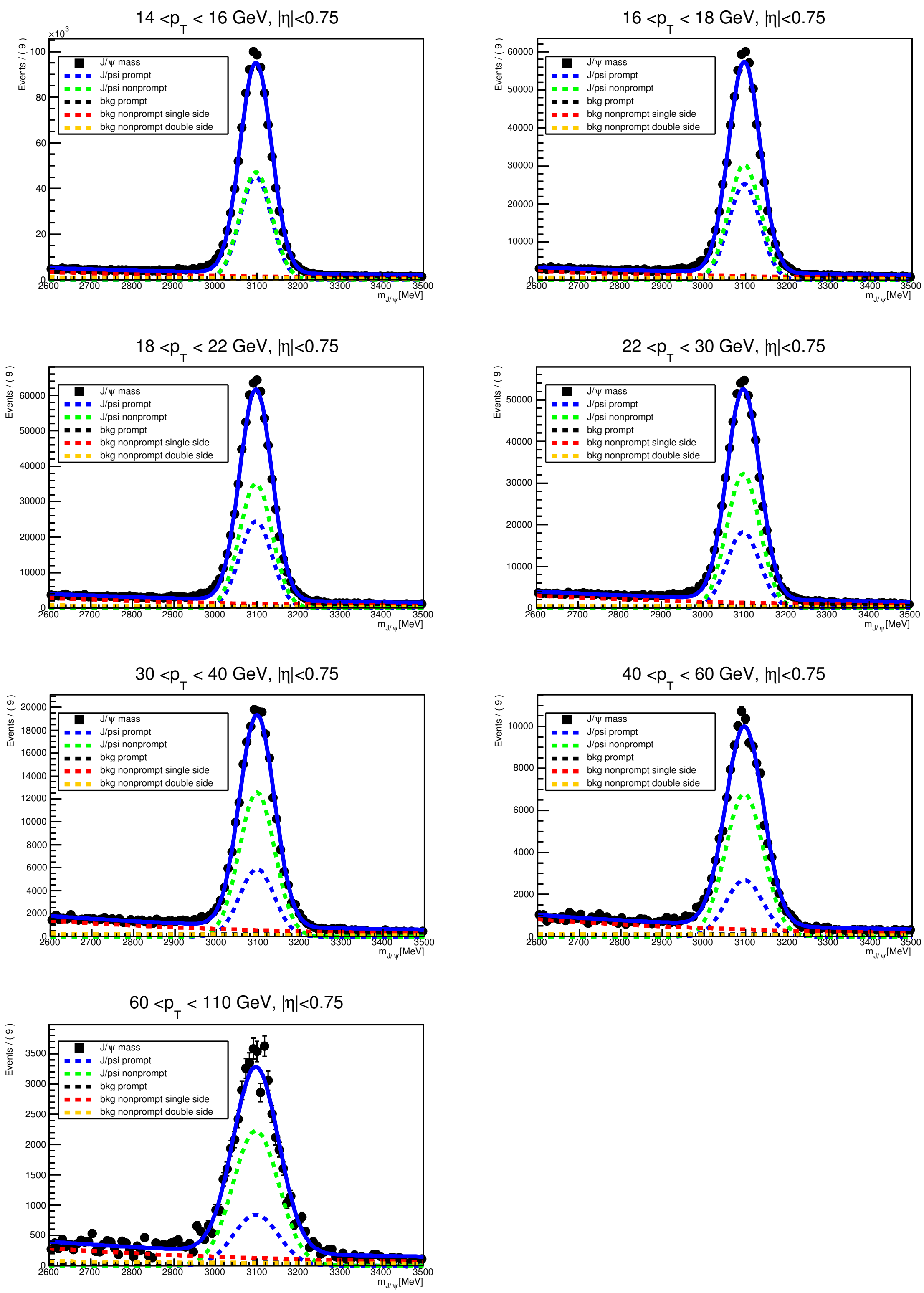

Figure A.2: Invariant mass distribution of weighted J/ψ in rapidity $|y| < 0.75$ for different transverse momenta p_{T}.

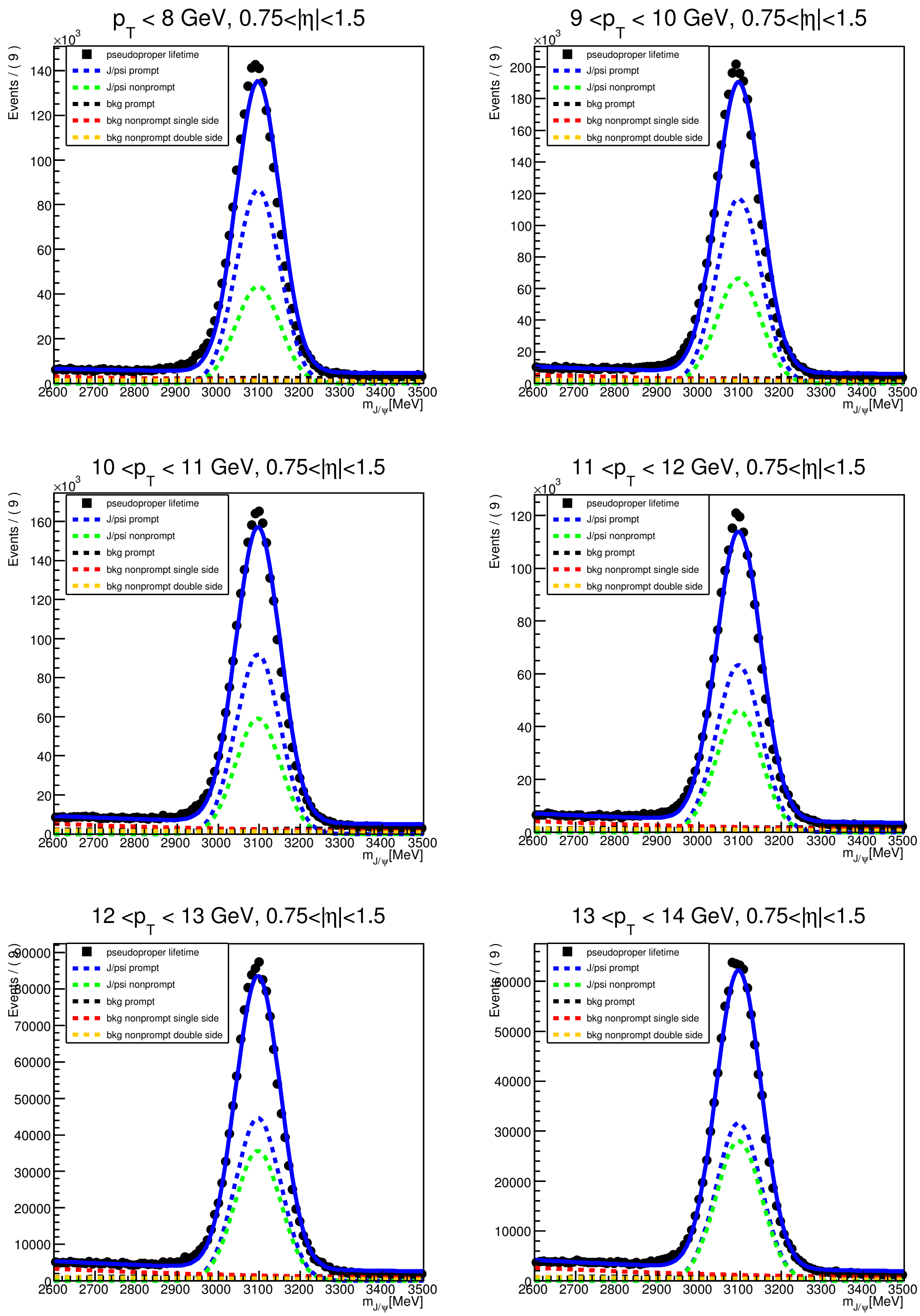

Figure A.3: Invariant mass distribution of weighted J/ψ in rapidity $0.75 < |y| < 1.5$ for different transverse momenta p_{T}.

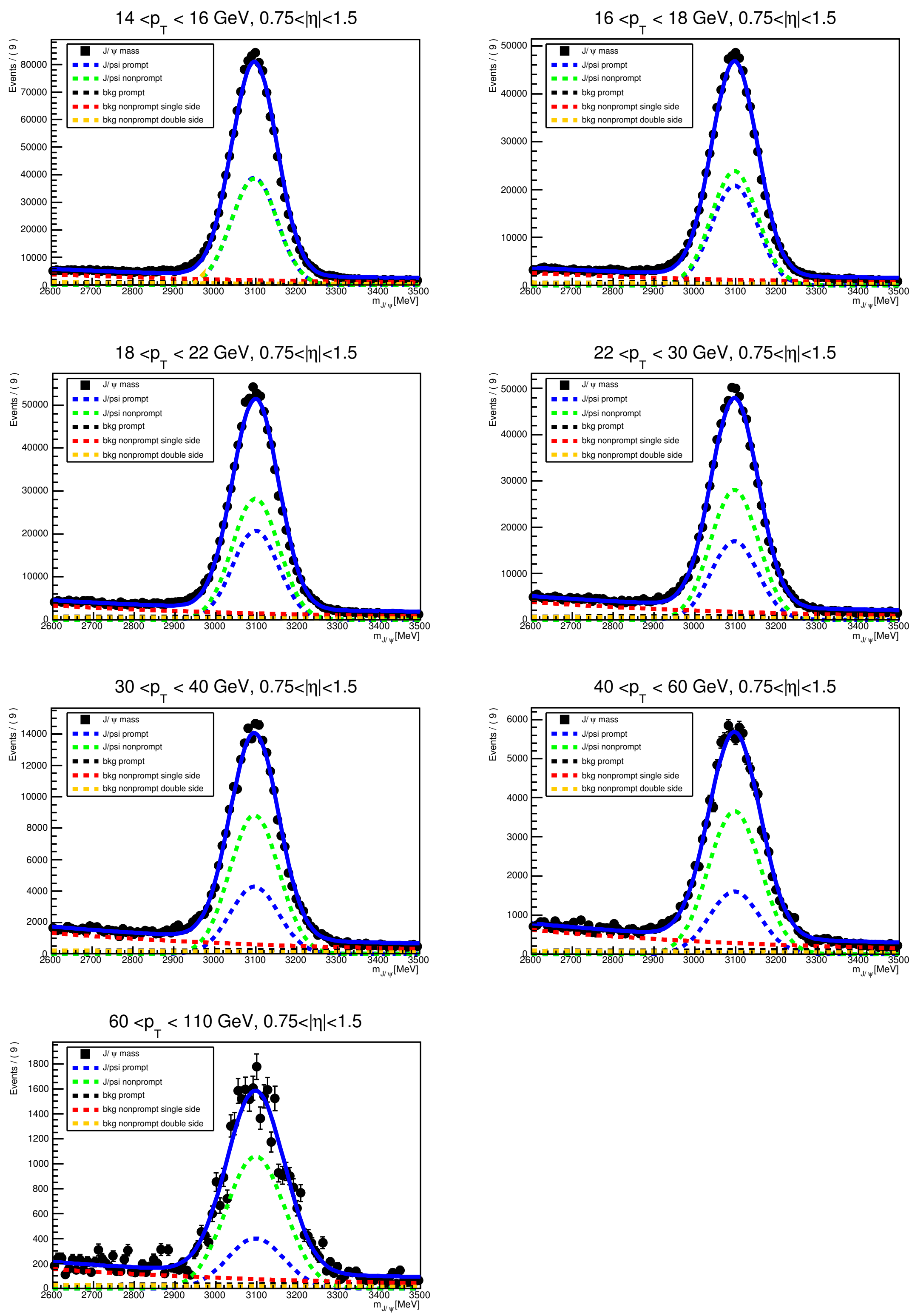

Figure A.4: Invariant mass distribution of weighted J/ψ in rapidity $0.75 < |y| < 1.5$ for different transverse momenta p_{T}.

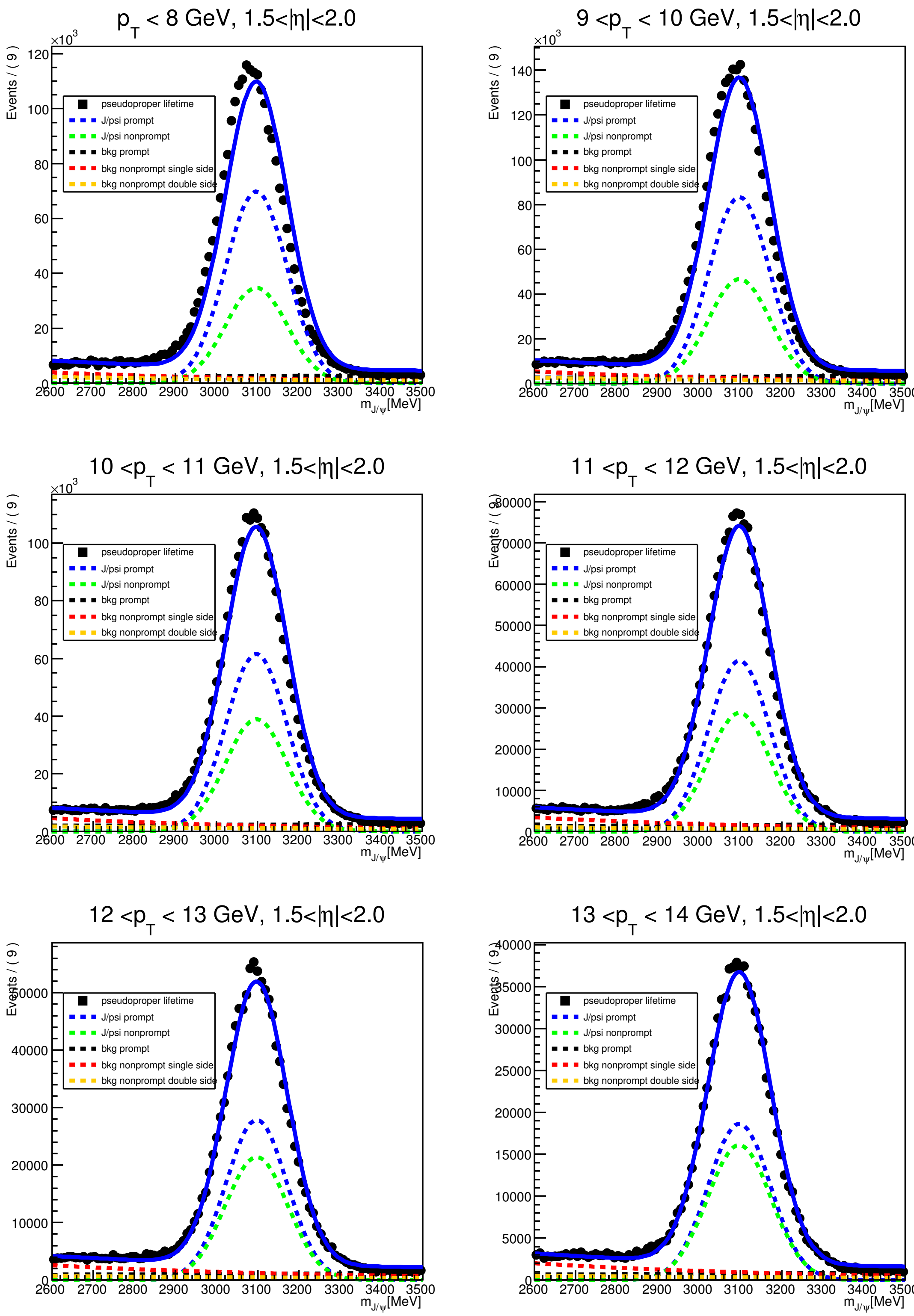

Figure A.5: Invariant mass distribution of weighted J/ψ in rapidity $1.5 < |y| < 2.0$ for different transverse momenta p_{T}.

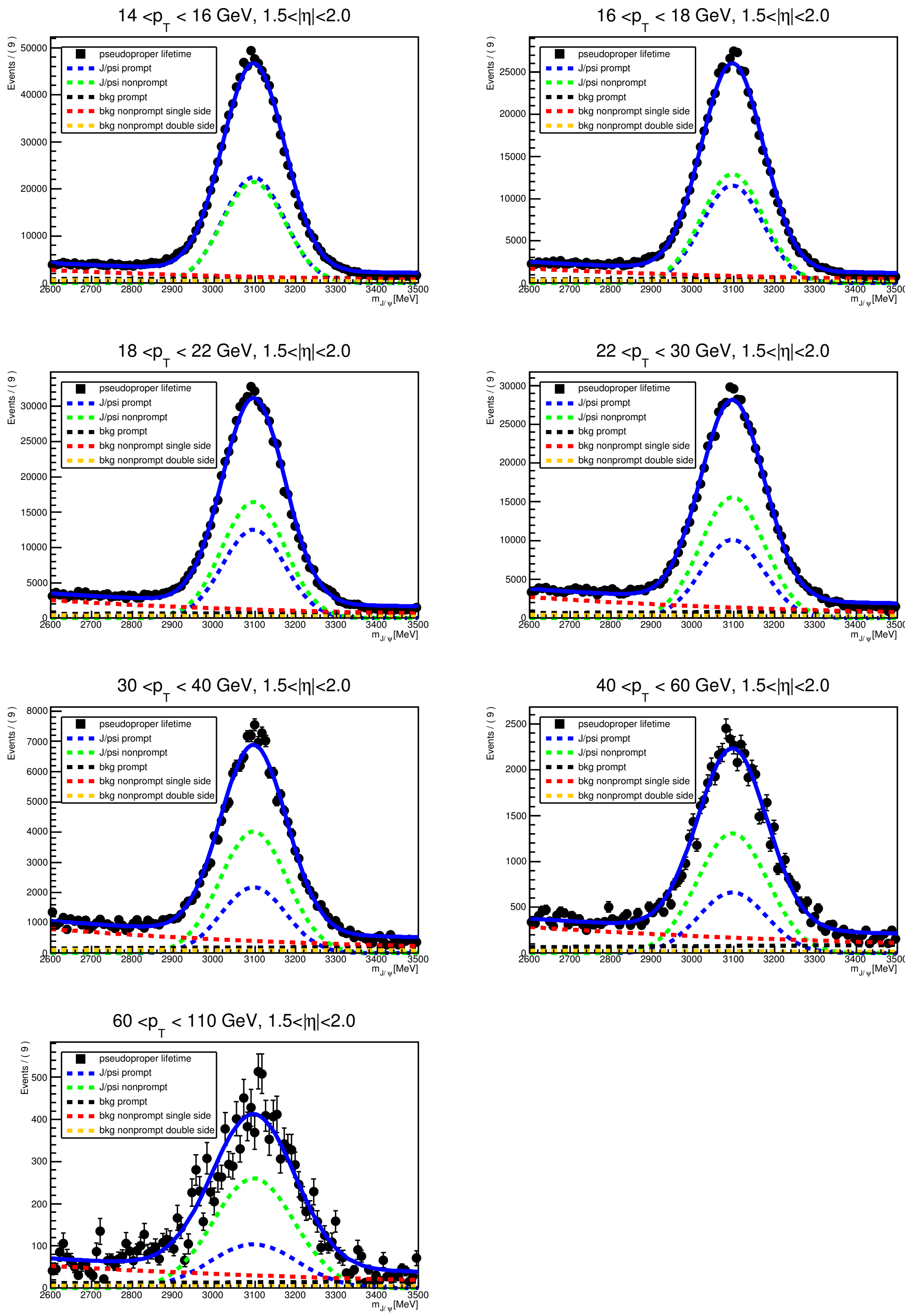

Figure A.6: Invariant mass distribution of weighted J/ψ in rapidity $1.5 < |y| < 2.0$ for different transverse momenta p_{T}.

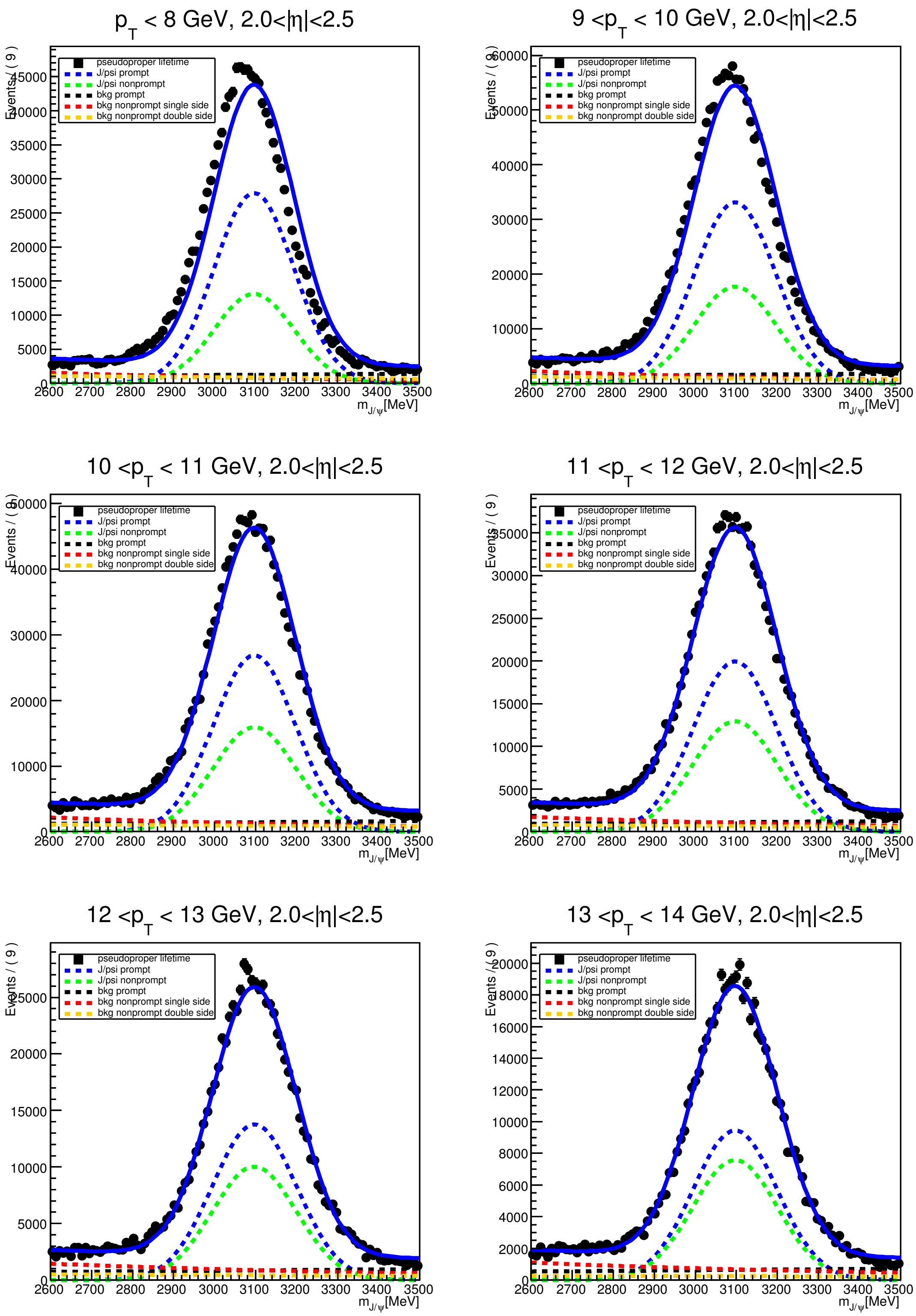

Figure A.7: Invariant mass distribution of weighted J/ψ in rapidity $2.0 < |y| < 2.5$ for different transverse momenta p_{T}.

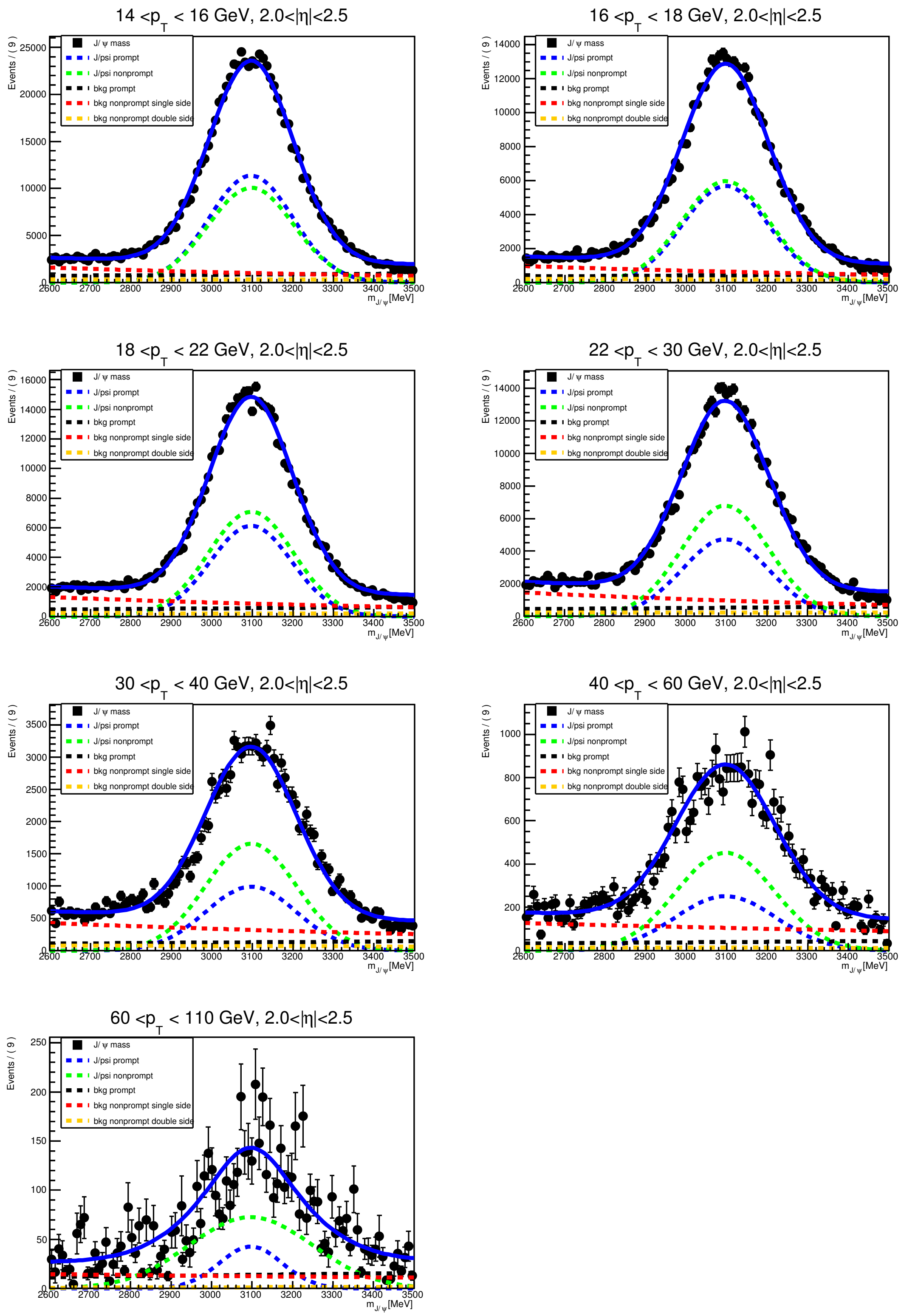

Figure A.8: Invariant mass distribution of weighted J/ψ in rapidity $2.0 < |y| < 2.5$ for different transverse momenta p_{T}.

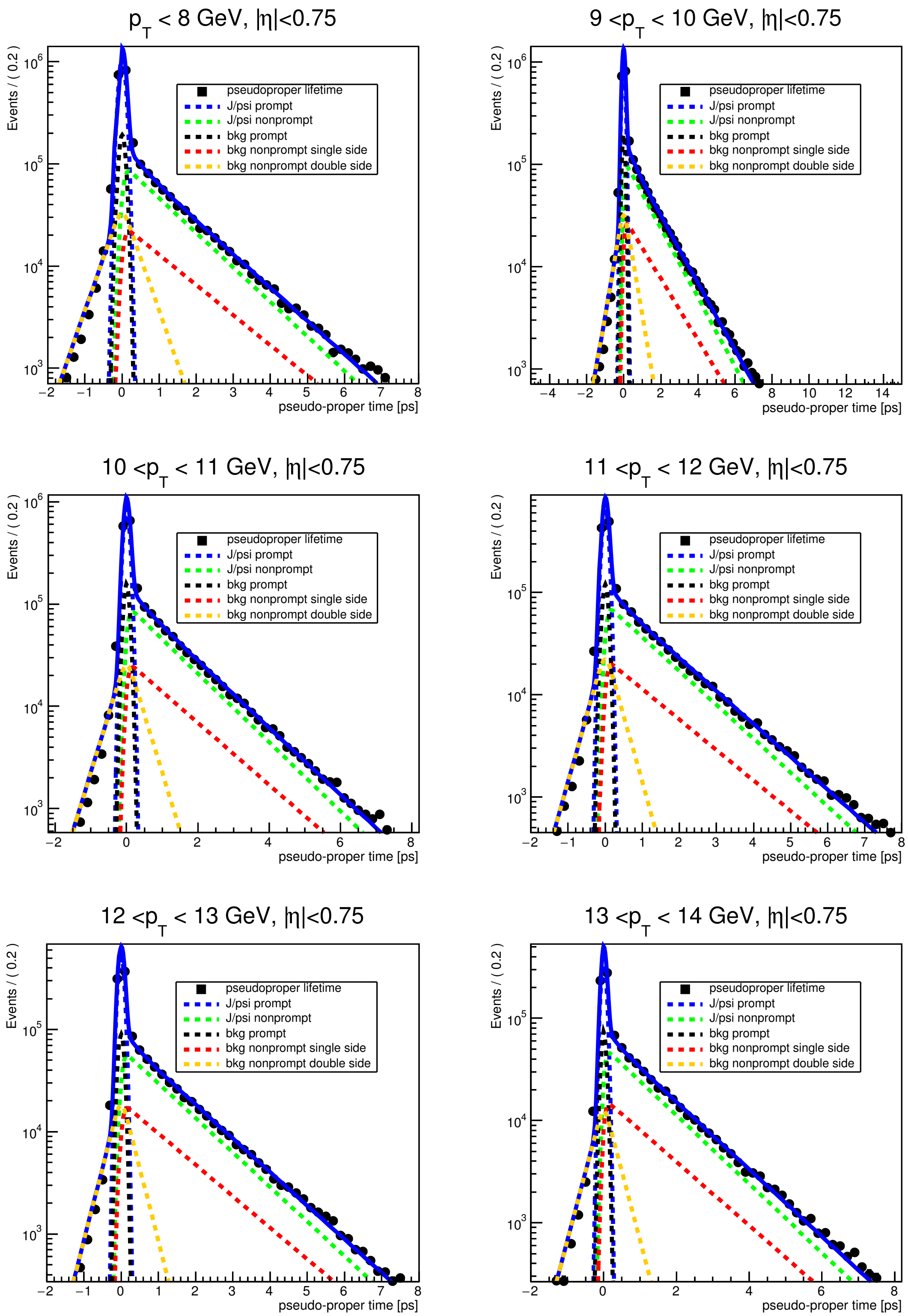

Figure A.9: Pseudo-proper lifetime distribution of weighted J/ψ in rapidity $|y| < 0.75$ for different transverse momenta p_{T}.

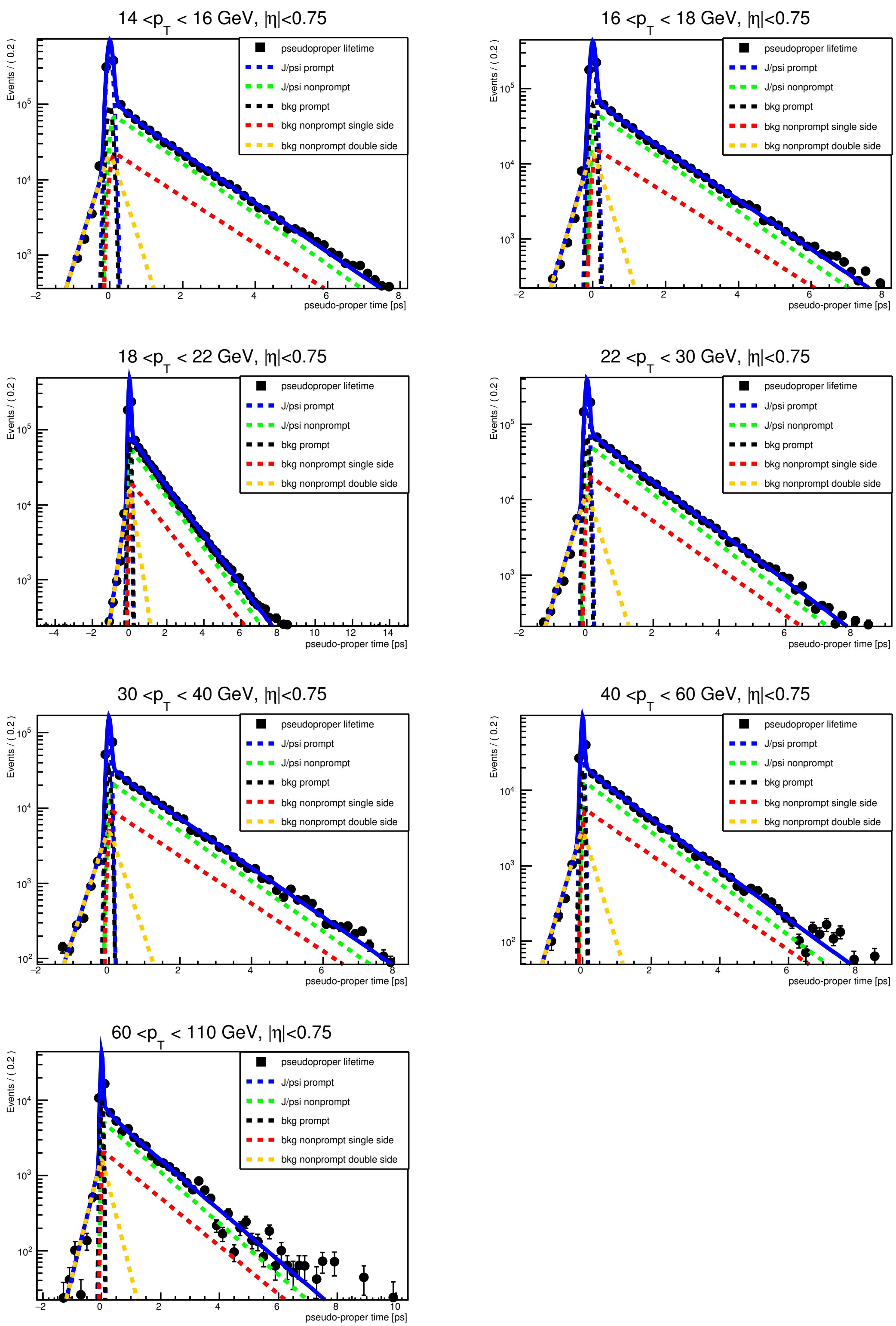

Figure A.10: Pseudo-proper lifetime distribution of weighted J/ψ in rapidity $|y| < 0.75$ for different transverse momenta p_{T}.

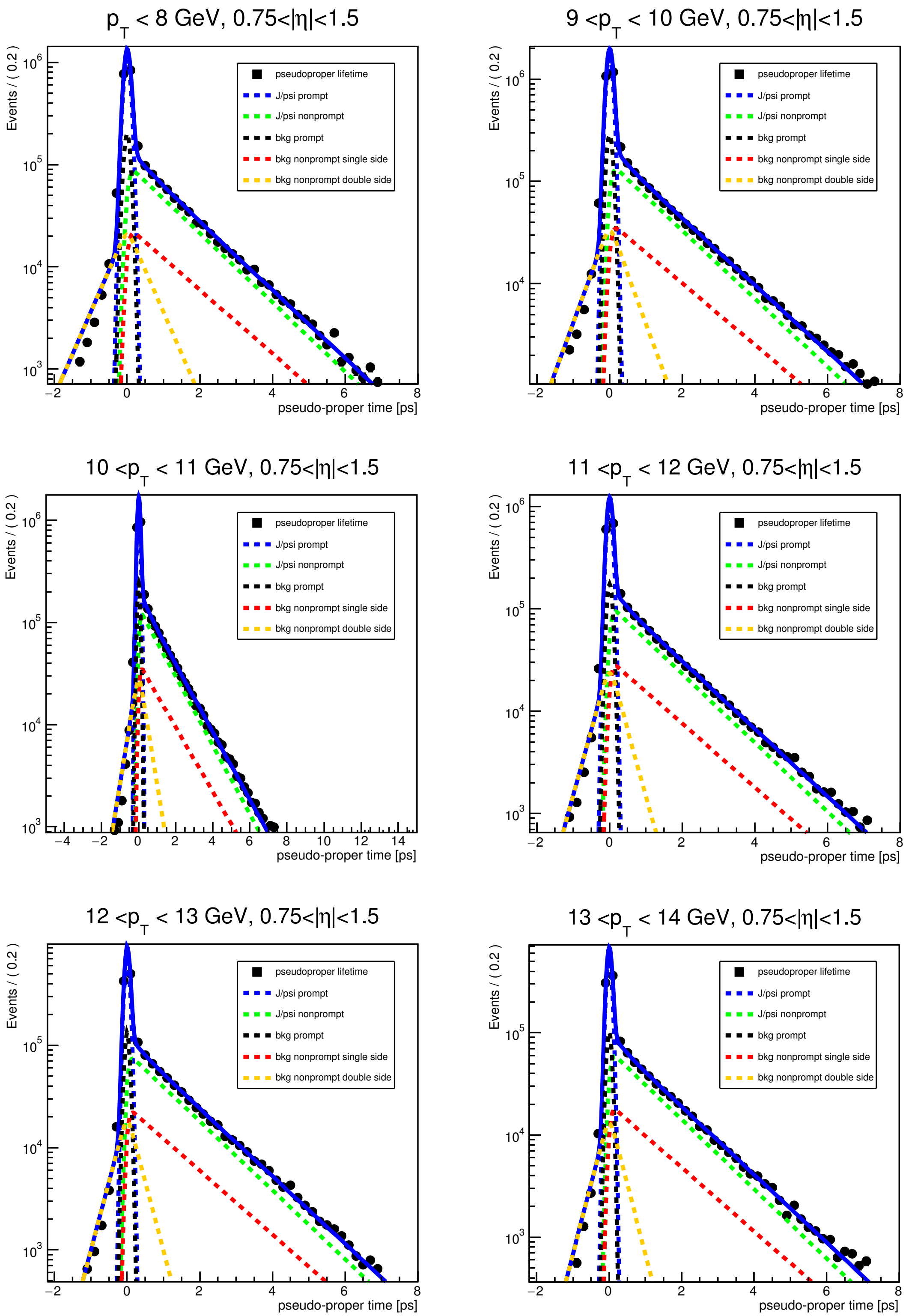

Figure A.11: Pseudo-proper lifetime distribution of weighted J/ψ in rapidity $0.75 < |y| < 1.5$ for different transverse momenta p_{T}.

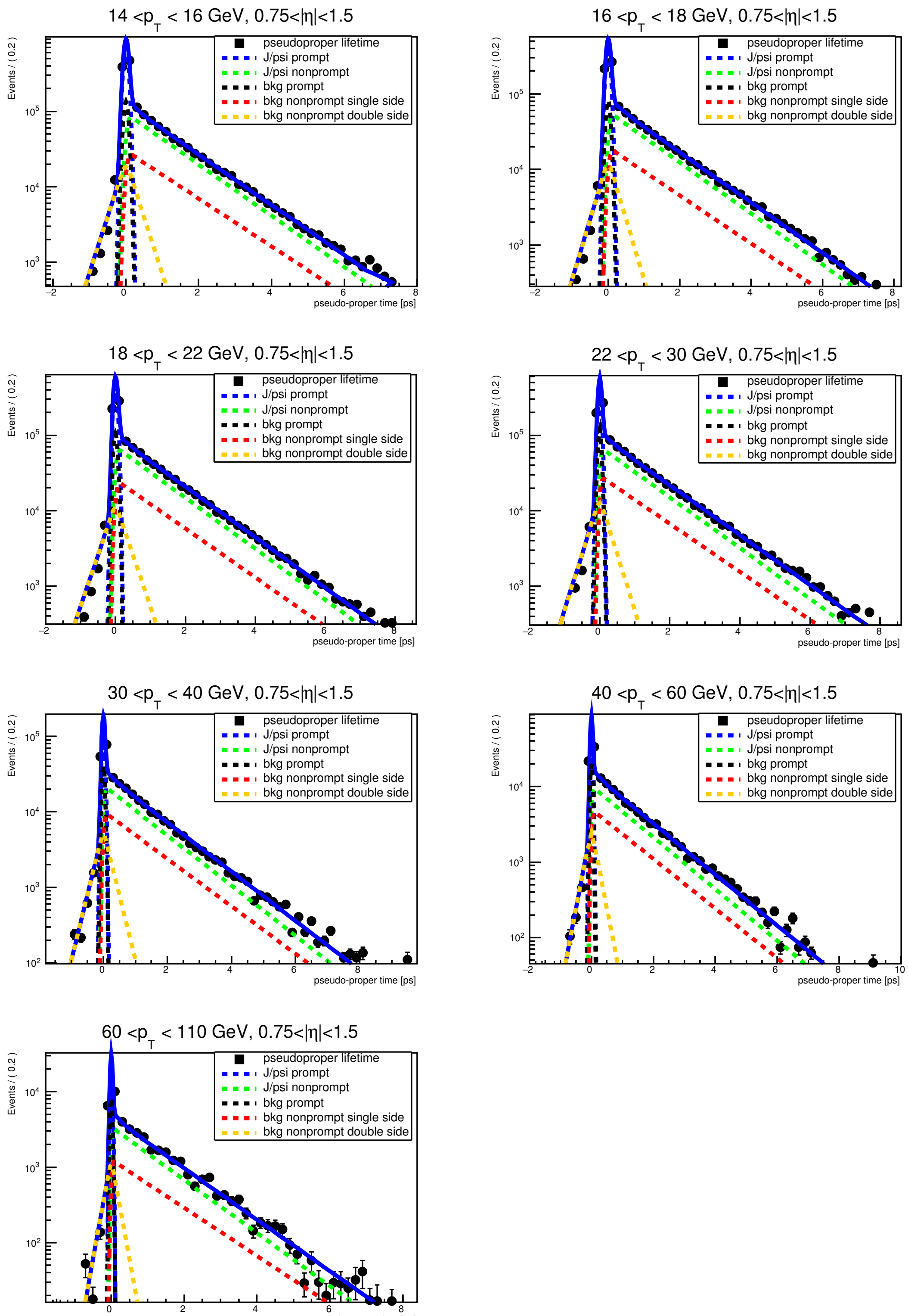

Figure A.12: Pseudo-proper lifetime distribution of weighted J/ψ in rapidity $0.75 < |y| < 1.5$ for different transverse momenta p_{T}.

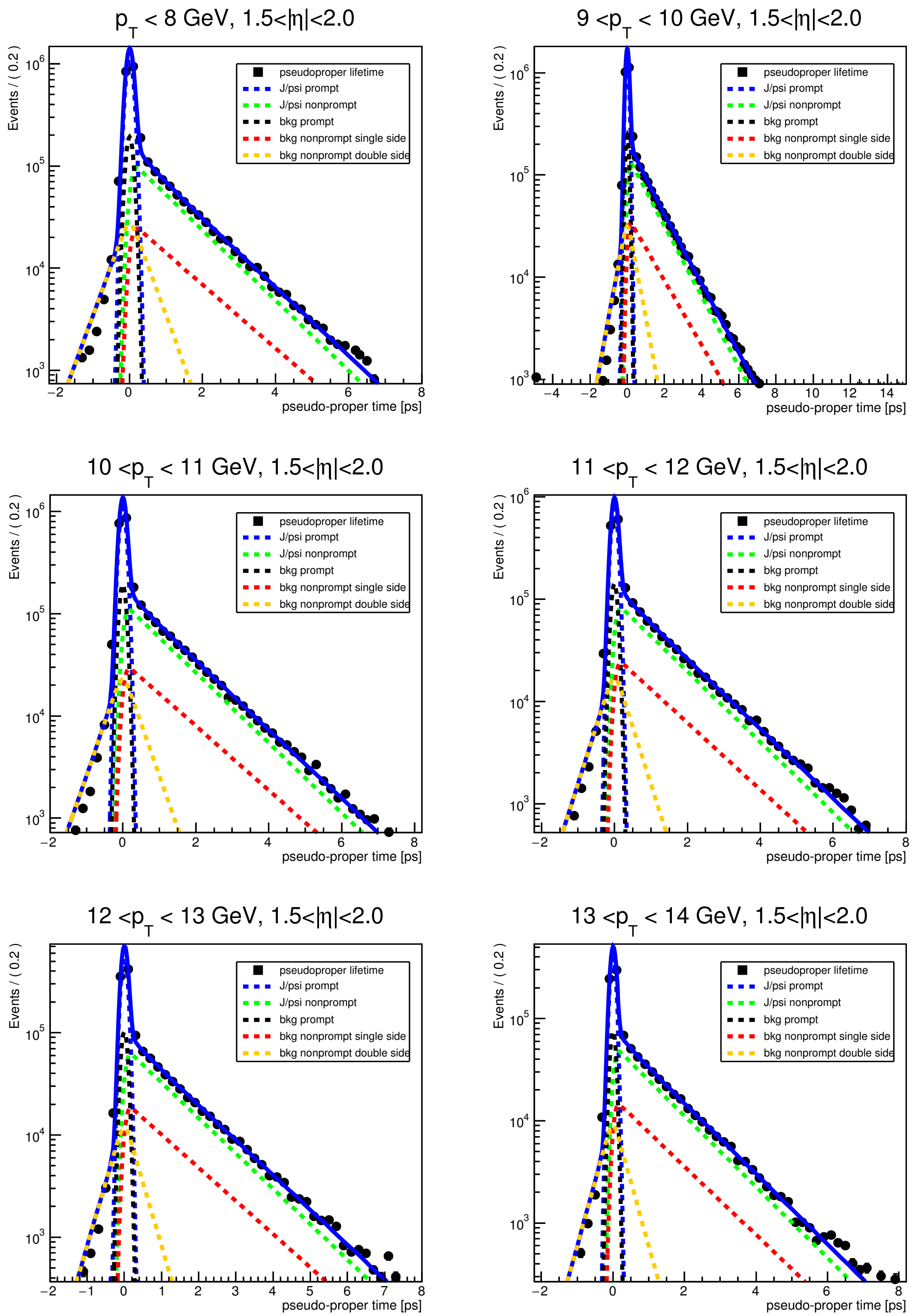

Figure A.13: Pseudo-proper lifetime distribution of weighted J/ψ in rapidity $1.5 < |y| < 2.0$ for different transverse momenta p_{T}.

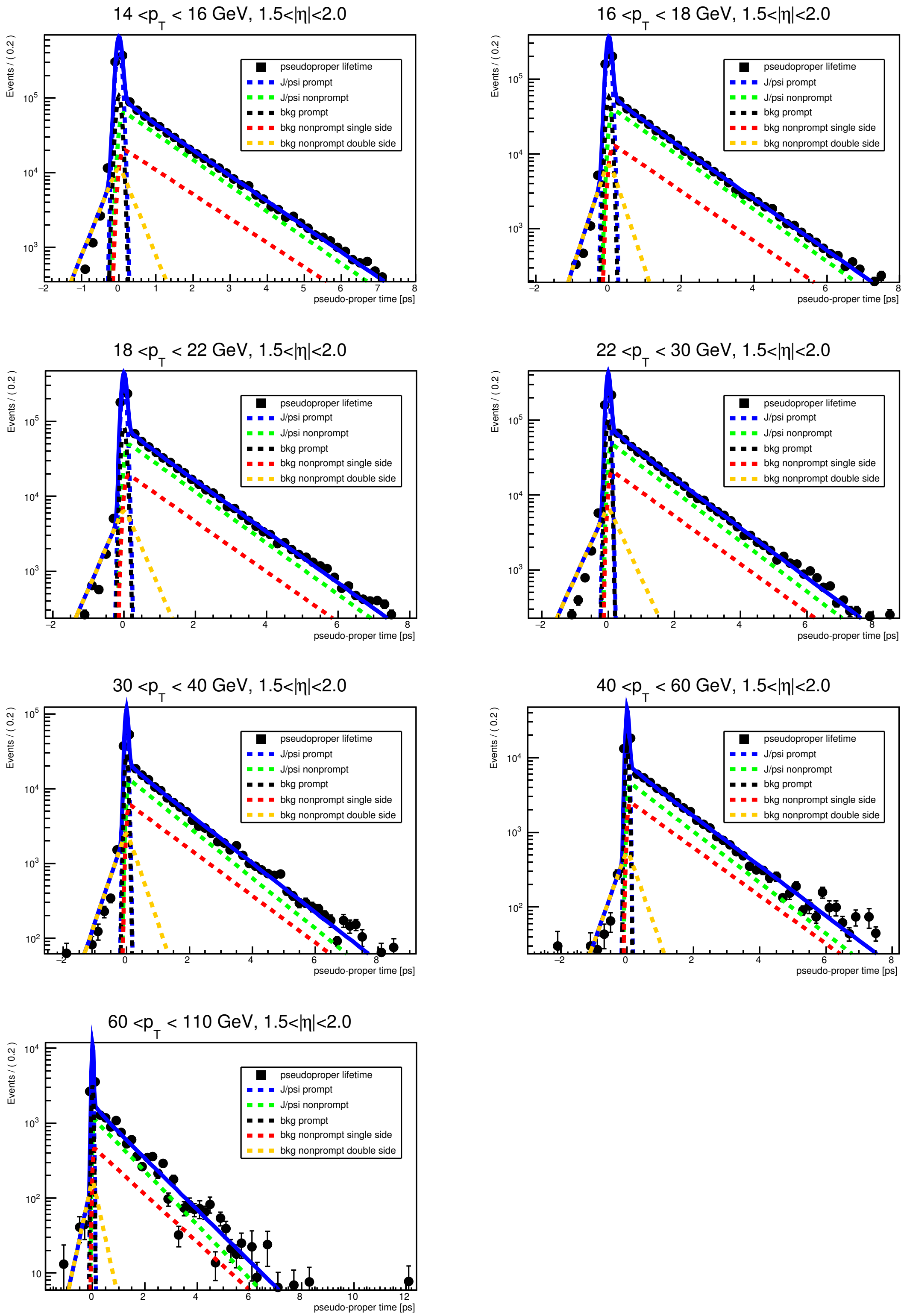

Figure A.14: Pseudo-proper lifetime distribution of weighted J/ψ in rapidity $1.5 < |y| < 2.0$ for different transverse momenta p_{T}.

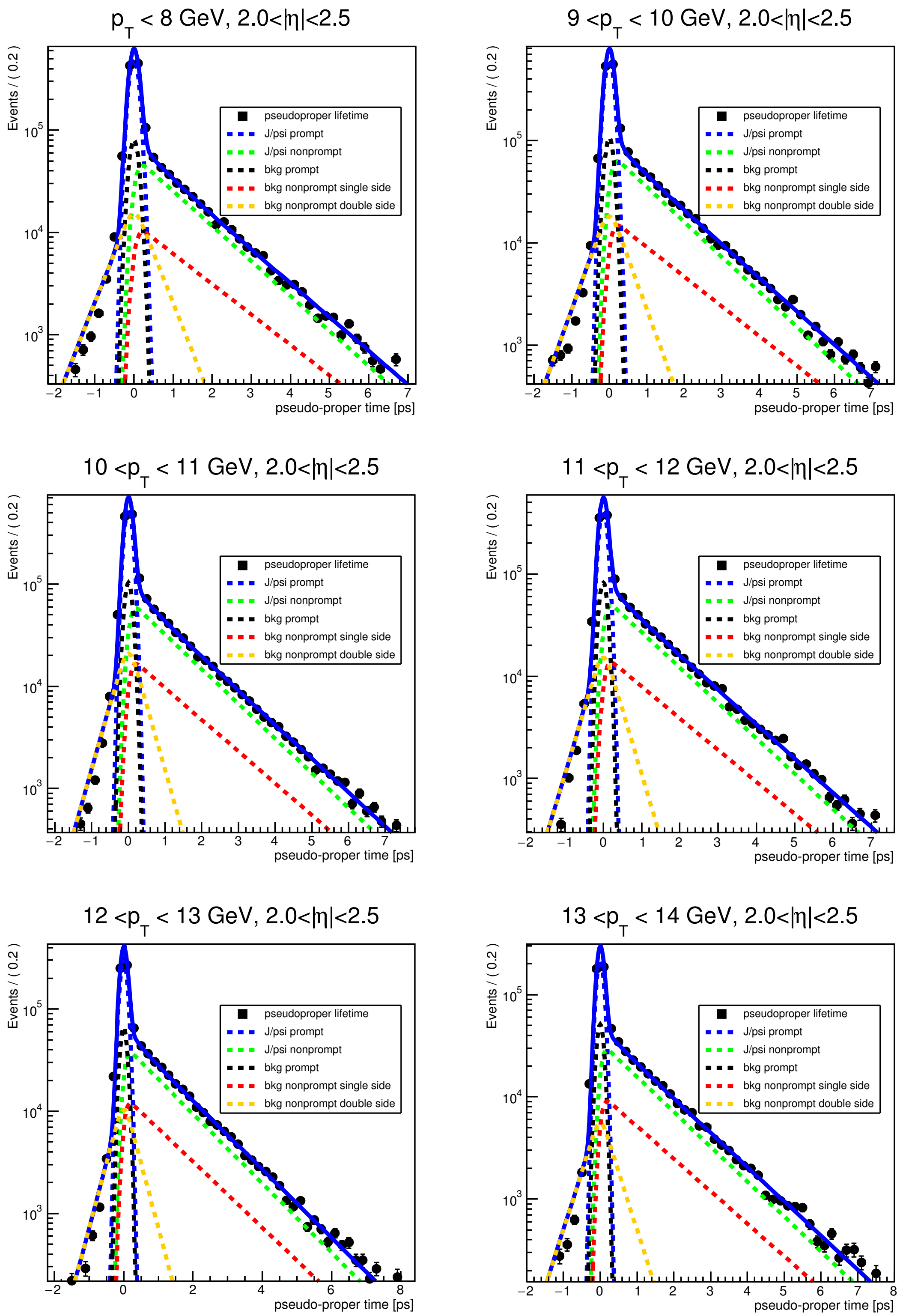

Figure A.15: Pseudo-proper lifetime distribution of weighted J/ψ in rapidity $2.0 < |y| < 2.5$ for different transverse momenta p_{T}.

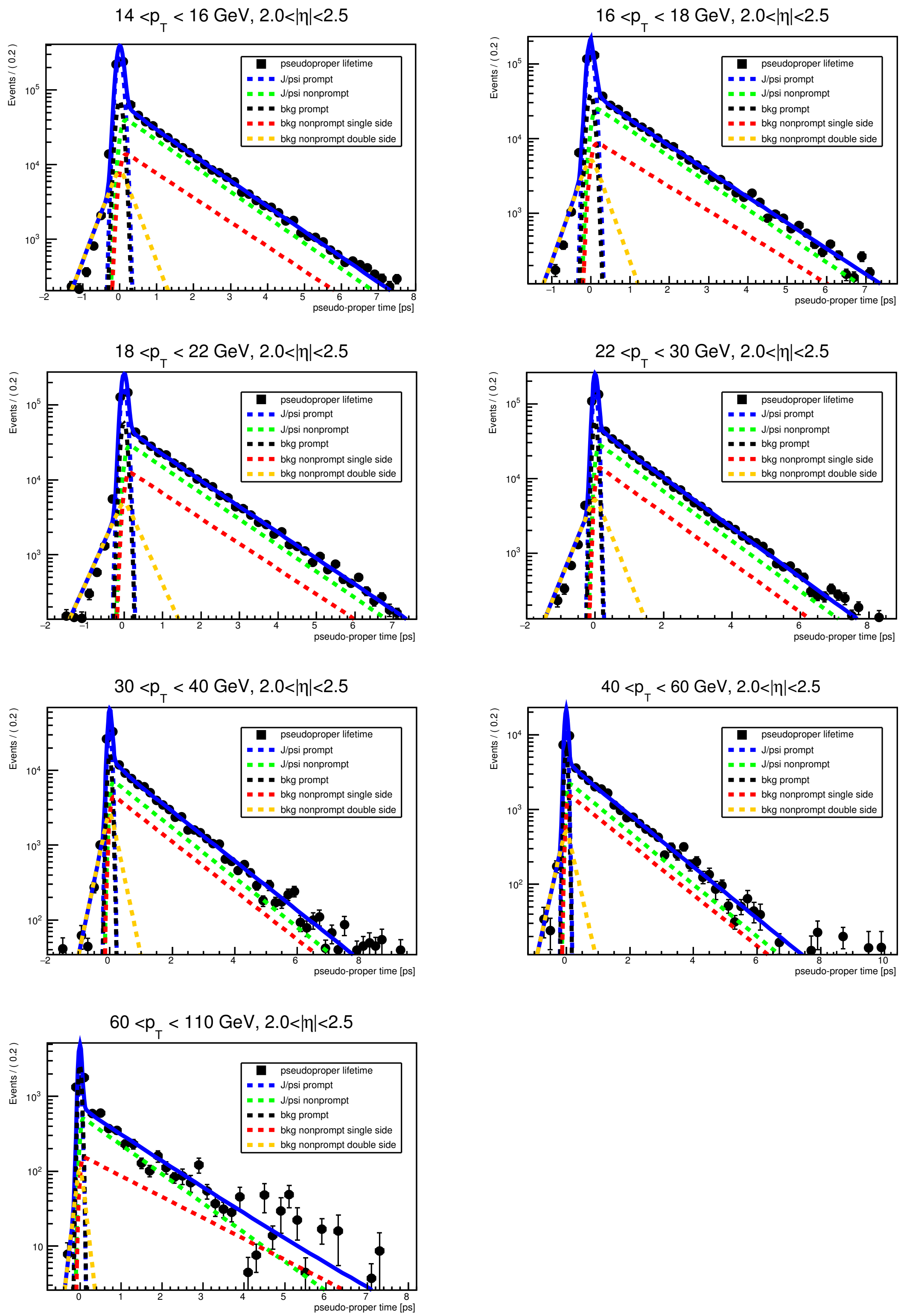

Figure A.16: Pseudo-proper lifetime distribution of weighted J/ψ in rapidity $2.0 < |y| < 2.5$ for different transverse momenta p_{T}.

Appendix B

$\psi(2S)$ invariant mass and pseudo-proper lifetime distributions with fits

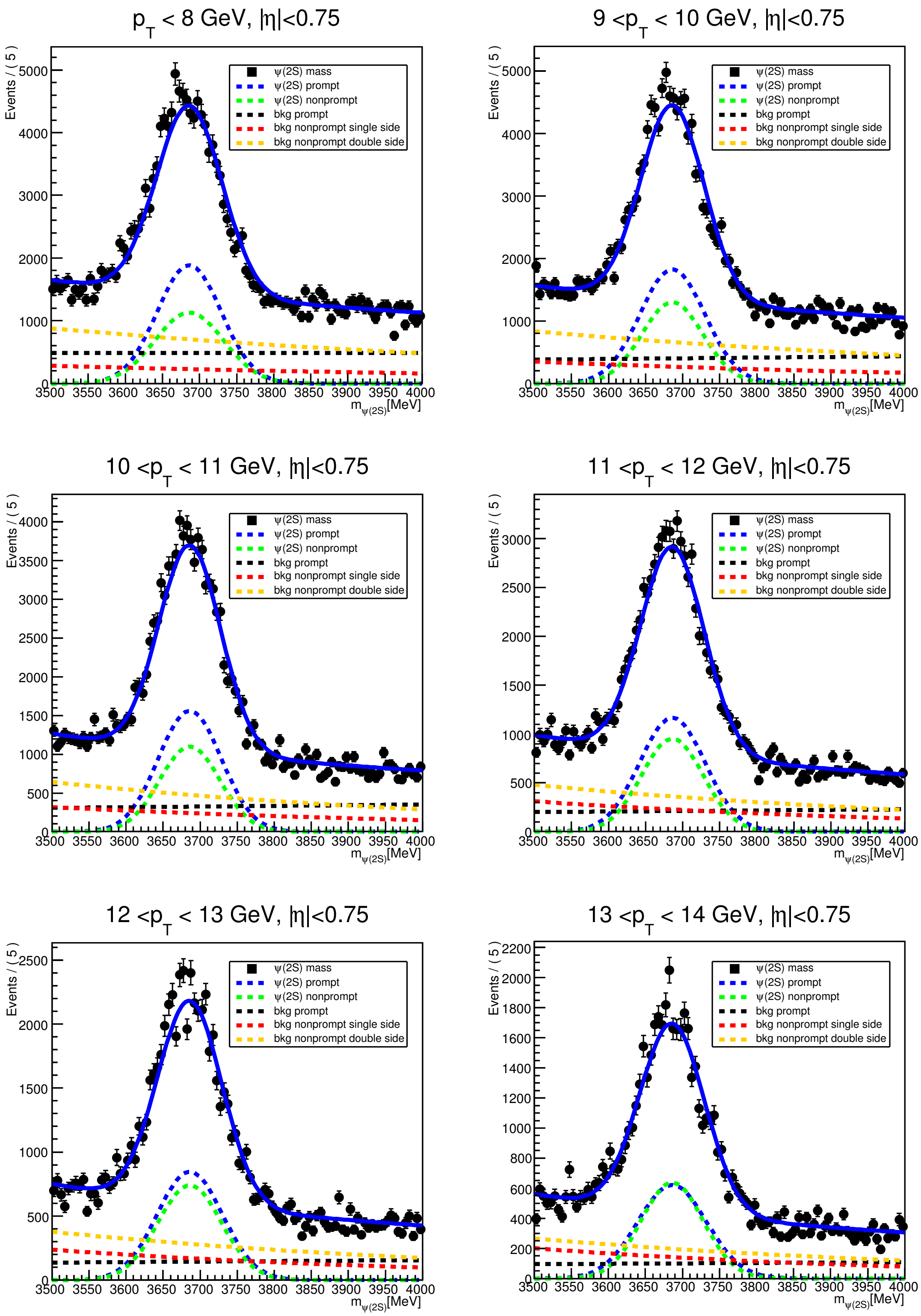

Figure B.1: Invariant mass distribution of weighted $\psi(2S)$ in rapidity $|y| < 0.75$ for different transverse momenta p_{T}.

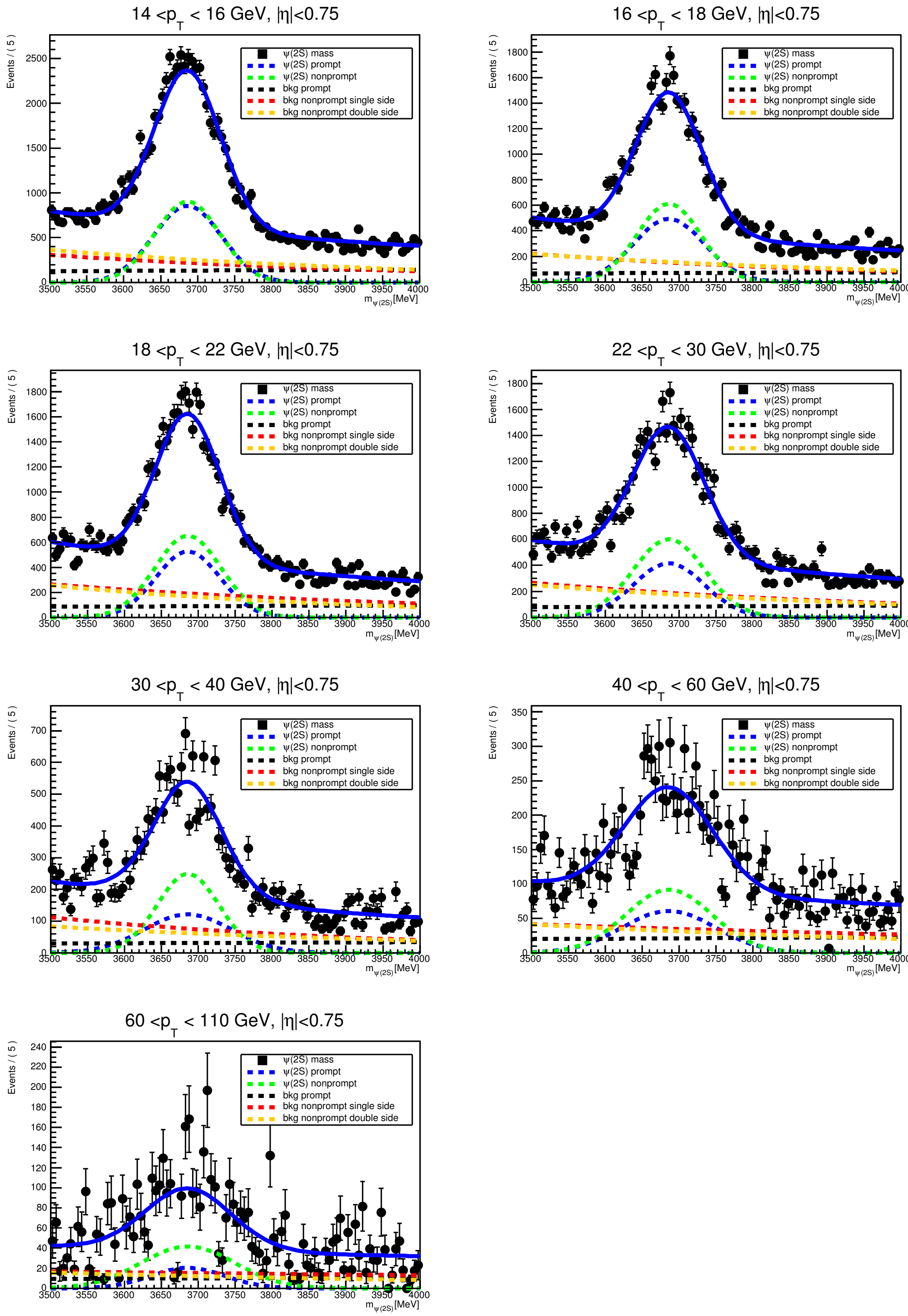

Figure B.2: Invariant mass distribution of weighted $\psi(2S)$ in rapidity $|y| < 0.75$ for different transverse momenta p_{T}.

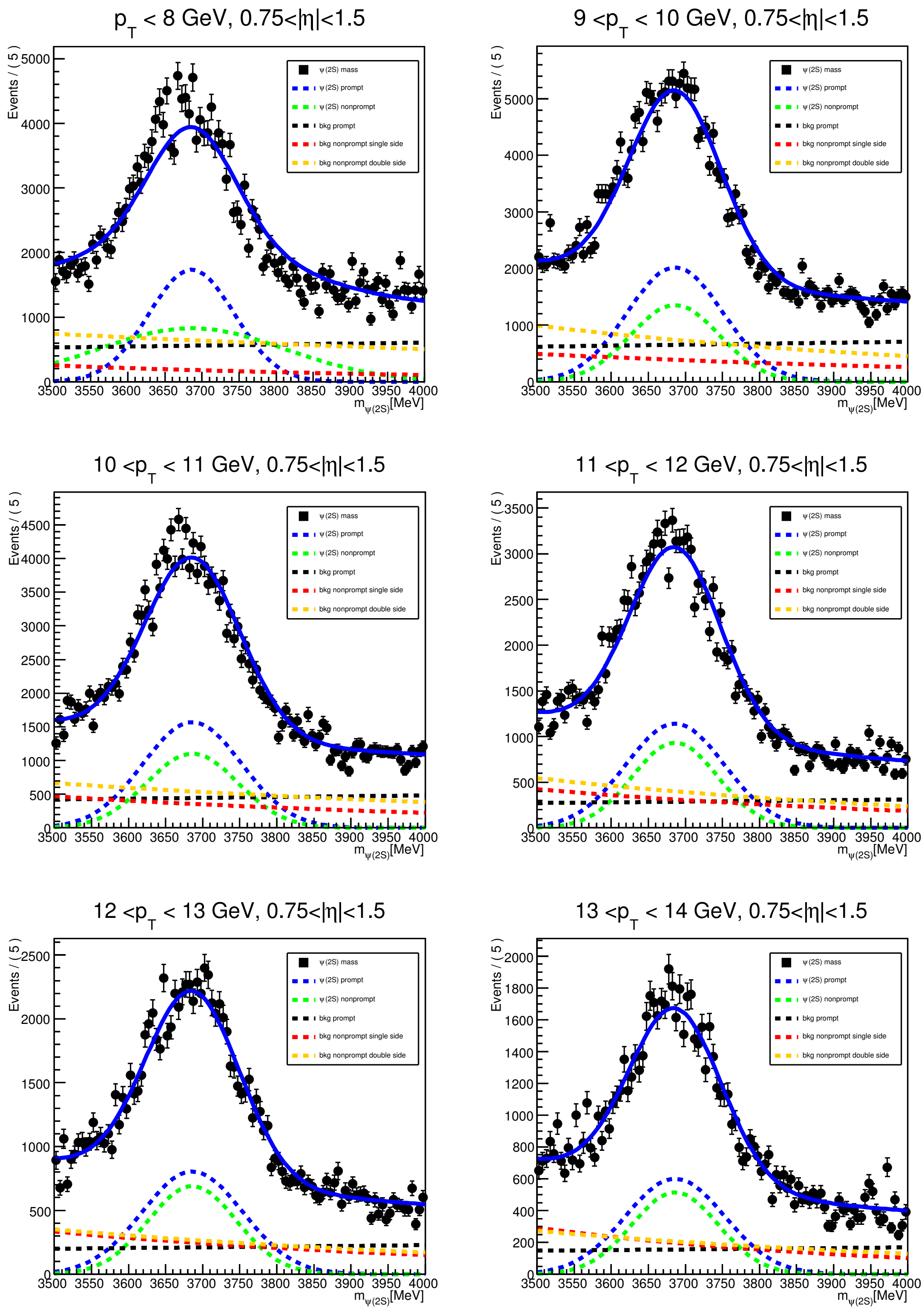

Figure B.3: Invariant mass distribution of weighted $\psi(2S)$ in rapidity $0.75 < |y| < 1.5$ for different transverse momenta p_{T}.

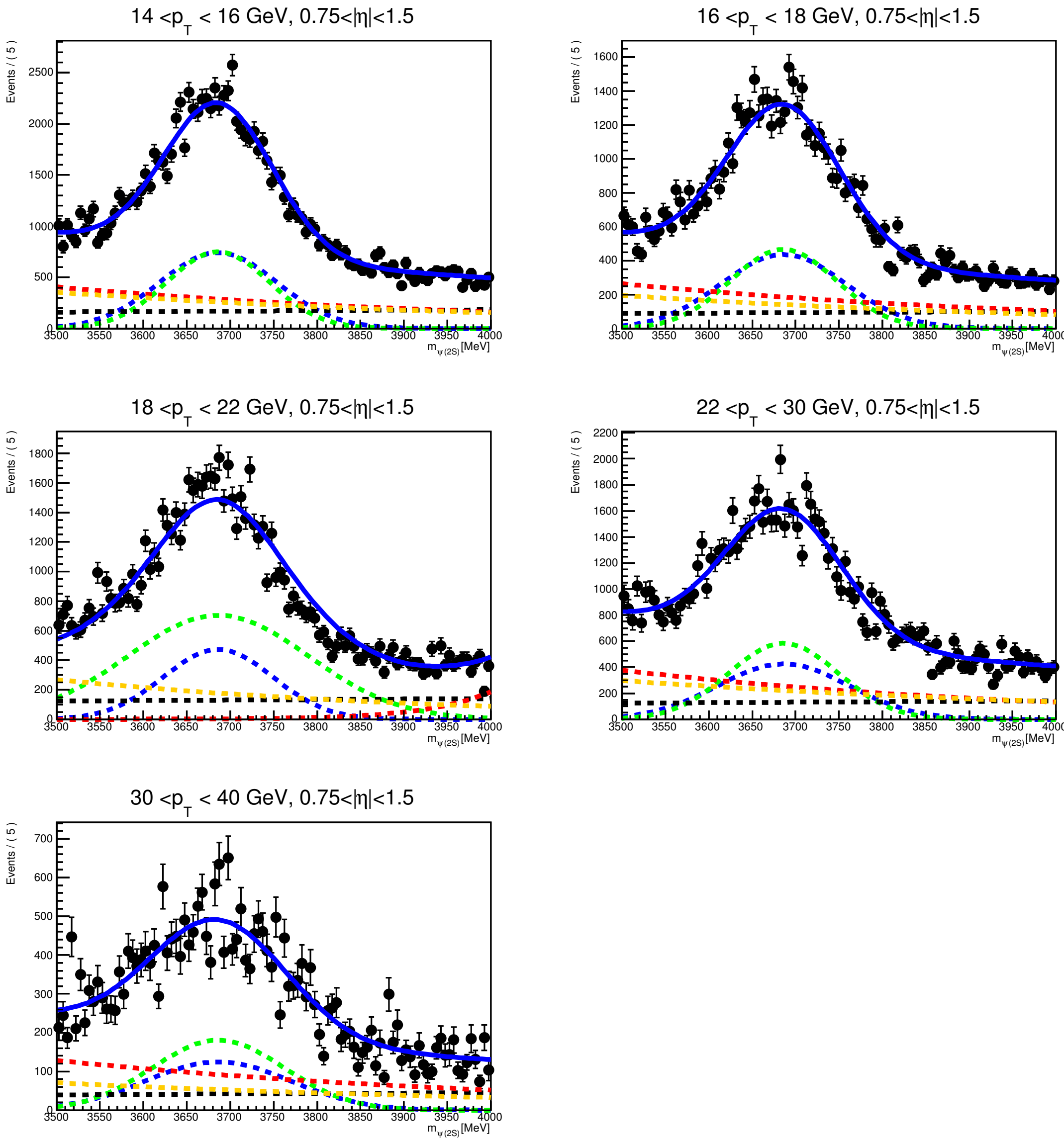

Figure B.4: Invariant mass distribution of weighted $\psi(2S)$ in rapidity $0.75 < |y| < 1.5$ for different transverse momenta p_{T}.

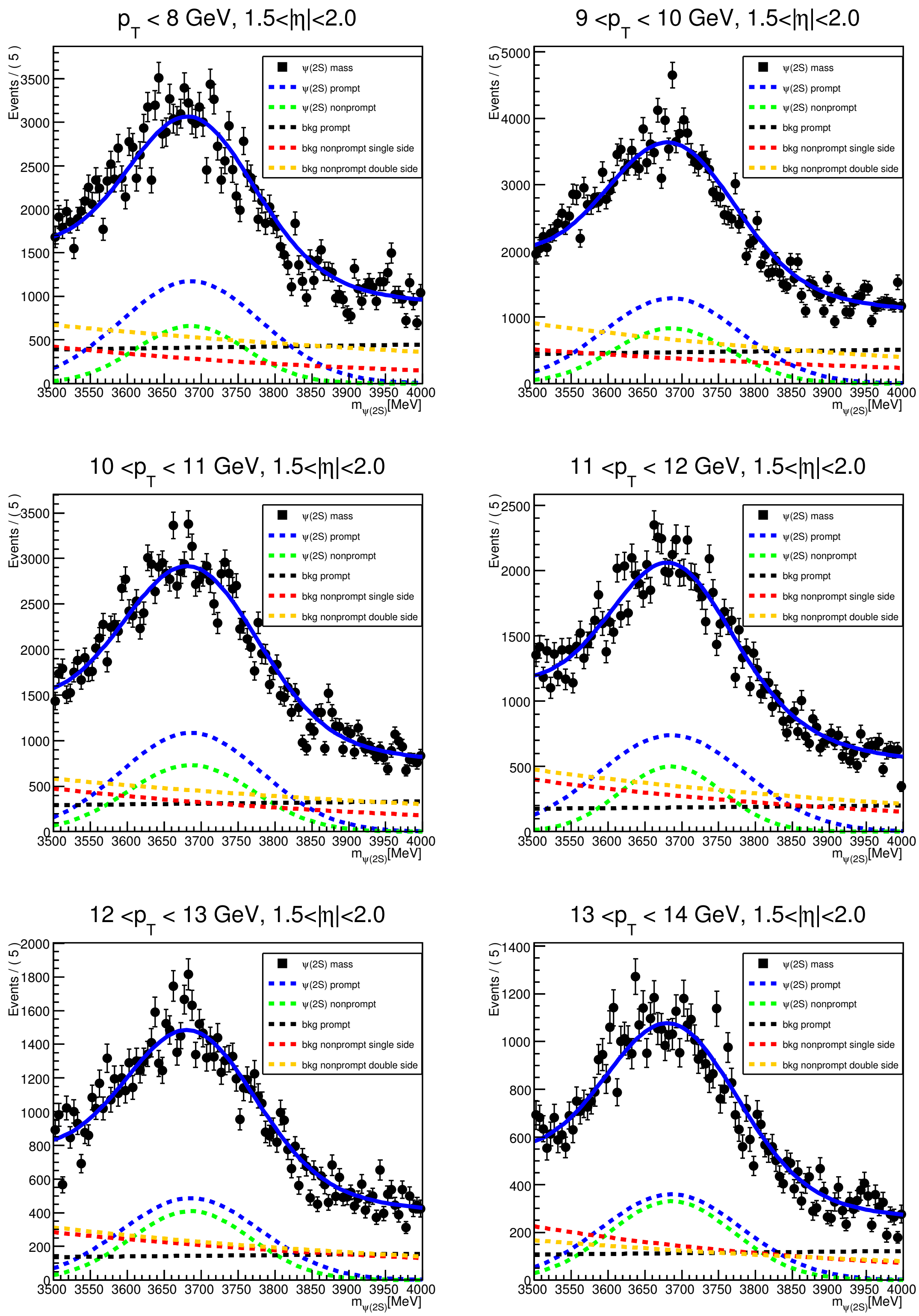

Figure B.5: Invariant mass distribution of weighted $\psi(2S)$ in rapidity $1.5 < |y| < 2.0$ for different transverse momenta p_{T}.

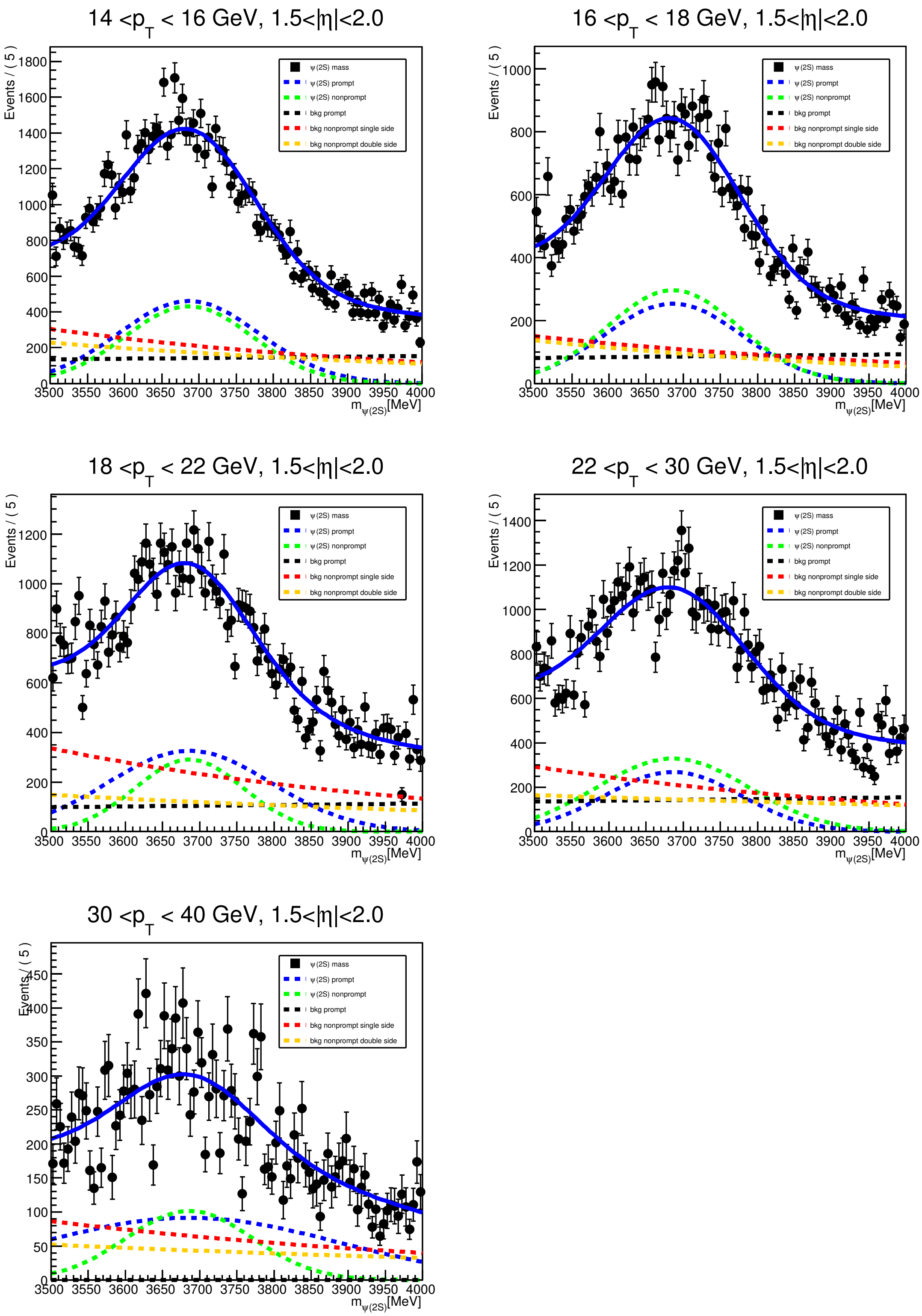

Figure B.6: Invariant mass distribution of weighted $\psi(2S)$ in rapidity $1.5 < |y| < 2.0$ for different transverse momenta p_{T}.

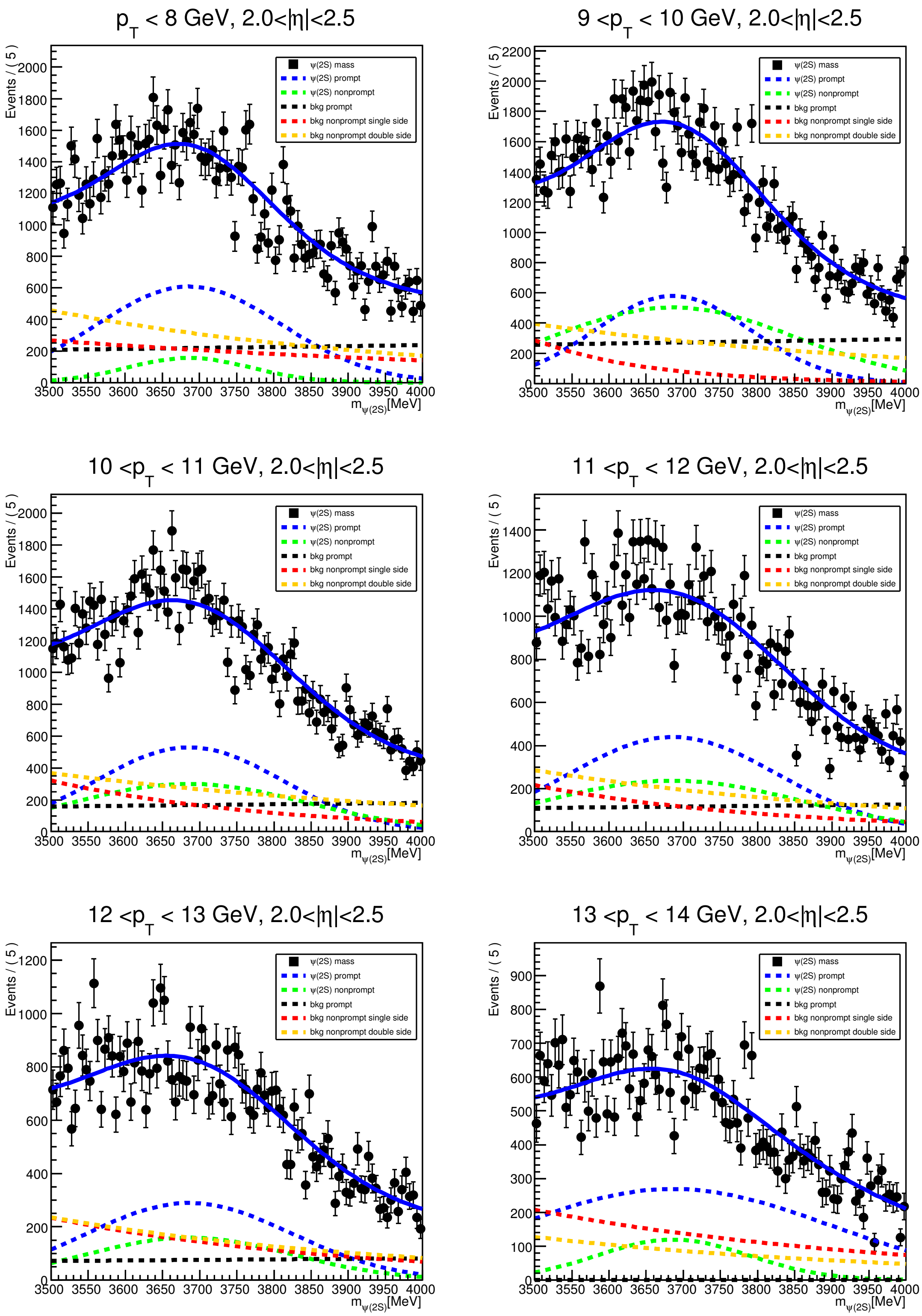

Figure B.7: Invariant mass distribution of weighted $\psi(2S)$ in rapidity $2.0 < |y| < 2.5$ for different transverse momenta p_{T}.

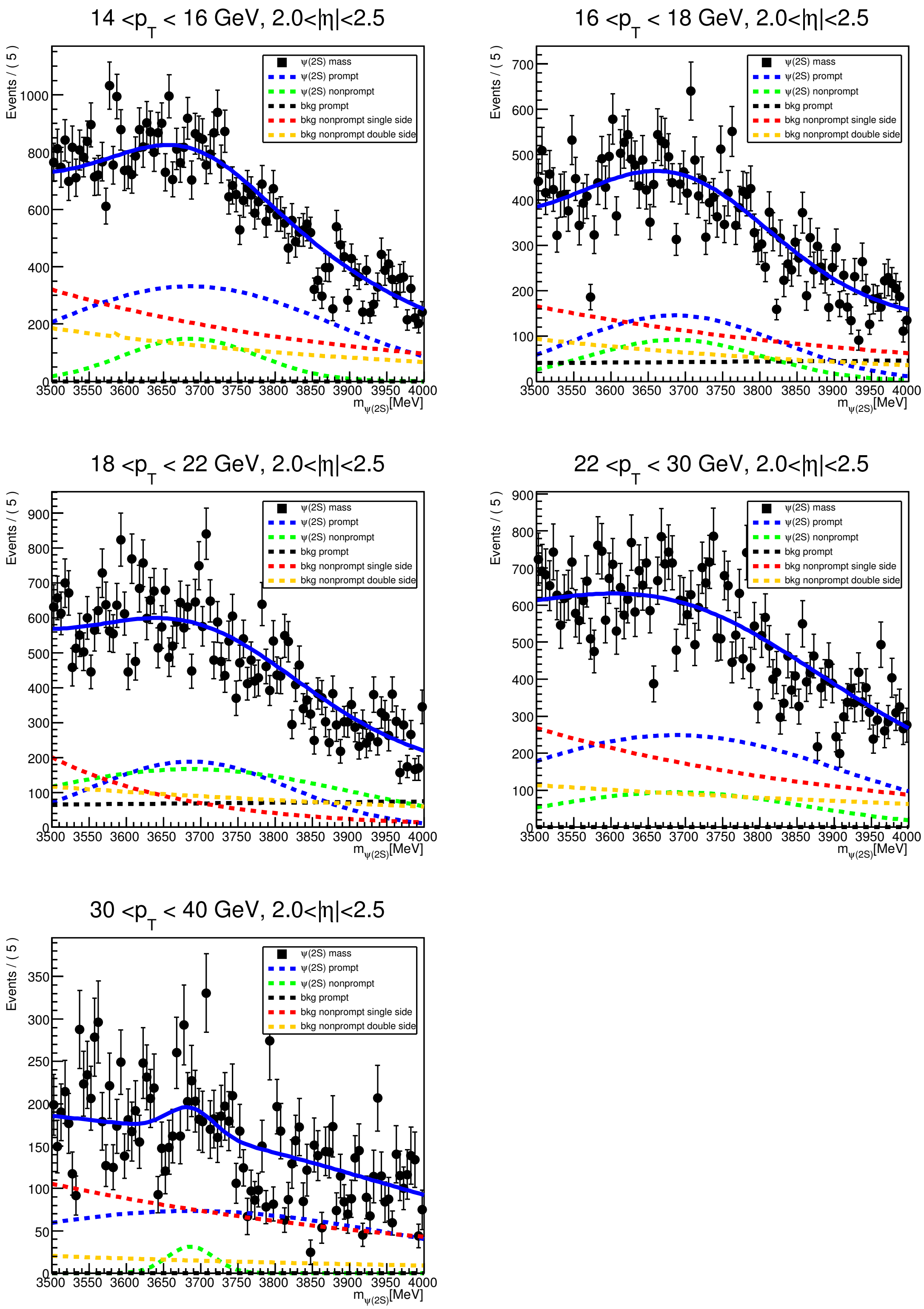

Figure B.8: Invariant mass distribution of weighted $\psi(2S)$ in rapidity $2.0 < |y| < 2.5$ for different transverse momenta p_{T}.

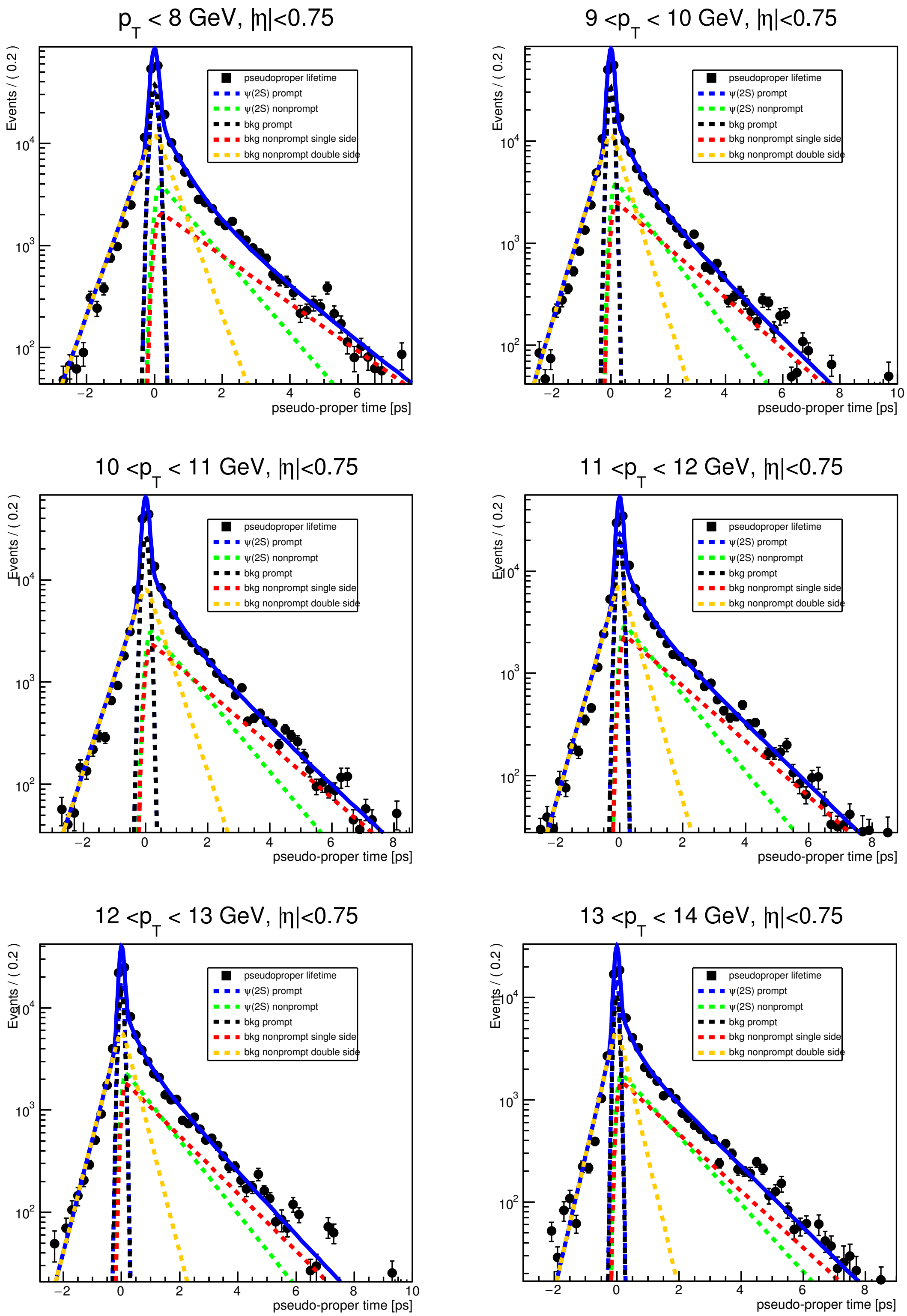

Figure B.9: Pseudo-proper lifetime distribution of weighted $\psi(2S)$ in rapidity $|y| < 0.75$ for different transverse momenta p_{T}.

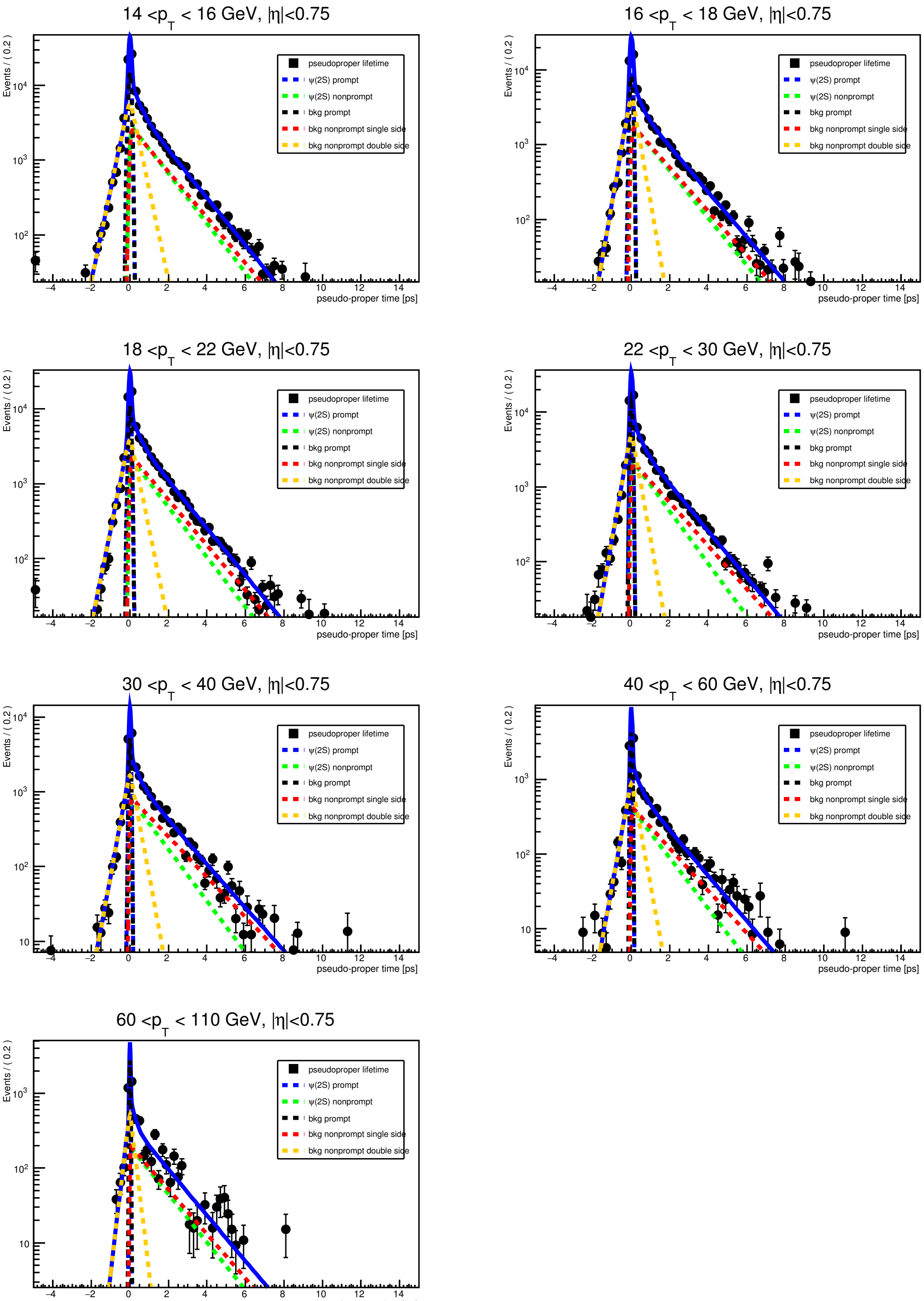

Figure B.10: Pseudo-proper lifetime distribution of weighted $\psi(2S)$ in rapidity $|y| < 0.75$ for different transverse momenta p_{T}.

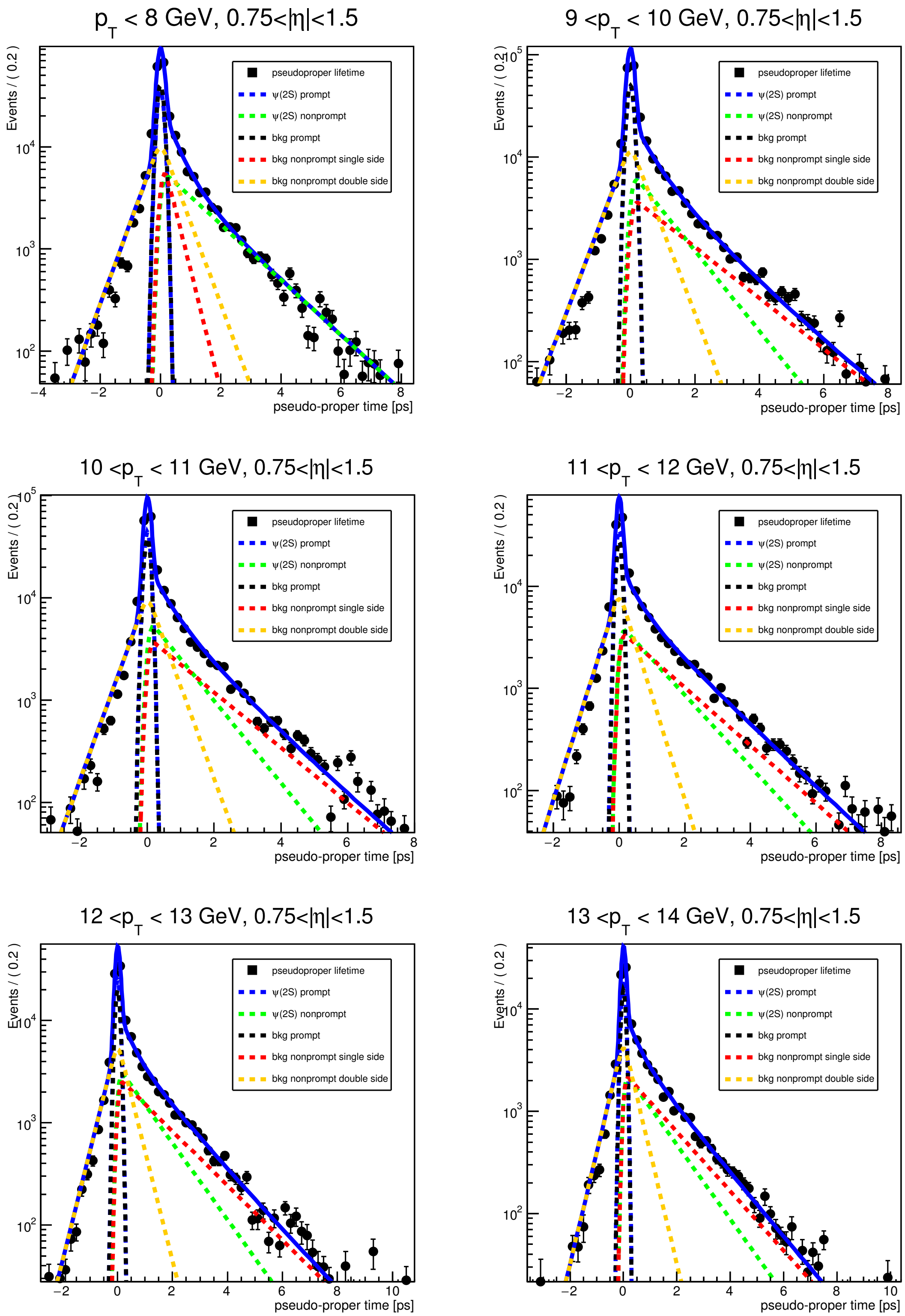

Figure B.11: Pseudo-proper lifetime distribution of weighted $\psi(2S)$ in rapidity $0.75 < |y| < 1.5$ for different transverse momenta p_{T}.

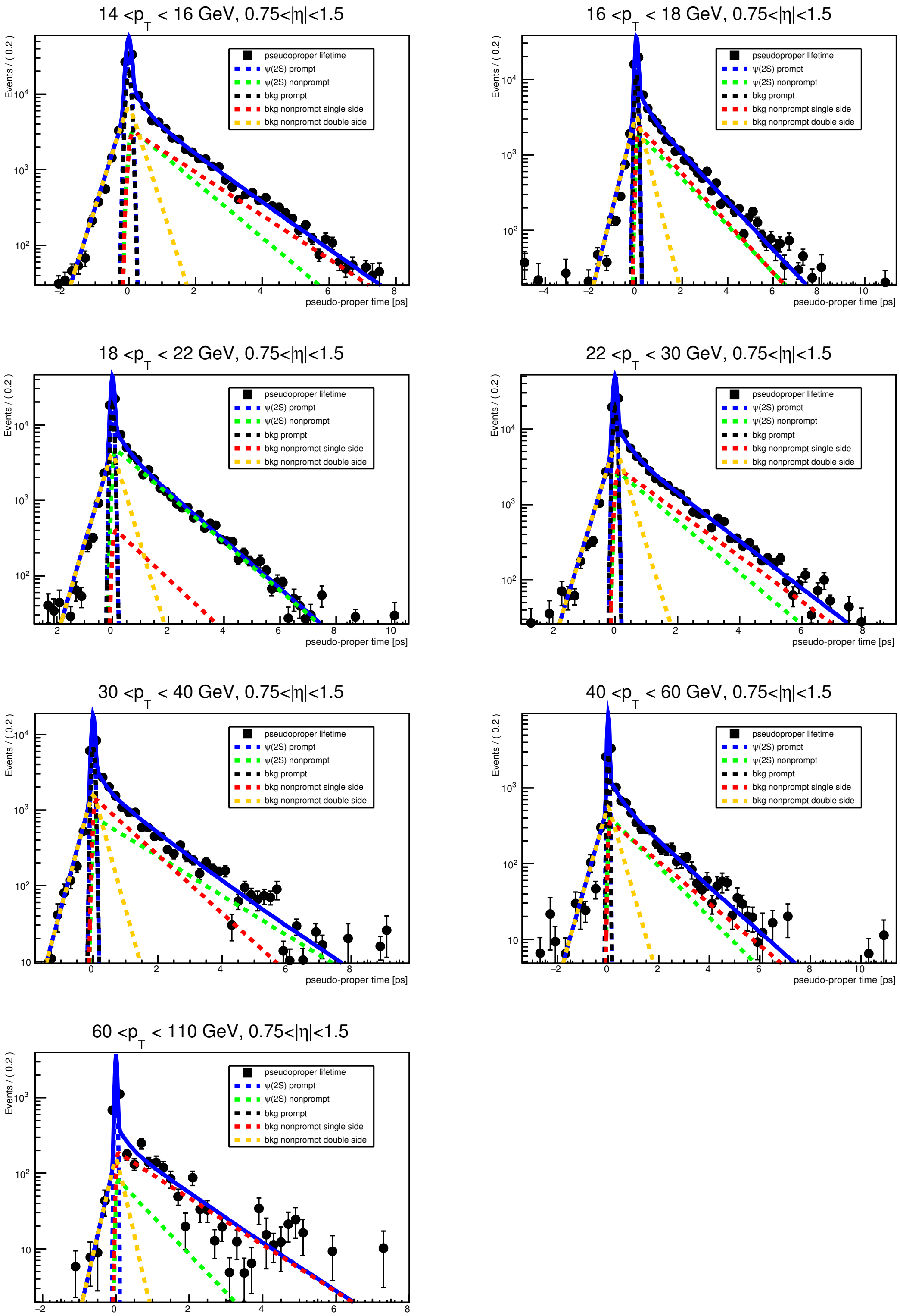

Figure B.12: Pseudo-proper lifetime distribution of weighted $\psi(2S)$ in rapidity $0.75 < |y| < 1.5$ for different transverse momenta p_{T}.

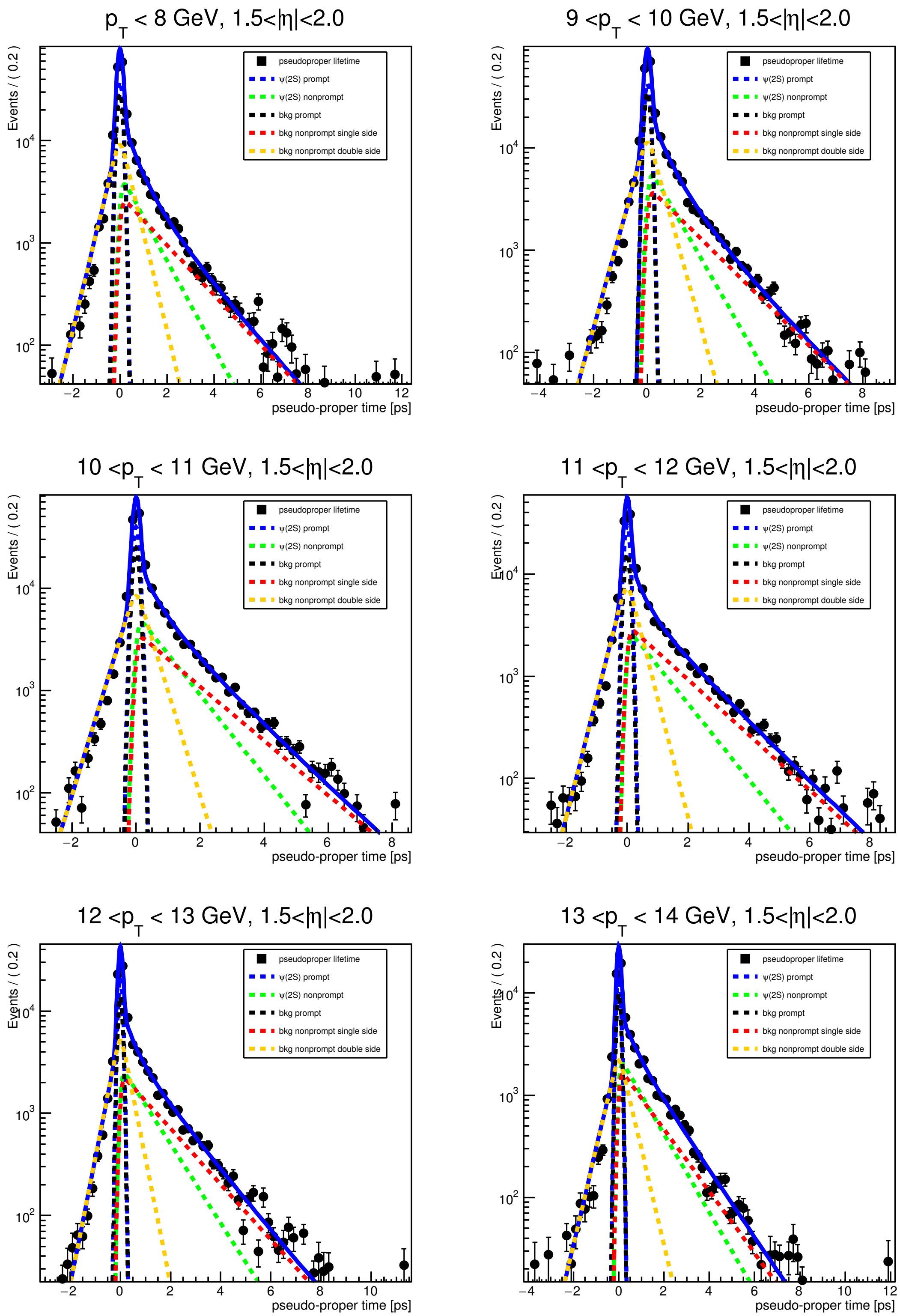

Figure B.13: Pseudo-proper lifetime distribution of weighted $\psi(2S)$ in rapidity $1.5 < |y| < 2.0$ for different transverse momenta p_{T}.

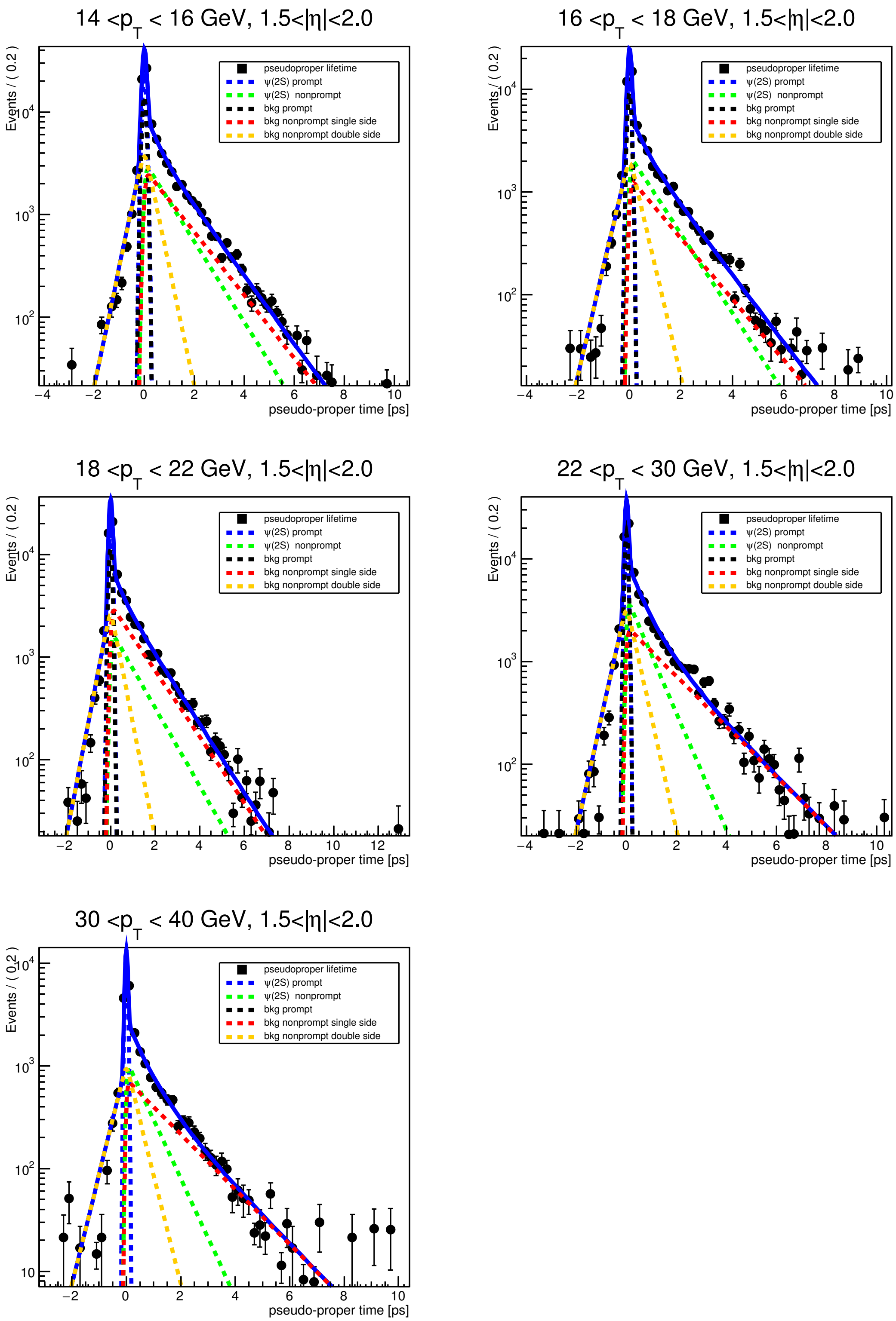

Figure B.14: Pseudo-proper lifetime distribution of weighted $\psi(2S)$ in rapidity $1.5 < |y| < 2.0$ for different transverse momenta p_{T}.

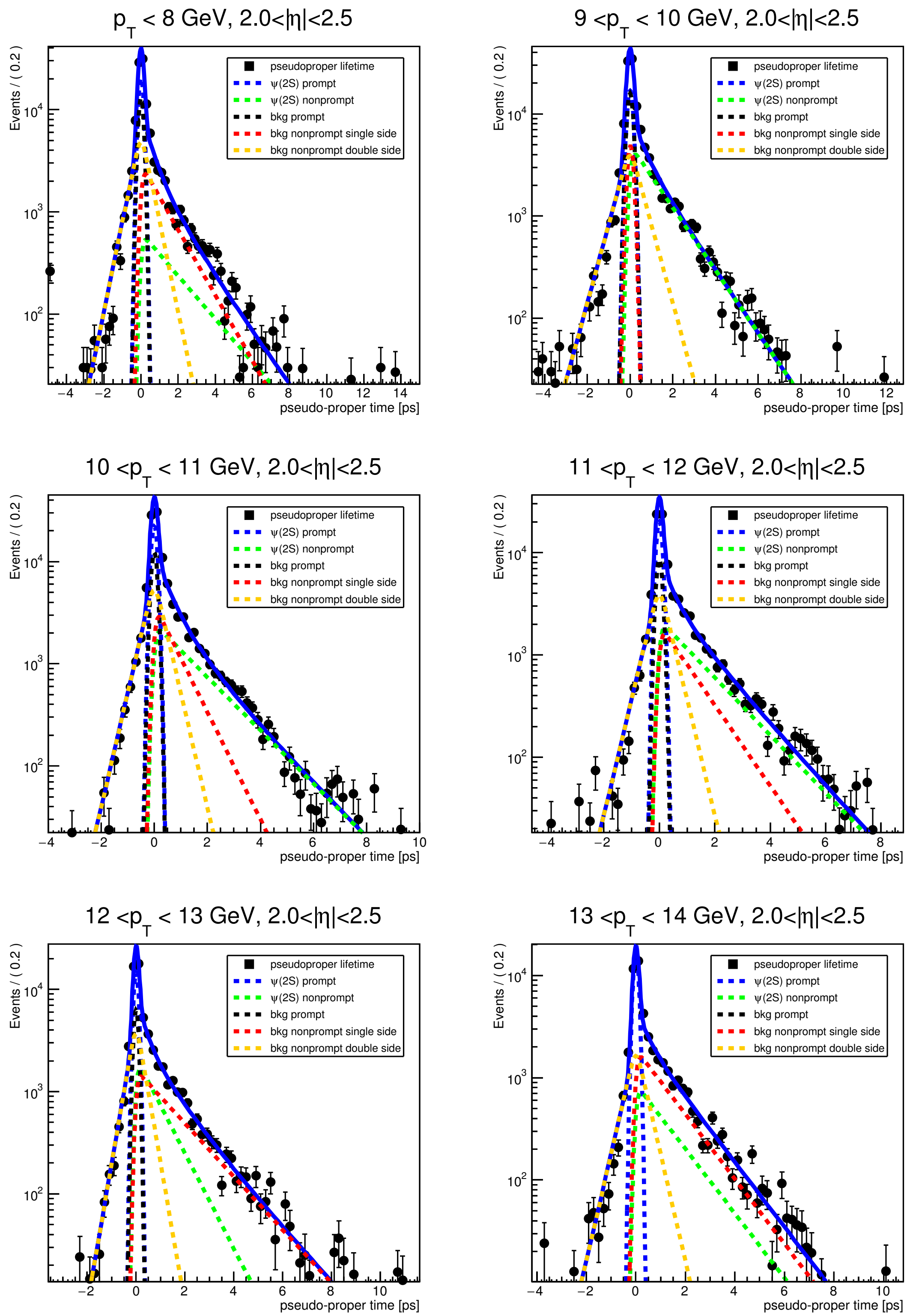

Figure B.15: Pseudo-proper lifetime distribution of weighted $\psi(2S)$ in rapidity $2.0 < |y| < 2.5$ for different transverse momenta p_{T}.

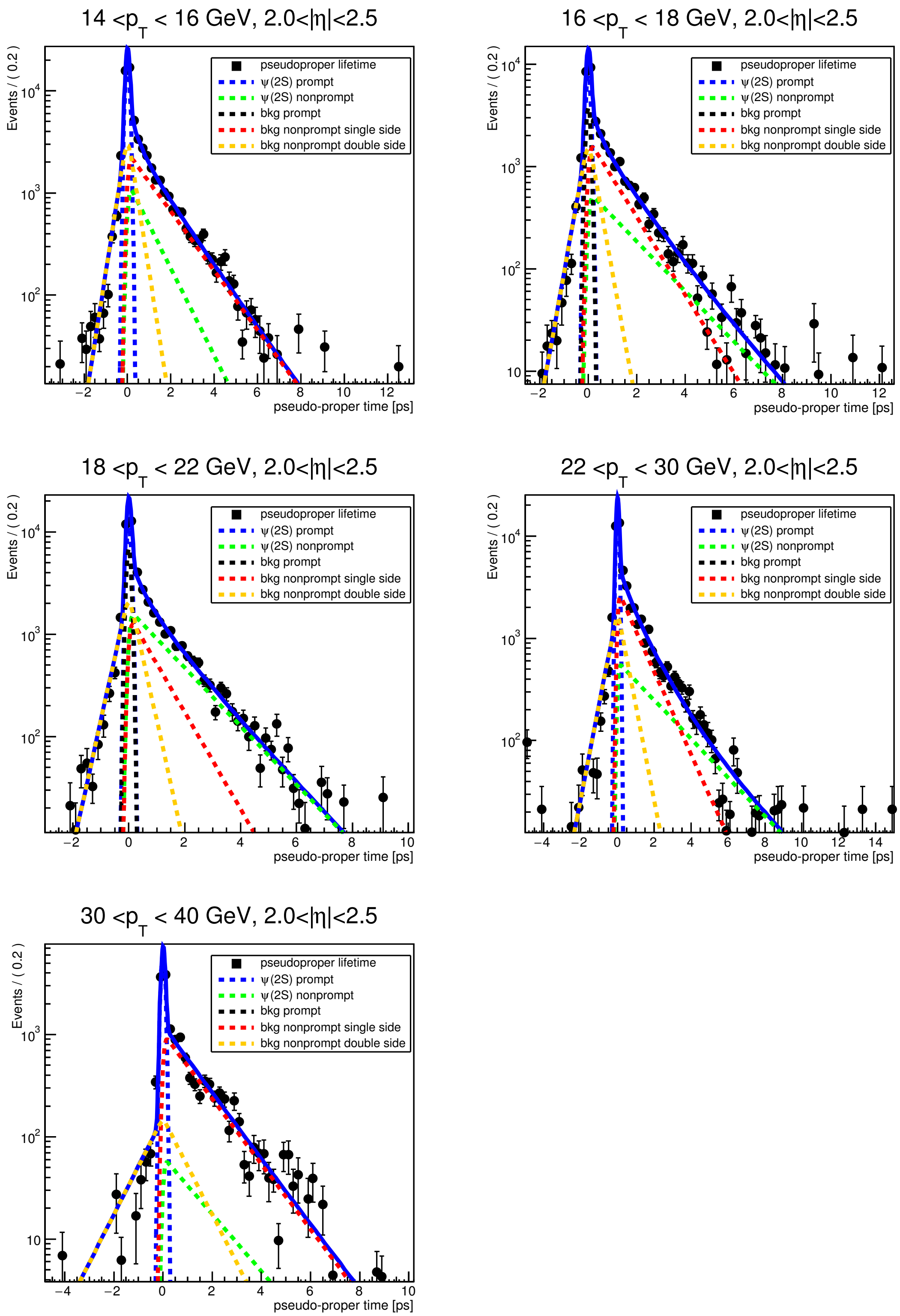

Figure B.16: Pseudo-proper lifetime distribution of weighted $\psi(2S)$ in rapidity $2.0 < |y| < 2.5$ for different transverse momenta p_{T}.

Bibliography

[1] K.A. Olive et al. (Particle Data Group), Chin. Phys. C, 38, 090001 (2014) and 2015 update

[2] Perkins, Donald. Introduction to High Energy Physics. Cambridge University Press, 2000

[3] Bettini, Alessandro. Introduction to Elementary Particle Physics. Cambridge University Press, 2014

[4] J. H. Christenson, J. W. Cronin, V. L. Fitch, and R. Turlay, Phys. Rev. Lett. 33, 138 (1964).

[5] B. Aubert et al., Phys. Rev. Lett. 100, 131802 (2008).

[6] R. Bluhm, Nucl. Instrum. Methods Phys. Res., B 221, 6-11 (2004).

[7] The KLOE-2 Collaboration, Phys. Lett. B 730, 89-94 (2014).

[8] C. W. Misner, K. S. Thorne, J. A. Wheeler. Gravitation. W. H. Freeman and Company, 2002

[9] Barry R. Holstein. Graviton Physics, arXiv:gr-qc/0607045v1, (2006).

[10] B. P. Abbott et al., Phys. Rev. Lett., 116, 061102 (2016).

[11] W. Pauli letter of the 4th of December 1930, Pauli Archive at CERN.

[12] G. Zweig, An SU(3) Model For Strong Interaction Symmetry And Its Breaking. 2, CERN-TH-412

[13] M. Gell-Mann, Phys. Lett. 8, 214 (1964).

[14] J. J. Aubert et al., Phys. Rev. Lett. 33, 1402 (1974).

[15] S. W. Herb et al., Phys. Rev. Lett. 39, 252 (1977).

[16] S. F. Abe et al., Phys. Rev. Lett. 74, 2626 (1995).

[17] P. A. R. Ade et al. Planck 2015 results. XIII. Cosmological parameters, arXiv:1502.01589v2, 2015

[18] R. Aaij et al., Phys. Rev. Lett., 112, 222002 (2014).

[19] R. Aaij et al., Phys. Rev. Lett.,115, 072001 (2015).

[20] P. A. M. Dirac, "A Theory of Electrons and Protons," Proc. Roy. Soc. A126, 360 (1930).

[21] C. D. Anderson, Phys. Rev. Lett. 43, 491 (1933).

[22] N. Cabibbo, Phys. Rev. Lett. 10, 531 (1963).

[23] S. Glashow, I. Iliopoulos and L. Maiani, Phys. Rev. D. 2, 1285 (1970)

[24] M. Kobayashi and K. Maskawa,Prog. Theor. Phys. 49, 652 (1973)

[25] E. Eichten, K. Gottfried, T. Kinoshita, K. D. Lane, and T. M. Yan, Phys. Rev. D 17, 3090 (1978)

[26] S. Okubo, Phys. Lett. 5, 1975 (1963)

[27] D. Melnyhuk, Ph.D. Dissertation/PANDA, The Andrej Soltan Institute for Nulear Studies (2009)

[28] S. C. C. Ting, Nobel Lecture: The Discovery of the J Particle: A Personal Recollection, accessed: 22-05-2016. [Online].
Available at http://www.nobelprize.org/nobel_prizes/physics/laureates/1976/ting-lecture.html.

[29] S. B. Richter, Nobel Lecture: From the Psi to Charm – The Experiments of 1975 and 1976, accessed: 22-05-2016. [Online].
Available at " http://www.nobelprize.org/nobel_prizes/physics/laureates/1976/richter-lecture.html.

[30] G. S. Abrams et al., Phys. Rev. Lett. 33, 1453 (1974).

[31] J. E. Augustin et al., Phys. Rev. Lett. 33, 1404 (1974).

[32] M.B. Voloshin. Charmonium. Prog.Part.Nucl.Phys., 61:455-511 (2008).

[33] CERN, The CERN accelerator complex, 2016, accessed 28-04-2016. [Online].
Available at https://espace.cern.ch/acc-tec-sector/default.aspx

[34] CERN, The accelerator complex. 2016, accessed 28-04-2016. [Online].
Available at http://home.web.cern.ch/about/accelerators.

[35] ATLAS Collaboration, Physics Letters B 716, 1–29 (2012).

[36] G. Aad et al. (ATLAS Collaboration), Phys. Rev. Lett. 108, 152001 (2012).

[37] Longer term LHC schedule. Accessed 15-06-2016. [Online].
Available at https://lhc-commissioning.web.cern.ch/lhc-commissioning/schedule/LHC-long-term.htm.

[38] CERN, Experiments. 2016, accessed 03-05-2016. [Online].
Available at http://home.cern/about/experiments.

[39] The ATLAS Collaboration at al. , The atlas experiment at the CERN Large Hadron Collider, Journal of Instrumentation, vol. 3, no. 08, p. S08003, 2008.

[40] A. V. Zlobin, Superconducting Magnets - Principles, Operation, and Applications. Wiley Encyclopedia of Electrical and Electronics Engineering. 1–19, 2014.

[41] ATLAS IBL Community, Insertable B-Layer - Technical Design Report, , CERN-LHCC-2010-013, (2010).

[42] Sandro Palestini, The Muon Spectrometer of the ATLAS Experiment, ATLAS Note ATL-COM-MUON-2003-005 (2002).

[43] Carlo Schiavi, ATLAS High-Level Trigger algorithms for Run-2 data-taking, ATLAS Note ATL-DAQ-PROC-2015-018 (2015).

[44] William Panduro Vazquez, Atlas Data Acquisition: from Run I to Run II, ATLAS Note ATL-DAQ-SLIDE-2014-387 (2014).

[45] ATLAS Collaboration , Muon reconstruction performance of the ATLAS detector in proton-proton collision data at $\sqrt{s} = 13$ TeV, CERN-EP-2016-033 (2016).

[46] N. Orlando, ATLAS Note ATL-PHYS-PROC-2012-011 (2012).

[47] R. Nicolaidou, L. Chevalier, S. Hassani, J.F. Laporte, E.L. Menedeu, A. Ouraou, J. Phys. Conf. Ser. 219, 032052 (2010).

[48] Louise Heelan. ATLAS Analysis Model: (How analysis should be done). Software Tutorial at CERN, 2016.

[49] Eric Lançon. Preparing ATLAS Distributed Computing for LHC Run 2, PoS(ISGC2014)045, 2014.

[50] Attila Krasznahorkay. The xAOD Event Data Model. ATLAS Software & Computing tutorials USM/PUC, Chile (2015).

[51] R. Brun and F. Rademakers, Nucl. Instrum. Meth. A389 81–86 (1997).

[52] http://proj-gaudi.web.cern.ch/proj-gaudi/

[53] https://root.cern.ch/

[54] http://roofit.sourceforge.net/